2015

Investigation of numerical viscosities and dissipation rates of shock-capturing schemes for implicit large-eddy simulation

Shreyas Bidadi

INVESTIGATION OF NUMERICAL VISCOSITIES AND DISSIPATION RATES OF SHOCK-CAPTURING SCHEMES FOR IMPLICIT LARGE-EDDY SIMULATION

by

SHREYAS BIDADI

A DISSERTATION

Submitted in partial fulfillment of the requirements
for the degree of Doctor of Philosophy
in
The Department of Mechanical and Aerospace Engineering
to
The School of Graduate Studies
of
The University of Alabama in Huntsville

HUNTSVILLE, ALABAMA

2015

In presenting this Dissertation in partial fulfillment of the requirements for a doctoral degree from The University of Alabama in Huntsville, I agree that the Library of this University shall make it freely available for inspection. I further agree that permission for extensive copying for scholarly purposes may be granted by my advisor or, in his/her absence, by the Chair of the Department or the Dean of the School of Graduate Studies. It is also understood that due recognition shall be given to me and to The University of Alabama in Huntsville in any scholarly use which may be made of any material in this Dissertation.

Shreyas

Shreyas Bidadi

03/26/2015

(date)

DISSERTATION APPROVAL FORM

Submitted by Shreyas Bidadi in partial fulfillment of the requirements for the degree of Doctor of Philosophy in Mechanical Engineering and accepted on behalf of the Faculty of the School of Graduate Studies by the Dissertation committee.

We, the undersigned members of the Graduate Faculty of The University of Alabama in Huntsville, certify that we have advised and/or supervised the candidate of the work described in this Dissertation. We further certify that we have reviewed the Dissertation manuscript and approve it in partial fulfillment of the requirements for the degree of Doctor of Philosophy in Mechanical Engineering.

Sarma Rani 03/23/2015
Dr. Sarma Rani (Date) Committee Chair

Kader Frendi 3/19/15
Dr. Kader Frendi (Date)

S. Ravindran 3/20/15
Dr. Sivaguru Ravindran (Date)

Shankar Mahalingam 03/23/15
Dr. Shankar Mahalingam (Date)

Robert A Frederick 3/23/15
Dr. Robert Frederick (Date)

D. K. Hollingsworth 3/23/15
Dr. D. Keith Hollingsworth (Date) Department Chair

Shankar Mahalingam 3/23/15
Dr. Shankar Mahalingam (Date) College Dean

D R Berkowitz 4/13/15
Dr. David Berkowitz (Date) Graduate Dean

ABSTRACT

School of Graduate Studies
The University of Alabama in Huntsville

Degree: Doctor of Philosophy College/Dept.: Engineering/Mechanical and Aerospace Engineering

Name of Candidate: Shreyas Bidadi

Title: Investigation of Numerical Viscosities and Dissipation rates of Shock-Capturing Schemes for Implicit Large-Eddy Simulation

In recent times, the limitations of popular subgrid-scale models for Large-Eddy Simulation have led to the development of a number of sophisticated modeling approaches. An approach that utilizes the numerical viscosity arising from the non-linear discretization of convective fluxes to model the smaller more isotropic eddies has received considerable attention. This method is referred to as Implicit Large-Eddy Simulation (ILES). The goal of this dissertation is to advance current understanding of a class of ILES techniques based on shock-capturing schemes. This is achieved through intricate quantitative insights into the stability and diffusive characteristics of Roe-MUSCL-based shock-capturing scheme.

The first step towards achieving the goal involved developing a formulation to quantify the numerical viscosity of the Roe-MUSCL scheme for the case of non-linear advection equation. The expression derived is a function of the flux limiter employed, distance between cell centers on either side of a face, face-normal velocity and a scaling factor. The significance of the scaling factor is revealed when the Roe-MUSCL scheme, originally developed for 1-D scenarios, is applied to 2-D scalar

advection problems. It is seen that without the scaling factor, the MUSCL scheme may not necessarily be monotonic in multi-dimensional scenarios.

In the next step, Roe's original shock-capturing scheme developed for 1-D Euler equations is extended to three dimensions in a manner that is consistent with the finite volume framework. After extending the scheme to second-order using van Leer's MUSCL extrapolation technique, an expression for numerical viscosity is derived following the procedure outlined for the advection equation case. To minimize the excessive dissipation of Roe-MUSCL for turbulent flows, the high numerical viscosity is mitigated using a z-factor that depends on the local Mach number.

In order to demonstrate the performance of Roe-MUSCL in capturing the physics of turbulent flows, a detailed investigation is conducted for decaying homogeneous isotropic turbulence with varying degrees of compressibility. The spectral profiles of numerical viscosity and dissipation rate demonstrate the effectiveness of the z-factor both in narrowing the wavenumber range in which dissipation occurs, and in shifting the location of the dissipation peak closer to the cut-off wavenumber. A number of statistical parameters for mesh resolution greater than 32^3 showed good agreement with prior direct numerical simulation and experimental studies. In the final step, Roe-MUSCL together with three Runge-Kutta temporal schemes is investigated for the Taylor-Green vortex transitional flow problem. The spectral profiles of numerical dissipation rate show that the Runge-Kutta scheme of Shu-Osher is the most stable and together with Roe-MUSCL accurately captures the physics of vortex stretching and subsequent production of dissipative eddies.

Abstract Approval: Committee Chair

Sarma Rani 03/23/2015

Dr. Sarma Rani

Department Chair

3/23/15

Dr. D. Keith Hollingsworth

Graduate Dean

4/13/15

Dr. David Berkowitz

ACKNOWLEDGMENTS

I would like to sincerely thank my advisor Professor Sarma Rani for his support and guidance throughout the years, his advise in choosing the problem to investigate and for the opportunity to pursue my own ideas. I am also grateful to my committee members, Dr. Kader Frendi, Dr. Sivaguru Ravindran, Dr. Shankar Mahalingam and Dr. Robert Frederick for their guidance and in providing insightful comments which has helped improve this dissertation. This work has benefited greatly from the fruitful discussions I had with a number of friends and colleagues at UAH over the past four years. I will always cherish the intellectual discussions I had with my good friends Vijaya Krishna Rani, Rohit Dhariwal, Madhu Sridhar, Bangalore Yashwanth and Ambarish Dahale. I would also like to thank my friend John Bennewitz for introducing me to the game of Racquetball.

Finally, this work would not have been possible without the love and support of my parents and younger brother Ashish. They are a constant source of strength and inspiration to me.

TABLE OF CONTENTS

PAGE

LIST OF FIGURES

FIGURE PAGE

LIST OF TABLES

TABLE PAGE

LIST OF SYMBOLS

SYMBOL	DEFINITION
q	Advected scalar
$\mathbf{Q}$	Vector of conserved variables
$\mathbf{u}$	Velocity of the advected quantity
α	Scaled characteristic speed
V	Cell volume
A	Surface area of a cell's face
$\mathbf{n}$	Normal vector
L, c	State at the left cell centroid
R, c	State at the right cell centroid
L	State to the left of an interface
R	State to the right of an interface
ψ	Flux limiter
$\mathbf{\Psi}$	Flux limiter matrix
Λ	Scaling factor
ν_{num}	Numerical viscosity or diffusivity
$H(.)$	Harten's correction

δ	Threshold parameter
$\mathbf{F}$	Flux vector in the x-direction
$\mathbf{G}$	Flux vector in the y-direction
$\mathbf{H}$	Flux vector in the z-direction
$\mathbf{A}$	Flux Jacobian
$\widetilde{\cdot}$	Roe-averaged quantity
θ	Component of a numerical flux
α	Coordinate direction
$\mathbf{R}$	Right eigenvector matrix
$\mathbf{L}$	Left eigenvector matrix
$\mathbf{\Lambda}$	Eigenvalue matrix
λ	Eigenvalue
ρ	Density
e_t	total energy
p	Pressure
T	Temperature
c_p	Specific heat at constant pressure
H	Total enthalpy
a	Sound speed

$\mathbf{d}$	Vector from the left to the right cell centroid
ν	Kinematic viscosity
Re	Reynolds number
z	Mach-number-dependent factor
S	Entropy
f_b	Body force

To my parents and brother

CHAPTER 1

INTRODUCTION

1.1 Nature of Turbulent Flows

Turbulent flows are ubiquitous. Most flows occurring both in nature and in engineering are turbulent. Examples of turbulent motion we might encounter in our everyday lives include smoke billowing from a chimney of a factory, flow of water around rocks, exhaust of jet or rocket engines, and hurricanes or tornadoes with the potential to cause tremendous damage to lives and property. Although the topic has gained the attention of some of the greatest mathematicians and engineers over the past two centuries, it still remains the last unsolved problem of classical physics. To this day there is still no clear understanding of what triggers turbulence nor can we predict such a motion with any degree of reliability even in simple flow configurations. A non-dimensional parameter that is typically used to characterize whether the fluid motion is laminar or turbulent is the Reynolds number, Re

$$Re = \frac{\rho U L}{\mu} \tag{1.1}$$

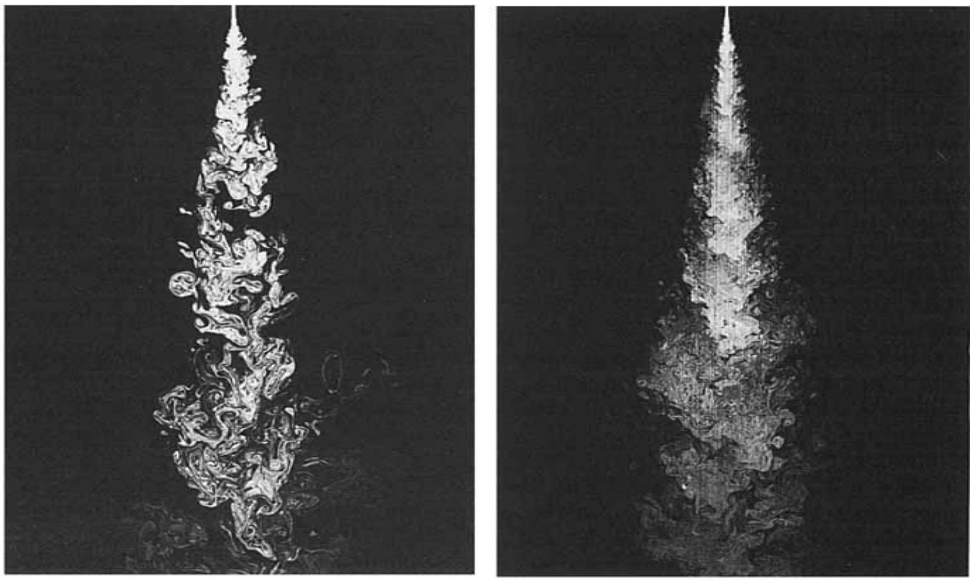

Figure 1.1: Turbulent jets issuing from a nozzle at (a) Re = 1500 and (b) Re=3000 [1].

where ρ and μ are the density and molecular viscosity of the fluid, U is its velocity and L is the length scale. It is essentially the ratio of the convective to the diffusion forces present in the fluid. In turbulent flows, the non-linear convective fluxes dominate the viscous terms. Figure 1.1 illustrates the development of a turbulent jet at $Re = 1500$ and 5000. The high Re flow transitions to turbulence much more rapidly and the large magnitude of perturbations in the flow generate finer vortical structures as compared to the lower Re case.

The Navier-Stokes equations represent the motion of all Newtonian fluids. The equations are accurate for both laminar and turbulent flows at all speeds. In the case

of incompressible flows, the non-linear, coupled system of equations are:

$$\nabla \cdot \mathbf{u} = 0 \tag{1.2}$$

$$\mathbf{u}_t + \mathbf{u} \cdot \nabla \mathbf{u} = -\nabla p + \nu \Delta \mathbf{u} + f_b \tag{1.3}$$

The high degree of non-linearity of the governing equations makes it impossible to obtain analytical solutions. Hence, a number of physically unrealistic simplifying assumptions are made to obtain closed form solutions.

One of the most popular definitions in literature to describe turbulent motion is from Richardson [18]. According to his view, large energy containing structures called eddies are highly unstable and break up into smaller eddies, thereby transferring the energy to these relatively small eddies. These smaller eddies break down and transfer energy to even smaller eddies. This process continues until the energy is dissipated at the smallest length scales due to the action of molecular viscosity. Richardson summarized his views as follows:

"Big whorls have little whorls,

which feed on their velocity;

And little whorls have lesser whorls,

And so on to viscosity."

A number of other definitions have been proposed to describe turbulence. But none seem to completely characterize turbulent motion nor say with any degree of certainty about when turbulence occurs. However, the definition proposed by Chapman and Tobak [19] is more deterministic than others:

"Turbulence is any chaotic solution to the 3-D Navier-Stokes equations that is sensitive to initial data and which occurs as a result of successive instabilities of laminar flows as a bifurcation parameter is increased through a succession of values."

The definition explicitly mentions Navier-Stokes as being the governing equations of all flows. It also describes turbulence as being chaotic but not perfectly random, since the governing equations themselves are deterministic. Due to the fact that turbulence is not a perfectly random process [20], there is no theory that can describe the phenomenon since large scales (non-linear) play a very important role in the evolution of the fluid. Thirdly, the definition states that turbulence is three-dimensional since the phenomenon is attributed to vortex stretching which occurs only in 3-D. Finally, it includes the phrase "sensitivity to initial data" which has been backed up by experimental measurements and is in agreement with modern mathematical treatment of the governing equations.

Significant strides in our understanding of turbulence has been made over the past century due to the study of homogeneous flows [21]. The statistics of such flows are invariant to the translation of the coordinate system and extend to infinity in all directions. This idealization permits the investigation of various scales of turbulent motion and development of a number of theories. Kolmogorov's theory [22] presented in the form of three hypotheses for homogeneous isotropic turbulence answers some of the fundamental questions concerning turbulent motion. The statistics in isotropic turbulent flows are invariant to translation, rotation as well as reflection of the coordinate system. According to the hypothesis of local isotropy, at very high Re, the

statistics of small scale motions can be considered isotropic. Local isotropy refers to the fact that small scales statistics are universal and display similar behavior in all high Re turbulent flows. Moreover, the statistics of the smaller eddies have a universal form that is determined uniquely by viscosity ν and dissipation rate ϵ. This conclusion is referred to as Kolmogorov's first similarity hypothesis. Three important length, velocity and time scales can be defined based on ϵ and ν:

$$\eta = \left(\nu^3/\epsilon\right)^{1/4} \tag{1.4}$$

$$u_\eta = (\epsilon\nu)^{1/4} \tag{1.5}$$

$$\tau_\eta = (\nu/\epsilon)^{1/2} \tag{1.6}$$

These are the Kolmogorov scales which describe the smallest dissipative structures. The Reynolds number based on these variables $Re_\eta = \eta u_\eta/\nu = 1$. This signifies that viscosity becomes very effective in remove the turbulent kinetic energy at the smallest length scales. The second similarity hypothesis of Kolmogorov states that the statistics of turbulent motion in the inertial subrange have a universal form that is uniquely determined by ϵ and is independent of ν. Moreover, the energy in this range scales as

$$E(k) = C\epsilon^{2/3}k^{-5/3} \tag{1.7}$$

An important manifestation of the three hypotheses is that the rate of energy transfer is independent of the length scale and is equal to ϵ. Finally, a consequence of the

theory is the following similarity hypothesis (also referred to as the $4/5^{th}$ law)

$$r\bar{\epsilon_r} = \frac{5}{4}\langle \Delta u^3 \rangle \tag{1.8}$$

where the dissipation rate $\bar{\epsilon_r}$ is averaged over the distance r, and Δu is the velocity increment.

The experimental works on homogeneous turbulence were conducted in wind tunnels by numerous researchers (see for example the work of Comte-Bellot and Corrsin [23]) to investigate turbulent statistics. As a result of rapid increase in computational power in the late 1970s, numerical simulations were conducted to compliment experimental and theoretical studies. Numerical experiments of homogeneous isotropic turbulent flow was pioneered by Clark [24]. Significant insights have been gained since then into the nature of turbulence as a result of solving the discretized form of incompressible as well as compressible form of governing equations both in physical and spectral space. The compressible form of Navier-Stokes equations are:

$$\partial_t \rho + \nabla \cdot (\rho \mathbf{u}) = 0 \tag{1.9}$$

$$\partial_t (\rho \mathbf{u}) + \nabla \cdot (\rho \mathbf{u}\mathbf{u} + \bar{p}\ \mathbf{I}) = \nabla \cdot \sigma + \rho \mathbf{g} \tag{1.10}$$

$$\partial_t (\rho e_t) + \nabla \left(\rho \mathbf{u} e_t + \bar{p}\mathbf{u}\right) = \nabla \cdot (\sigma\ \mathbf{u}) - \nabla \cdot \mathbf{q} \tag{1.11}$$

where, $\sigma = \mu\left[\left(\nabla \mathbf{u} + \nabla \mathbf{u}^T\right) - \frac{2}{3}\nabla \cdot \mathbf{u}\mathbf{I}\right]$ is the viscous stress tensor, $\mathbf{q} = \mathbf{q}_{cond} = -k\nabla T$ is the heat flux vector computed using the heat conduction law of Fourier, $e_t = e + \frac{1}{2}\mathbf{u} \cdot \mathbf{u}$ is the sum of internal and kinetic energies, respectively. The internal

energy e for an ideal gas (calorically and thermally diatomic perfect gas) is

$$e = \frac{1}{\gamma - 1}\frac{p}{\rho} \tag{1.12}$$

where $\gamma = c_p/c_v$ is the specific heat ratio equal to 1.4 for air.

There exists three main classes of simulating turbulent flows: (1) Direct numerical simulation (DNS), (2) Reynolds-Averaged Navier Stokes (RANS), and (3) Large-Eddy Simulation (LES). Following is a brief description of each of these approaches. A fourth approach, one that was considered controversial by many but which has been steadily gaining acceptance over the past decade is termed Implicit Large-Eddy Simulation (ILES). This last approach is the primary focus of the dissertation.

1.1.1 Direct Numerical Simulation

Direct numerical simulation (DNS) is the most accurate computational approach for turbulent flows. It resolves all length and time scales of turbulent motion. In the case of homogeneous, isotropic turbulent flow where the turbulent velocity field is considered periodic, DNS simulations are typically performed in wavenumber space [25] to obtain highly accurate results. Consequently, the grid size and time step chosen must be small enough to capture the characteristic time and length scales of the smallest eddies in the flow. DNS, however, is subject to the well-known limitation on the maximum Reynolds number that can be achieved, due to its prohibitive computational expense for realistic, high-Reynolds-number turbulent flows [26]. The

length scales of energy-containing eddies and the smallest dissipative eddies is proportional to $O(Re_L^{3/4})$. Since the ratio of the temporal scales is also of the same order, the number of grid points required is $O(Re_L^{9/4})$ [27] and the total cost of the simulation is $O(Re^3)$. Hence, the high computational cost of DNS has limited its applicability to low Re flows.

1.1.2 Reynolds-Averaged Navier Stokes

To simulate turbulent flows at moderate to high Reynolds numbers, Reynolds-Averaged Navier Stokes (RANS) simulations are considered to be the most popular and the least expensive of the modeling approaches. All flow variables are first decomposed into mean and fluctuating components. This is commonly referred to as *Reynolds decomposition*. Next, taking the mean of the Navier-Stokes equations and substituting the decomposed variables into the governing equations results in the well-known Reynolds equations. These set of equations contain the non-linear unclosed terms known as Reynolds stresses that are components of a symmetric rank 2 tensor [25]. The closure problem is typically dealt with using Boussinesq approximation; also referred to as the turbulent-viscosity hypothesis. The hypothesis states that the deviatoric part of the Reynolds stress is proportional to the mean rate of strain, where the proportionality constant is the turbulent (eddy) viscosity ν_T. A large number of turbulence models have been developed for wide range of flows to determine ν_T. While the modeling approach is less accurate than DNS, it is computationally cheaper making it feasible to solve very high Re practical problems. However, the lack of accuracy and errors generated by these models restrict their usage to steady

flows and flows without separation. It is interesting to note that most of the fundamental research in turbulence modeling have been restricted to incompressible fluids. For moderately compressible flows, these turbulence models have been applied with reasonable success. However, they become highly inaccurate at Mach numbers.

1.1.3 Large-Eddy Simulation

Large-Eddy Simulations (LES) have emerged as a potential, computationally feasible alternative to DNS and address some of the drawbacks of the RANS approach. LES involves resolving the large, anisotropic turbulent scales, and modeling the effects of unresolved small-scale eddies that may be considered isotropic (at least for high Reynolds numbers). In LES, any turbulent quantity can be decomposed into resolved and unresolved components

$$w = \bar{w} + w' \tag{1.13}$$

The large-scale component is obtained via a filtering operation

$$\bar{w} = \int_{\Omega} G(\mathbf{x}, \mathbf{y}) w(\mathbf{y}, t) d\mathbf{y} \tag{1.14}$$

where G is the filter function that depends on $\mathbf{x} - \mathbf{y}$ as well as on the filter width $\Delta = (\Delta_x \Delta_y \Delta_z)^{1/3}$, with Δ_i being the filter width in the i^{th} direction. The three most commonly used filter functions are the top-hat, Gaussian and spectral cut-off filter. The energy spectrum profile in Figure 1.2 shows the sharp cut-off filter in spectral space separating the anisotropic eddies from the nearly isotropic ones. The direction of the energy transfer along with the location of the cut-off wavenumber $k_c = \pi/\Delta$

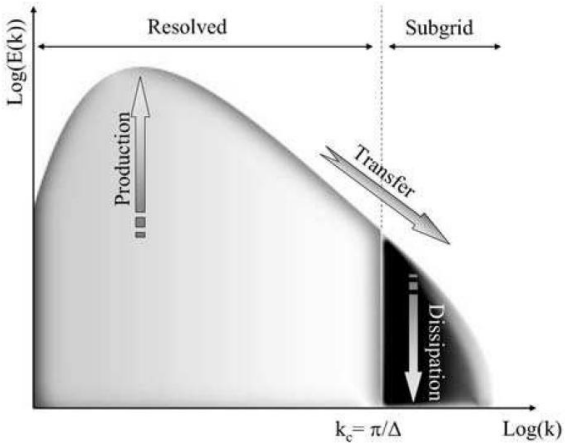

Figure 1.2: Homogeneous isotropic turbulence spectrum with sharp cut-off filter applied in the inertial subrange at cut-off wavenumber k_c [2].

are also shown in the figure. While most of the energy is transferred to small scales (outscatter), there also exists an inverse-cascade phenomenon (backscatter) whose intensity is much weaker than outscatter. Substituting the above decomposition into (1.3) yeilds the filtered equations with unresolved terms that require closure as in the RANS approach. In the case of compressible flows, it is convenient to introduce the following Favre-filtered or density weighted variable

$$\tilde{w} = \frac{\rho \bar{w}}{\bar{\rho}} \tag{1.15}$$

Hence, any flow quantity can be expressed as a sum of filtered ($\tilde{w}$) and unfiltered (w'') variables. The filtered, compressible form of Navier-Stokes equations can be

then written as

$$\partial_t \bar{\rho} + \nabla \cdot (\bar{\rho}\tilde{\mathbf{u}}) = 0 \tag{1.16}$$

$$\partial_t(\bar{\rho}\tilde{\mathbf{u}}) + \nabla \cdot (\bar{\rho}\tilde{\mathbf{u}}\tilde{\mathbf{u}} + \bar{p}\ \mathbf{I}) - \nabla \cdot \hat{\sigma} = -\nabla \cdot (\bar{\rho}\tau^{\mathrm{SGS}}) \tag{1.17}$$

$$\partial_t(\bar{\rho}\tilde{e}_t) + \nabla\,(\rho\tilde{\mathbf{u}}\tilde{e}_t + \bar{p}\tilde{\mathbf{u}}) - \nabla \cdot (\hat{\sigma}\ \tilde{\mathbf{u}}) + \nabla \cdot \tilde{\mathbf{q}} = -\tilde{\mathbf{u}}\nabla \cdot (\bar{\rho}\tau^{\mathrm{SGS}}) - \nabla \cdot \mathbf{q}^{\mathrm{SGS}} \tag{1.18}$$

where $(\bar{\rho}\tau^{\mathrm{SGS}}) = -2\bar{\rho}\nu^{\mathrm{SGS}}S_{ij}(\tilde{\mathbf{u}})$ from Boussineq approximation, and S_{ij} is the compressible form of the strain rate tensor

$$S_{ij} = \frac{1}{2}\left(\partial_j \tilde{u}_i + \partial_i \tilde{u}_j\right) - \frac{1}{3}\delta_{ij}\partial_k \tilde{u}_k \tag{1.19}$$

The SGS heat flux vector q_j^{SGS} in the energy equation is obtained from the following expression

$$q_j^{SGS} = -\frac{\bar{\rho}\nu_{SGS}c_p}{Pr_T}\partial_j \tilde{T} \tag{1.20}$$

Popular LES closure models to compute ν_{SGS}, commonly referred to as subgrid-scale (SGS) models (for modeling the effects of eddies not captured by the computational grid), include the isotropic eddy-viscosity models of Smagorinsky [28] and Germano [29]. Such models are based on the assumption that k_c is located in the inertial subrange and small scales are isotropic [2]. While Smagorinsky's model is computationally less expensive and complex, it is highly dissipative since the coefficient in the viscosity formulation is a constant. The model also fails to account

for backscatter. On the other hand, Germano's model [29], commonly referred to as the dynamic Smagorinsky computes the coefficient dynamically and is therefore dependent on the local flow conditions. It accounts for the backscatter mechanism and predicts proper energy transfer near walls and in transitional regimes. In general, the two models dissipate turbulent kinetic energy at the correct rate.

More sophisticated SGS models such as scale similarity and approximate deconvolution have been developed for ensuring proper energy transfer between length scales. However, they dissipate less energy than is normally needed for computational stability. This has led to the development of mixed models that contains positive aspects of both types of models. However, these are highly complex to implement and the computational resources necessary are significantly larger than isotropic eddy-viscosity models. Moreover, SGS models are not particularly suited to compressible turbulent flows since they fail to account for the intermodal energy exchange between acoustic, entropy and vorticity modes. Such models also do not capture the kinetic to internal energy conversion across shocks [30].

1.1.4 Implicit Large-Eddy Simulation

LES based on modeling SGS stresses *implicitly* through the leading-order truncation error terms of the discretized convective fluxes has therefore received considerable attention in recent years. This is possible through adaptive, non-linear discretization of advective terms in the Navier-Stokes equations [31]. The approach is commonly referred to as implicit large-eddy simulation (ILES) [32, 33]. Such non-linear high-resolution (also referred to as non-oscillatory finite volume (NFV)) schemes were

originally developed to circumvent Godunov's barrier theorem [34] which states that a second or higher-order linear scheme cannot be monotonicity preserving.

The history of ILES can be traced back to the work of Boris et al. [35] who attempted to take advantage of the dissipative nature of shock-capturing schemes to mimic the behavior of standard SGS models. Many ILES-based methods have been developed since the work of Boris et al. [35], which use high-resolution and higher-order schemes for convective fluxes that are atleast second-order accurate away from discontinuities [32]. Hence, the numerical or artificial viscosity terms that appear as a result of the discretization process are applied in a non-linear fashion similar to SGS viscosity in LES.

The concept of artificial viscosity was originally proposed by von Neumann and Richtmyer to remove Gibbs oscillation (ringing) in the vicinity of shock waves. The viscosity was added explicitly to ensure proper entropy rise across the shock front (i.e., the entropy change must be $\propto \Delta u^3$ [36]). Grinstein et al. [33] state that NFV methods and SGS models have their origins in the artificial viscosity concept (AVC). In fact, the Smagorinsky's SGS model was inspired by AVC and can be regarded as an extension of this concept to three dimensions to remove oscillations in weather and climate predictions.

ILES approaches are sometimes referred to as monotonically integrated LES (MILES) in literature, since the nonlinearity of high-resolution schemes prevents the development of unphysical extrema in the solution. The MILES approach of Fureby and Grinstein [32] consists of a flux limiting/correcting method wherein the convective fluxes in Navier-Stokes equations are expressed as a flux-limiter-weighted combination

of higher and lower order fluxes. Other MILES approaches utilize Godunov's type upwind method (also referred to as shock-capturing schemes) that effectively results in local Riemann problems for state variables at all internal (non-boundary) faces. The convective flux vector is expressed as a sum of central differenced and artificial diffusion terms, with the latter being controlled using a flux limiter. Godunov-based methods have the potential to account for intermodal energy transfers in compressible flows and correctly capture the dissipation across shocks. Morever, by carefully controlling the dissipation inherent to these methods, one can successfully reproduce the $-5/3$ power law of the energy spectrum in the inertial subrange for low Mach-number flows.

Since its conception by Boris in 1990 [37], ILES technique has been successful in capturing the physics of fluid of both practical and academic interest. Woodward and coworkers performed ILES simulations of compressible homogeneous turbulence and problems in astrophysics at very high Reynolds number. The method has also been utilized in the study of Rayleigh-Taylor, Kelvin-Helmholtz and Richmyer-Meshkov instabilities which are inherently challenging to simulate due to adjacent regions of very high and very low Reynolds number. Finally, the multidimensional positive definite advection transport algorithm (MPDATA) ILES method has been used in geophysical applications. Despite its success, the method has not been widely used as LES. This is because there is a need to understand at a very fundamental level as to why and how ILES works compared to traditional SGS models, and to also study its limitations as well.

This motivated researchers at the turn of the century to conduct fundamental studies on ILES methods. Fureby and Grinstein [32] examined the effects of the discretization of NFV schemes by expressing the discretized Navier-Stokes equations back into partial differential equation (PDE) form that essentially satisfied the numerical solution. The framework was given the name Modified Equation Analysis (MEA) since it resulted in an explicit expression for numerical viscosity. A detailed analysis presented by the authors showed similarity between implicit SGS model due to the flux limiting NFV scheme and explicit SGS models. Rider and Margolin [38] also performed MEA for a number of NFV schemes in one dimension to show connection with SGS models. Recently, Drikakis et al. [26] provided the criteria that need to be satisfied for ILES simulations to generate physically realistic solutions: (1) the mesh resolution and numerical scheme chosen must be able to resolve the large energy-containing eddies, and (2) the numerical scheme should capture the instabilities driving the laminar to turbulent transition. An important manifestation of a scheme meeting these criteria is its ability to capture the $-5/3$ slope of the energy spectrum in the inertial subrange. In addition, for compressible flows, the schemes must also be monotonic in density and pressure to prevent unphysical oscillations in the solution [26]. Thornber et al. [9, 39] performed rigorous theoretical analysis to show why high-resolution Godunov schemes are excessively dissipative in low-Mach number turbulent flows. The authors also developed a modification to the fluxes to recover the $-5/3$ inertial slope.

The objective of this dissertation is to provide further justification of the ILES technique based on high-resolution shock-capturing schemes for all Mach number tur-

bulent flows. The second-order extension of Roe's shock-capturing scheme [40] is utilized to discretize the convective terms of compressible Euler equations. Prior to deriving expressions for viscosity and dissipation rate of this scheme for the Euler equations, an approach to quantifying the viscosity of the scheme for the non-linear advection equation is presented first. The resulting viscosity profiles will be examined for a number of non-linear flux limiters for 1-D and 2-D canonical problems. Therefore, this study presents for the first time both the magnitude and the spatial distribution of the numerical viscosity inherent to the non-linear scheme. For the system of non-linear equations, the same procedure will be utilized to quantify the numerical viscosity, and the expression along with the dissipation rate formulation will be investigated in both physical and Fourier space for compressible isotropic turbulence and Taylor-Green vortex transitional flow problems. These provide us with quantitative insights into the wavenumber range in which the effects of dissipation are most significant. A modification of the form proposed by Thornber et al. [9] is introduced to minimize the viscosity and consequently the dissipation in low Mach number regions of the flow. The above two test cases are meant to demonstrate that Godunov-based schemes such as Roe's solver can accurately capture the physics of both turbulent and transitional flows, thereby satisfying the two criteria laid out by Drikakis et al. [26].

1.2 Numerical Methodology

This study utilizes the LOCI programming framework [41] for all problems. It is a C++ based unstructured code for performing finite volume computations.

Also referred to as rule-based framework, a LOCI application does not require the user to define any loops. Although the looping over cells and faces is determined internally, separate *rules* must be written however to perform computation for cell faces, cell centers and domain boundaries. *Facts* or user defined input must also be specified. Both rules and facts are necessary for the system to construct a solution. Another advantage of LOCI is automatic parallelization. Athough a LOCI code involves no explicit parallel directives, it can be run in parallel without changes. The framework has been used in the development of two popular CFD codes in the aerospace community; LOCI-CHEM [42] and LOCI-STREAM [43]. The former solves chemically reactive flow problems while the latter contains finite volume modules developed specifically for aerodynamic problems.

CHAPTER 2

NON-LINEAR ADVECTION EQUATION

2.1 Introduction

In the Finite Volume Method (FVM), the computation of convective fluxes at the cell faces presents a well-known conundrum. The difficulty arises because at a cell face one may have two distinct states of the convected quantities arising from the "reconstruction" using the cell-centered variables (and, if needed, their gradients) on either side of the face of interest. One may then compute the interface flux either by averaging the left- and right-reconstructed states at the face, or by simply using the left/right state depending upon whether the dot product of the face-velocity and the face-normal vectors is positive/negative. The former approach is conventionally referred to as central differencing, while the latter is called upwind differencing. The second order central differencing scheme (CDS) is a linear scheme that works well in smooth regions, but is unstable and non-monotonic near discontinuities and in high-gradient regions. The first-order upwind differencing scheme (UDS) is also a linear scheme that is stable but excessively diffusive. In fact, UDS is the most diffusive spatial discretization scheme. The celebrated Godunov's theorem [7, 34] states that a linear discretization scheme that is non-oscillatory can at the most be first-order accu-

rate near high-gradient regions. To overcome this constraint, computational research during the past three to four decades has focused on developing non-linear, non-oscillatory schemes known as TVD (Total Variational Diminishing) that are higher order accurate even near discontinuities and are therefore less diffusive than, say, UDS. A scheme is said to be TVD if

$$TV(\phi^{n+1}) \leq TV(\phi^n) \tag{2.1}$$

where ϕ is the quantity of interest, n is the time step and TV stands for total variation of the discrete solution:

$$TV(\phi) = \sum_{i=1 \in N} |\phi_i - \phi_{i-1}| \tag{2.2}$$

where i refers to the i^{th} computational cell and N is the total number of cells.

Boris and Book [44] developed a second-order TVD scheme known as the Sharp and Smooth Transport Algorithm (SHASTA), which is based on the "flux correction" principle. The methods that use this principle are referred to as the Flux-Corrected Transport (FCT) methods and contain two key steps. The first is a transport or convective step that involves the time-advancement of the solution and uses a first-order linear spatial scheme. While the transport step is conservative and non-oscillatory, it is also highly diffusive. The second step is an anti-diffusive or corrective stage that adds anti-diffusion controlled by a flux limiter to reduce the numerical diffusion while ensuring that the solution remains monotonic throughout the domain. It is the addition of anti-diffusion that makes these schemes non-linear.

FCT schemes are highly useful for solving many unsteady flow problems but are less so for steady-state computations.

An alternative approach to achieving second order accuracy while satisfying the TVD criterion is through van Leer's Monotone Upwind Scheme for Conservation Laws (MUSCL) technique [45]. The MUSCL scheme has two fundamental components. The first involves a piecewise linear representation of data within a cell. The second and the more important part involves limiting through a flux limiter function, ψ, the gradients used in reconstructing state variables within a cell. [45]. A third order extension can also be achieved by assuming piecewise parabolic distribution of data in each cell [46]. A formulation very similar to that of van Leer's MUSCL technique was developed in the early 1970s by Vladimir P. Kolgan [47] at the Central Aerodynamical National Institute (TsAGI) near Moscow, Russia. This work was unknown both within and outside of Russia and only recently did an English translation [48] of the original article appear in the Journal of Computational Physics. As in the MUSCL approach, cell-centered quantities were linearly reconstructed to the interfaces and the sub-cell gradients were limited by a primitive form of the now well known minmod limiter. The crudeness of the limiter restricted the Courant number to 1/2. Moreover, Kolgan's choice of first order accurate forward Euler time discretization scheme resulted in the appearence of steps or little jumps in the numerical solution in spite of the non-linearity of the spatial discretization scheme.

In general, the concept of TVD is considered to be one of the most significant accomplishments in the development of numerical methods for partial differential equations (PDEs). In fact, the success of CFD can be attributed to the develop-

ment of such high-resolution schemes [49]. A sound theoretical framework exists for 1-D scenarios involving uniform, orthogonal meshes. However, they have since been extended on an empirical basis to multi-dimensional problems involving unstructured non-orthogonal meshes [7]. For instance, a number of studies [4, 5, 50, 51] have attempted to directly extend the 1-D TVD schemes to multi-dimensional unstructured meshes. However, in terms of maintaining the monotonicity of these extended schemes, the results were mixed, particularly for multi-dimensional problems. One of the aspects addressed in this study is to understand and explain the reasons for this loss of monotonicity.

When extending the original TVD schemes to unstructured, non-uniform meshes, an important consideration lies in deriving a suitable expression for the r-factor needed to evaluate the limiter function. Bruner [50, 51] attempted to extend the 1-D r-factor to unstructured meshes. However, the unstructured mesh r-factor in [50, 51] failed to recover the original formulation for structured meshes. Subsequently, Darwish and Moukalled [4] developed an r-factor for unstructured meshes that did recover the original 1-D formulation. Another advantage of the Darwish and Moukalled r-factor is that it only requires variable information from the cell centroids on either side of a face, which is readily available on unstructured grids. Recently, Li et. al [5] developed an r-factor that requires information from two cells upstream of the face under consideration.

The objectives of this chapter are two fold. First, an explicit expression is derived for the numerical viscosity, ν_{num}, arising from the application of the popular first order Roe scheme together with MUSCL reconstruction step to the scalar

advection equation. Secondly, the numerical viscosity due to the various TVD limiters is quantified and compared for four canonical problems from the literature: 1-D advection of a step function profile [3], and 2-D advection of step, sinusoidal, and double-step profiles [4, 5]. For all cases, it is seen that the superbee scheme provides the lowest numerical viscosity. Further, the diffusive effects of superbee have the smallest spatial extent and are most confined to the vicinity of the discontinuity (or high-gradient regions). The minmod scheme is the most diffusive among the limiters considered, as well as active in regions away from the discontinuity. These trends are explained using Sweby's TVD diagram that plots the limiter function $\psi(r)$ as a function of r. The current viscosity formulation facilitates the consistent extension of TVD limiters to multi-dimensional problems while retaining their monotonic character. This is achieved through the use of a scaled limiting function in the original MUSCL scheme.

2.2 Numerical Approach

The governing equation of interest in the current study is the unsteady advection equation:

$$\frac{\partial q}{\partial t} + \nabla \cdot (\mathbf{u}q) = 0 \tag{2.3}$$

where $q = q(\mathbf{x}, t)$ is the advected scalar, $\mathbf{u} = \mathbf{u}(\mathbf{x}, t)$ is the advection velocity and $\mathbf{x}$ is the position vector. Integrating ((2.3)) over a grid cell of volume V and applying

the Gauss divergence theorem yields

$$\frac{d}{dt}\int_V q(\mathbf{x},t)\,dV + \int_A (\mathbf{u}q)\cdot\mathbf{n}\;dA = 0 \tag{2.4}$$

where A represents the cell surface area and $\mathbf{n}$ is the unit vector normal to that surface. Using the second-order midpoint rule

$$\int_V q(\mathbf{x},t)\;dV = q(t)\;V \tag{2.5}$$

where $q(t)$ is the value of q at the cell centroid. The surface integral in (2.4) can be approximated as

$$\int_A \mathbf{F}\cdot\mathbf{n}\;dA \approx \sum_{f\in\text{cell faces}} (\mathbf{F}\cdot\mathbf{n})_f\;A_f \tag{2.6}$$

where $\mathbf{F} = \mathbf{u}q$ is the interface flux and A_f is the control surface area. Substituting (2.5) and (2.6) into (2.4) and writing the resulting equation in terms of residual R yields

$$V\;\frac{dq}{dt} = -R(q,t) \tag{2.7}$$

where $R = \sum(\mathbf{F}\cdot\mathbf{n})_f\;A_f$. Using a general time discretization scheme of the form presented in [52, 53], (2.7) can be written as

$$V\frac{q^{n+1}-q^n}{\Delta t} = -\sigma R(q^{n+1}) + (\sigma-1)R(q^n) \tag{2.8}$$

where σ is a positive real number between 0 and 1; $\sigma = 0$ results in the forward Euler (explicit) scheme, whereas the values of 0.5 and 1 correspond to the Crank-Nicolson

(semi-implicit) and the backward Euler (implicit) schemes, respectively. The Crank-Nicolson scheme is utilized in this study.

Performing a Taylor Series expansion of $R(q^{n+1})$ around q^n results in a discretized equation of the form

$$\left[\frac{V}{\Delta t} + \sigma \frac{\partial R(q^n)}{\partial q}\right] \Delta q = -R(q^n) \tag{2.9}$$

where $\Delta q = q^{n+1} - q^n$.

2.3 Roe-MUSCL Scheme and Numerical Viscosity

The original Roe's interface flux developed for the 1-D Euler system of equations [40] has been subsequently applied to the scalar advection equation as follows [54, 55]:

$$F_f = \frac{1}{2}[F(q_L) + F(q_R)] - \frac{1}{2}|\alpha_f|(q_R - q_L) \tag{2.10}$$

where q_L and q_R are the reconstructed values of q at the cell face obtained using data in the left and right cells, respectively, and $\alpha_f = \frac{\partial F}{\partial q}$ is the scaled characteristic speed. Note that the two 1/2 factors on the RHS of (2.10) are due to the 1-D uniform mesh used in deriving the original Roe's formulation. Therefore, one needs to be cognizant that the extension of (2.10) to unstructured meshes is empirical and approximate [7]. The notations used for the interface and cell-centered variables are illustrated in Figure 2.1. For the advection equation under consideration, $\alpha_f = (\mathbf{u}\cdot\mathbf{n})_f$. Recognizing

that $F(q_L) = (\mathbf{u} \cdot \mathbf{n})_f \; q_L$ and $F(q_R) = (\mathbf{u} \cdot \mathbf{n})_f \; q_R$, ((2.10)) can be written as:

$$F_f = \frac{1}{2}(\mathbf{u} \cdot \mathbf{n})_f (q_L + q_R) - \frac{1}{2}|(\mathbf{u} \cdot \mathbf{n})_f|(q_R - q_L) \tag{2.11}$$

The interface states q_L and q_R in the first term on the RHS of (2.11) are conventionally replaced with the respective cell-centered quantities $q_{L,c}$ and $q_{R,c}$ [56]:

$$F_f = \frac{1}{2}(\mathbf{u} \cdot \mathbf{n})_f (q_{L,c} + q_{R,c}) - \frac{1}{2}|(\mathbf{u} \cdot \mathbf{n})_f|(q_R - q_L) \tag{2.12}$$

Such a replacement is exact only for uniform, orthogonal meshes. For an unstructured mesh with higher order (second-order or higher) reconstruction of data within a cell, it would not be exact and a truncation error term would remain. However, it will be shown subsequently that the replacement is necessary (even for unstructured meshes) in order that the combined Roe-MUSCL scheme defaults to the upwind and central differencing schemes at the appropriate asymptotic limits of the flux limiter function $\psi(r)$.

The first term on the right hand side (RHS) of ((2.12)) can be interpreted as a central-differenced flux and the second term as a "diffusion" term. It is well known that the second term contributes to numerical diffusion. However, what has not been quantified thus far is the effective numerical viscosity, ν_{num}, resulting from the diffusion term. The derivation leading to an expression for ν_{num} is presented in the following discussion.

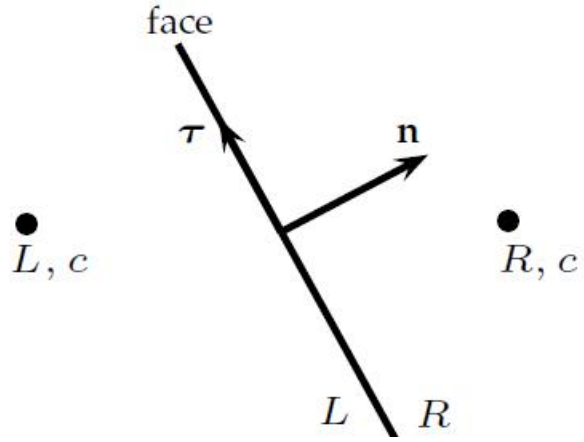

Figure 2.1: Illustration of the cell-centered and interface states at a face. L, c and R, c refer to the cell centroids on either side of the face. L and R refer to the states on either side of the interface.

2.3.1 Expression for ν_{num}

One of the characteristics of Roe's scheme is the piecewise constant representation of data within a cell, which is only first-order accurate. Van Leer extended Roe's scheme to second-order through a piecewise linear reconstruction of data on a 1-D structured grid. On an unstructured grid, however, the reconstruction step can be expressed as follows:

$$q_L = q_{L,c} + \nabla q_{L,c} \cdot \triangle \mathbf{r}_{L,f} + O(\Delta \mathbf{r}^2) \tag{2.13}$$

$$q_R = q_{R,c} + \nabla q_{R,c} \cdot \triangle \mathbf{r}_{R,f} + O(\Delta \mathbf{r}^2) \tag{2.14}$$

where $q_{L,c}$ and $q_{R,c}$ are the the values of q at the left and right cell centroids, $\nabla q_{L,c}$ and $\nabla q_{R,c}$ are the respective cell-centered gradients, and $\triangle \mathbf{r}_{L,f}$ and $\triangle \mathbf{r}_{R,f}$ are the vectors from the face centroid to the left and right cell centers, respectively.

Van Leer recognized that directly using (2.13) and (2.14) in (2.12) does not satisfy the monotonicity criterion. To ensure monotonicity, van Leer proposed the Monotonic Upstream-Centered Scheme for Conservation Laws (MUSCL) [45]. In this scheme, the contribution of cell-centered gradients to the reconstruction is limited using a function ψ, which is appropriately known as the limiter function. Using the MUSCL scheme, q_L and q_R can be written as

$$q_L = q_{L,c} + \frac{\psi}{\Lambda}\nabla q_{L,c} \cdot \triangle \mathbf{r}_{Lf} \tag{2.15}$$

$$q_R = q_{R,c} + \frac{\psi}{\Lambda}\nabla q_{R,c} \cdot \triangle \mathbf{r}_{Rf} \tag{2.16}$$

where a scaling factor Λ has been introduced in addition to the limiter ψ. Most reconstruction formulations in the literature implicitly correspond to a scaling factor $\Lambda = 1$. In this study, it is shown that $\Lambda = 2$ is more appropriate for multiple reasons. First, choosing $\Lambda = 2$ allows us to both recover the upwind scheme when $\psi = 0$ and the second-order central differencing when $\psi = 2$. In addition, it will be shown that choosing $\Lambda = 2$ ensures the TVD character of limiters when applied to 2-D (and by extension, 3-D) problems.

Substituting (2.15) and (2.16) into (2.12) gives

$$\begin{aligned} F_f &= \frac{1}{2}(\mathbf{u}\cdot\mathbf{n})_f(q_{L,c} + q_{R,c}) - \\ &\quad \frac{1}{2}|(\mathbf{u}\cdot\mathbf{n})_f|\left\{(q_{R,c} - q_{L,c}) + \frac{\psi}{\Lambda}[\nabla q_{R,c}\cdot\triangle\mathbf{r}_{R,f} - \nabla q_{L,c}\cdot\triangle\mathbf{r}_{L,f}]\right\} \quad (2.17) \\ &= F_{\mathrm{UDF}} + F_{\mathrm{ADF}} \quad (2.18) \end{aligned}$$

where

$$F_{\text{UDF}} = \frac{1}{2}(\mathbf{u}\cdot\mathbf{n})_f(q_{L,c}+q_{R,c}) - \frac{1}{2}|(\mathbf{u}\cdot\mathbf{n})_f|(q_{R,c}-q_{L,c}), \tag{2.19}$$

$$F_{\text{ADF}} = -\frac{\psi}{2\Lambda}\,|(\mathbf{u}\cdot\mathbf{n})_f|\,\{\nabla q_{R,c}\cdot\triangle\mathbf{r}_{R,f} - \nabla q_{L,c}\cdot\triangle\mathbf{r}_{L,f}\} \tag{2.20}$$

represent the upwind and anti-diffusive fluxes, respectively. It is clear from (2.17) that when $\psi = 0$, the first-order upwind scheme is obtained. It is also apparent that without replacing q_L and q_R in (2.11) with $q_{L,c}$ and $q_{R,c}$, one would not recover the upwind scheme for $\psi = 0$.

Another property that the Roe-MUSCL scheme should satisfy is that for the appropriate values of ψ and Λ, one recovers the purely central-differenced fluxes. Equations (2.15) and (2.16) suggest that for $\psi = \Lambda$, Roe-MUSCL defaults to the standard central differencing. However, from (2.19) and (2.20), it is not clear whether this is the case. The numerical viscosity formulation will, however, demonstrate that one indeed recovers the standard central-differenced flux.

Using (2.15) and (2.16) in (2.20), the anti-diffusive flux F_{ADF} can be written as

$$F_{\text{ADF}} = -\frac{\psi}{2\Lambda}\,|(\mathbf{u}\cdot\mathbf{n})_f|\,\{(q_R - q_L) - (q_{R,c} - q_{L,c})\} \tag{2.21}$$

It can be shown rigorously (see Appendix A) that $(q_R - q_L) \ll (q_{R,c} - q_{L,c})$, where $(q_R - q_L)$ is the difference between the reconstructed quantities at the interface, while $(q_{R,c} - q_{L,c})$ represents the difference between the cell-centered quantities. F_{ADF} then

becomes

$$F_{\text{ADF}} \approx \frac{\psi}{2\Lambda} \, |(\mathbf{u} \cdot \mathbf{n})_f| \, (q_{R,c} - q_{L,c}) \tag{2.22}$$

Substituting (2.22) into (2.18) and using a face-centered Taylor series expansion for $(q_{R,c} - q_{L,c})$ yields

$$\begin{aligned} F_f &\approx \frac{1}{2}(\mathbf{u} \cdot \mathbf{n})_f (q_{L,c} + q_{R,c}) - \frac{1}{2}|(\mathbf{u} \cdot \mathbf{n})_f|(q_{R,c} - q_{L,c}) + \\ &\quad \frac{\psi}{2\Lambda}|(\mathbf{u} \cdot \mathbf{n})_f|(q_{R,c} - q_{L,c}) \qquad (2.23) \\ &\approx \frac{1}{2}(\mathbf{u} \cdot \mathbf{n})_f (q_{L,c} + q_{R,c}) - \frac{1}{2} \, |(\mathbf{u} \cdot \mathbf{n})_f| \, (\mathbf{d} \cdot \mathbf{n})_f \, \left(1 - \frac{\psi}{\Lambda}\right) \, (\nabla q \cdot \mathbf{n})_f \qquad (2.24) \end{aligned}$$

It is now apparent from (2.24) that when $\psi = \Lambda$, the central-differenced flux is indeed recovered. Moreover, if the limiter ψ asymptotes to a maximum value of 2 as is the case with the superbee limiter, then to recover the central differencing scheme the scaling factor should be $\Lambda = 2$.

Treating the central-differenced and Roe's numerical diffusion fluxes in (2.24) to be the advective and diffusive fluxes, respectively, the modified governing equation that is actually being solved by the numerical scheme becomes

$$\frac{\partial q}{\partial t} + \nabla \cdot (\mathbf{u}q) - \nabla \cdot (\nu_{\text{num}} \nabla q) = 0 \tag{2.25}$$

where the numerical viscosity ν_{num} is given by

$$\nu_{\text{num}} = \frac{1}{2}|(\mathbf{u} \cdot \mathbf{n})_f| \, (\mathbf{d} \cdot \mathbf{n})_f \, \left(1 - \frac{\psi}{\Lambda}\right) \tag{2.26}$$

When $\psi = \Lambda$, the original form of the advection equation (2.3) is recovered. This is to be expected since central differencing is non-diffusive to leading order. However, when $\psi = 2$ and $\Lambda = 1$, ν_{num} is negative. This would mean that the TVD scheme is adding anti-viscosity to the governing equation being solved. As a result, when using a limiter such as superbee coupled with $\Lambda = 1$, the MUSCL scheme is susceptible to excursions beyond the extrema of the advected quantity. This study shows that this indeed the case for 2-D problems.

Numerical viscosity in (2.26) is evaluated at a cell face. The cell-centered viscosity is determined using the following interpolation scheme:

$$\nu_{\text{cell}} = \frac{\sum_{i=1}^{N_f} W_i \ \nu_{f,i}}{\sum_{i=1}^{N_f} W_i} \tag{2.27}$$

where ν_{cell} is the cell-centered viscosity, N_f is the number of faces in a cell, $\nu_{f,i}$ is the viscosity evaluated at the ith face of a cell, and W_i is the weighting factor. The weighting factor is obtained as

$$W_i = \frac{1}{|(\mathbf{x}_{\text{cell}} - \mathbf{x}_{f,i}) \cdot \mathbf{n}_i|} \tag{2.28}$$

where $\mathbf{x}_{\text{cell}}$ is the cell centroid, $\mathbf{x}_{f,i}$ is the centroid of the ith face and $\mathbf{n}_i$ is the normal to the ith face.

2.3.2 High Resolution Flux Limiters

It can be seen from (2.26) that the flux limiter ψ controls the amount of artificial diffusion being added and hence plays a critical role in determining whether a differencing scheme is TVD or not. A number of TVD limiters have been developed, principally for 1-D uniform meshes, and their extension to multi-dimensional and generalized grids is the subject of extensive ongoing research. In this section, the original 1-D, second-order TVD flux limiter schemes will be introduced, followed by a discussion of their extension to 2-D and 3-D unstructured meshes.

Sweby [57] introduced the famous TVD diagram that plots ψ as a function of r for the various flux limiters. Sweby's original TVD diagram is *similar, but not identical,* to that shown in Figure 2.2. In Figure 2.2, $\psi = 1$ and $\psi = 2$ correspond to the asymptotic limits of the minmod and superbee limiters, respectively. In this context, it is relevant to mention that most studies in the literature (cf. [4,5]) implicitly assume $\Lambda = 1$. This fact in conjunction with (2.23) tells us that in those studies, $\psi = 1$ and $\psi = 2$ correspond to CDS and downwind schemes, respectively. This would mean that when $\Lambda = 1$ and $\psi \in (1, 2]$, a net *anti-diffusion* is being supplied, as indicated by a negative ν_{num} in (2.26). In addition, there is less diffusion being added near the high-gradient regions when $\Lambda = 1$ and $\psi \in [0, 1)$. While this approach seems to maintain monotonicity on 1-D meshes, non-monotonic behavior was observed for 2-D cases [4, 5]. By choosing $\Lambda = 2$, the limits $\psi = 0$ and $\psi = 2$ would correspond to upwind differencing (UDS) and central differencing (CDS) schemes, respectively.

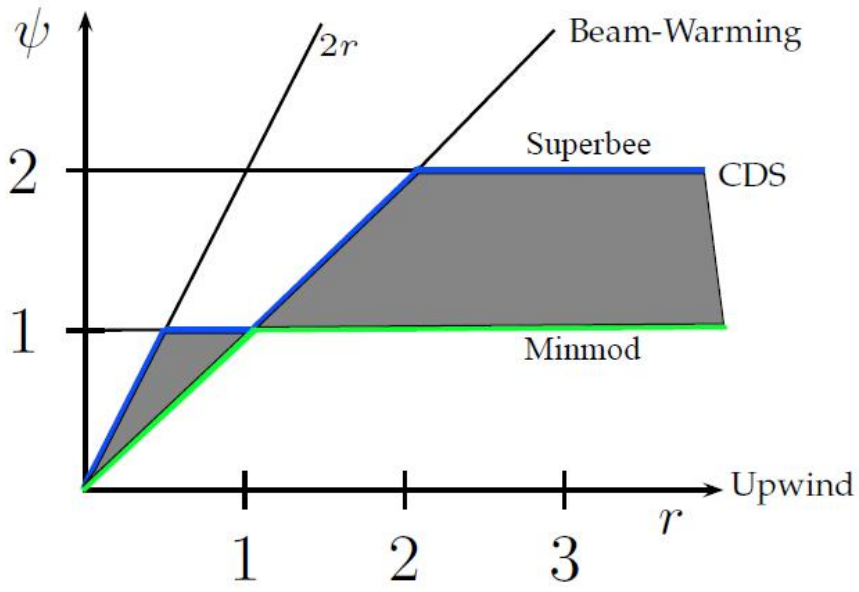

Figure 2.2: Modified Sweby diagram showing flux limiter $\psi(r)$ as a function of r for $\Lambda = 2$. The shaded region is the TVD region. The superbee and minmod limiter curves bounding the TVD region are displayed in bold.

The consequence of such a choice is that the solution will remain TVD even in multi-dimensional scenarios.

Sweby determined that in order for a limiter to be TVD, the following criterion must be satisfied:

$$0 \leq \psi(r) \leq min(2r, 2) \tag{2.29}$$

Moreover, for second-order schemes to be TVD, their limiter curves must lie in the shaded region in Figure 2.2, as well as pass through the point (1,1). Some of the early second-order linear schemes such as Lax-Wendroff and Beam-Warming are not monotonic since their ψ-r curves lie outside this shaded region. This led to the development of a number of non-linear, high resolution (HR) schemes such as minmod, superbee, and Osher among others. In fact, there can exist an infinite number of TVD

limiters whose curves lie in the shaded region. The HR limiters tested here, apart from upwind and central differencing, are as follows

Minmod: $\psi(r) = max(0, min(1, r))$

van Leer: $\psi(r) = \frac{r+|r|}{1+|r|}$

Superbee: $\psi(r) = max(0, min(1, 2r), min(2, r))$

Barth-Jesperson: $\psi(r) = 0.5(r+1)min\left(min(1, \frac{4r}{r+1}), min\left(1, \frac{4}{r+1}\right)\right)$

The Barth-Jesperson scheme presented above was obtained from Berger [58] and is equivalent to the original form that was developed for unstructured grids. It is useful to think of the superbee and minmod limiters as the boundaries of the second-order TVD region, as indicated in Figure 2.2. Superbee reaches the limit of $\psi = 2$ for $r \geq 2.0$, where it provides maximum anti-viscosity. This limit corresponds to central differencing when $\Lambda = 2$, meaning that the numerical viscosity is zero to leading order. Minmod reaches the limit of $\psi = 1$ for $r \geq 1.0$ and hence is the most diffusive of the limiters.

As discussed previously, the concept of TVD has sound theoretical basis for scalar problems on a 1-D uniform mesh. Moreover, on this grid, the original form of van Leer's MUSCL extrapolation technique when applied to variable q immediately to the left and right states at the cell interface $i + 1/2$ with the limiter ψ [31, 59] results in the following reconstructed variables

$$q^L_{i+1/2} = q_i + \frac{1}{4}\left[(1-k)\psi(r^L)(q_i - q_{i-1}) + (1+k)\psi(\frac{1}{r^L})\,(q_{i+1} - q_i)\right] \tag{2.30}$$

$$q^R_{i+1/2} = q_{i+1} + \frac{1}{4}\left[(1-k)\psi(r^R)(q_{i+2} - q_{i+1}) + (1+k)\psi(\frac{1}{r^R})\,(q_{i+1} - q_i)\right] \tag{2.31}$$

where k is a free parameter between -1 and 1. When $k = -1$ or 0, the formulation reduces to upwind or central difference scheme, respectively. The dimensionless quantities r^L and r^R are the ratio of consecutive gradients defined as:

$$r^L = \frac{q_{i+1} - q_i}{q_i - q_{i-1}} \tag{2.32}$$

$$r^R = \frac{q_{i+1} - q_i}{q_{i+2} - q_{i+1}} \tag{2.33}$$

It is clear from the above expressions that r^L and r^R require nodal information at two cell centroids upstream and downstream of a face, respectively which are typically not available for second-order schemes on unstructured meshes. Therefore, extending this formulation to multidimensional unstructured meshes requires developing a modified expression for the r-factor.

The first step in developing an r-factor for a general mesh involves replacing the index-based notation by the following unstructured grid-based notation [4, 5, 50]:

$$r_f = \frac{q_{L,c} - q_V}{q_{R,c} - q_{L,c}} \tag{2.34}$$

where L, c and R, c are the cell centroids to the left and right of interface f, and V is the virtual node located upstream of L, c as shown in Figure 2.3. Since (2.34) is simply an extension of (2.32) and (2.33) to arbitrary meshes, the virtual node is located along the line segment connecting R, c and L, c such that node L, c is equidistant from R, c and V. Moreover, V need not coincide with the cell centroid located upstream of L, c.

The next step is to find an accurate approximation for the numerator in (2.34) containing the virtual node V. A number of researchers have proposed models to deal with this node. Bruner [50, 51] was the first to develop a modified form of the r-factor

$$r_{f,\text{Bruner}} = \frac{q_{L,c} - q_V}{q_{R,c} - q_{L,c}} \approx 2\frac{q_f - q_{L,c}}{q_{R,c} - q_{L,c}} \tag{2.35}$$

$$= \frac{2\triangle \mathbf{r} \cdot \nabla q|_{L,c}}{q_{R,c} - q_{L,c}} \tag{2.36}$$

However, this approximation is incorrect since the TVD condition is not recovered when r is reduced to the 1-D form. Darwish and Moukalled [4] proposed the following so-called "exact r formulation" which does recover the 1-D r formulations (2.32) and (2.33):

$$r_f = \frac{q_{L,c} - q_V}{q_{R,c} - q_{L,c}} = \frac{(q_{R,c} - q_V) - (q_{R,c} - q_{L,c})}{q_{R,c} - q_{L,c}} \tag{2.37}$$

where $(q_{R,c} - q_V)$ is expressed as (see Figure 2.3)

$$(q_{R,c} - q_V) \approx \nabla q_{L,c} \cdot \mathbf{r}_{V \to R,c} = 2\nabla q_{L,c} \cdot \mathbf{r}_{L,c \to R,c} \tag{2.38}$$

Substituting (2.38) into (2.37), the following expression for r was obtained

$$r = \frac{(2\nabla q_{L,c} \cdot \mathbf{r}_{L,c \to R,c})}{q_{R,c} - q_{L,c}} - 1 \tag{2.39}$$

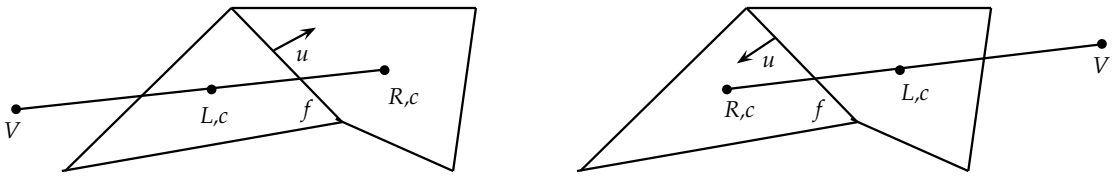

Figure 2.3: Unstructured meshes showing the dependence of the location of virtual node V on the direction of flow indicated by u.

The current study utilizes this form of r for the 1-D and 2-D simulations on both orthogonal and triangular meshes.

2.4 Results

The numerical viscosity ν_{num} in the advection equation has been quantified and compared for four limiters—minmod, van Leer, superbee and Barth-Jesperson—using four canonical problems from the literature: 1-D advection of a step function profile [3] on uniform grids, and 2-D advection of step, sinusoidal, and double-step profiles [4, 60] on both structured (orthogonal) and unstructured (triangular) grids. Results presented include the profiles of the advected quantity, and both the magnitude and spatial distribution of the numerical viscosity for the limiters considered. The effects of the scaling parameter Λ are also discussed.

2.4.1 1-D Step Function

This case consists of a 1-D step function advected with the constant velocity $\mathbf{u} = (u_x, u_y, u_z) = (1, 0, 0)$ on two uniform grids with 256 and 1024 cells. The step function was initialized with the discontinuity located at the inlet boundary ($x = 0$).

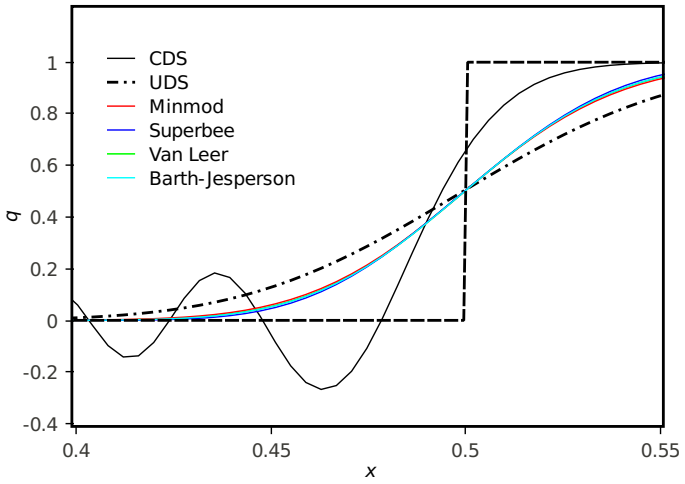

Figure 2.4: Comparison of profiles of the advected quantity q computed using UDS, CDS and the four flux limiters for the case of 1-D step profile on the 256-cell mesh with $\Lambda = 2$. Dashed line represents the exact profile.

The test conditions and the mesh are the same as those in Alves et al. [3]. The step function was advected till time $t = 0.5$, at which point it should have moved by a distance of 0.5.

Figures 2.4 and 2.5 show the profiles of the advected quantity q for the four limiters under consideration, as well as for the first-order upwind differencing scheme (UDS) and the second-order central differencing scheme (CDS). The profiles are for for $\Lambda = 2$ and 1, respectively, on the 256 cell mesh. As expected, CDS shows unstable behavior with spurious oscillations near the minimum, and UDS is observed to be the most diffusive scheme. The CDS profile is not shown in Figure 2.5. For a given limiter, it is seen that the profiles for $\Lambda = 2$ are more diffusive than those for $\Lambda = 1$. This is because it can be seen from (2.26) that $\Lambda = 2$ results in greater numerical viscosity. However, the significance of $\Lambda = 2$ is that it ensures monotonicity even when

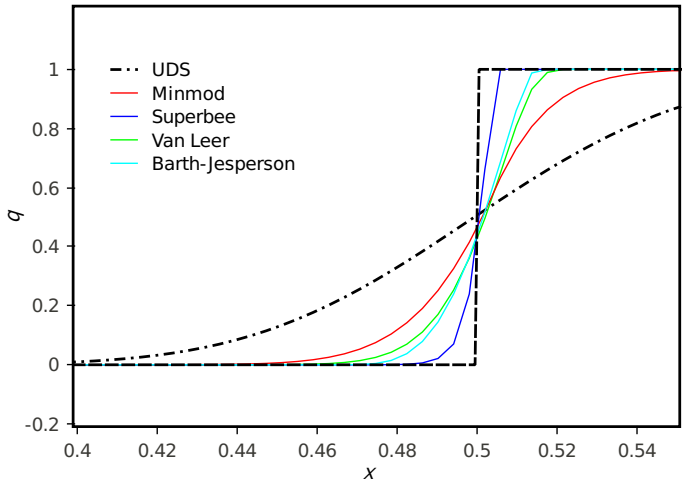

Figure 2.5: Comparison of q with the same limiters as in Figure 2.4 but with $\Lambda = 1$.

extending the Roe-MUSCL scheme and the various limiters to multi-dimensional problems, whereas $\Lambda = 1$ does not ensure monotonicity (to be demonstrated in the 2-D cases that follow). From Figure 2.4, it can be seen that when $\Lambda = 2$, the profiles for the various limiters are quite close to each other. However, the numerical viscosity plots will clarify that even when $\Lambda = 2$, minmod and superbee are the most and least diffusive, respectively. But when $\Lambda = 1$, it is clear from Figure 2.5 that minmod is the most diffusive and superbee is the least diffusive among the flux limiters considered.

Numerical viscosity ν_{num} as a function of the spatial location x is shown for the two meshes in Figure 2.6(a) and Figure 2.6(b). Also included are the UDS and CDS schemes, which will serve as the upper and lower limits for the numerical viscosity when $\Lambda = 2$. It is clear from figures Figure 2.6(a) and Figure 2.6(b) that UDS is the most diffusive, with the viscosity being uniform throughout the spatial domain. To leading order, CDS provides zero viscosity and is hence not discernible in the plots.

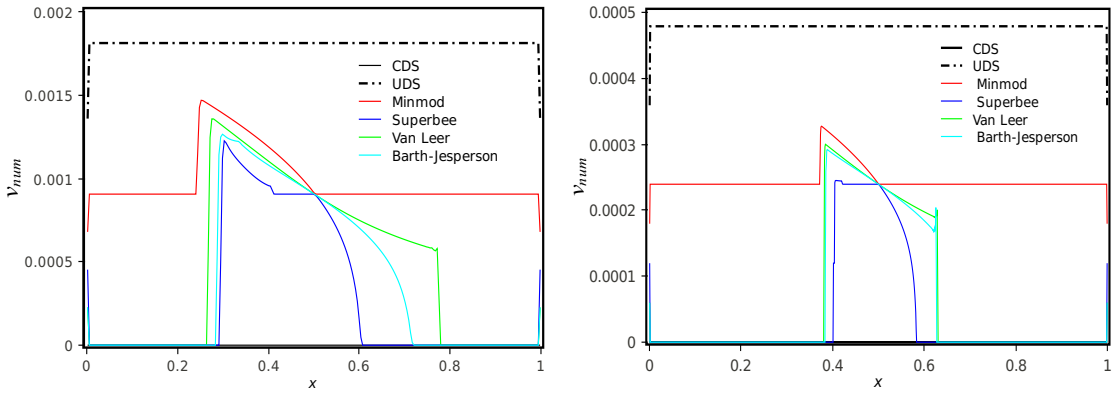

(a) 256 cells

(b) 1024 cells

Figure 2.6: Comparison of the numerical viscosity profiles for UDS, CDS and the four flux limiters for the case of 1-D step profile for $\Lambda = 2$: (a) 256-cell mesh and (b) 1024-cell mesh.

Among the flux limiters considered, minmod is the most diffusive and superbee is the least diffusive. Another salient feature of superbee is that it is most active around the discontinuity and is nearly zero away from it. The Barth-Jersperson and van Leer limiters are also confined to the region near the discontinuity, but are less so than superbee. Interestingly, minmod is not only the most diffusive limiter, but is also active throughout the spatial domain. For the flux limiters under consideration, the magnitude of the numerical diffusion is higher upstream of the discontinuity than downstream, indicating that the solution is more unstable in the upstream region. This is also confirmed in Figure 2.4, where the oscillations in the CDS solution occur predominantly in the region upstream of the discontinuity. Figure 2.6(b) shows that with grid refinement, both the magnitude and spatial extent of the numerical viscosity are decreased, although the overall trends are similar to those for the coarser mesh.

For validation purposes, the advected scalar profiles from our study are compared with the data from the study of Alves et al. [3]. Their study considered high resolution schemes such as minmod and SMART, in addition to UDS, second-order CDS, fourth-order CDS and cubic spline schemes. The numerical scheme used is a multiresolution adaptive mesh approach that is unconditionally bounded and allows for grid adaptation in regions of strong gradients. They also adopted the Normalized Variable Space Formulation (NSVF) of Darwish and Moukalled [4] in which a normalized face flux is utilized to compute the actual interface flux. Figure 2.7 shows a comparison of the scalar profiles for UDS, second-order CDS and minmod schemes. There is excellent agreement for both UDS and CDS. For $\Lambda = 1$, the minmod profile from the current study shows excellent agreement with that of [3]. Note that the study [3] implicitly assumes $\Lambda = 1$. As expected, the minmod profile for $\Lambda = 2$ from the current study was found to be more diffused compared to the profile from [3].

2.4.2 2-D Results

In this section, the results are presented for the advection of the 2-D step, sinusoidal and double-step profiles on uniform orthogonal and unstructured triangular meshes. Profiles of the advected scalar and the numerical viscosity are presented for the four TVD limiters, as well as for the UDS and CDS schemes.

2.4.2.1 2-D Step Profile.

The domain consists of a 2-D square region of side unity. The step function was initialized with the discontinuity located at the left inlet boundary ($x = 0$)

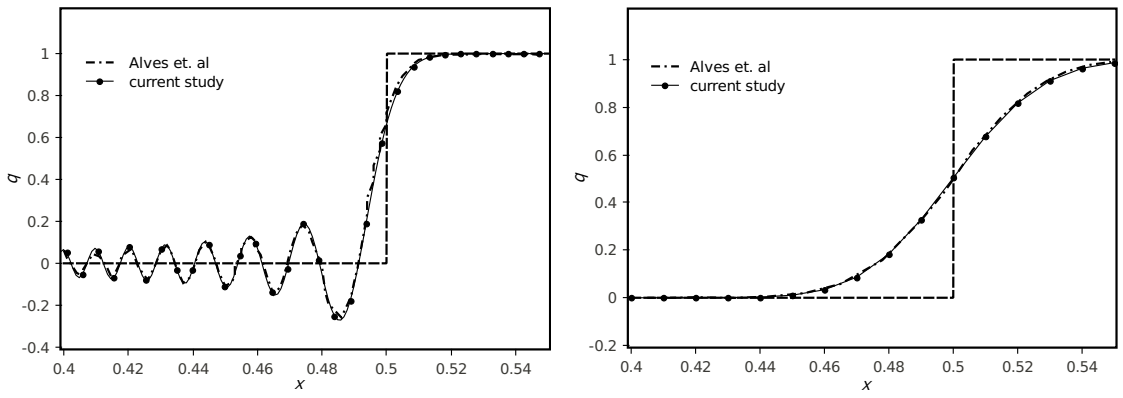

(a) CDS

(b) UDS

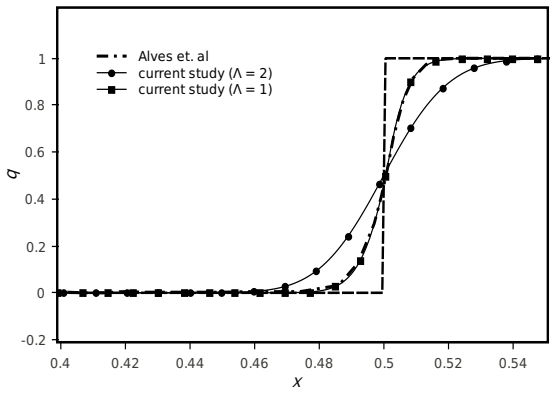

(c) Minmod

Figure 2.7: Comparison of q profiles from the current study with those from [3] for the case of 1-D step profile. Profiles are compared for the following schemes: (a) CDS, (b) UDS, and (c) Minmod for $\Lambda = 2$ and 1. Mesh consists of 1024 cells.

and was advected with a constant velocity $\mathbf{u} = (1, 1, 0)$. Two uniform orthogonal meshes consisting of 46×46 and 249×249 cells, and an unstructured mesh with 2150 triangular cells were considered. The number of cells in the triangular mesh was chosen to enable comparison of results with the 46×46 mesh. The simulation was conducted till the step function had traversed through the entire domain, at which point the solution could be considered independent of time. The steady-state contour plots of q for UDS and the superbee scheme on the 46×46 orthogonal grid

are presented in Figure 2.8. It is clear that the boundary between the maximum and minimum values of the step function, which should have been the diagonal of the square, has diffused due to the numerical diffusion in both UDS and superbee. The diffusion of this boundary increases as one moves from the lower left corner to the upper right corner, with the diffusion being greater for UDS than for superbee. A similar smearing can also be seen for the simulations conducted on the triangular mesh.

The profiles of q at the $y = 0.8$ cross-section are shown in Figure 2.9(a) for the 46×46 mesh and in Figure 2.9(b) for the 2150 cell triangular mesh. It is clear from Figure 2.9(a) that CDS generates oscillations on both sides of the discontinuity, in contrast to the 1-D step case where the oscillations were principally confined to the upstream region of the discontinuity. However, for the triangular mesh case in Figure 2.9(b), the oscillations are clearly diminished and primarily occur in the upstream region of the step. Although the superbee profile is the least diffused, the differences in the profiles of the various limiters are small due to the use of $\Lambda = 2$.

The numerical viscosity profiles at $y = 0.8$ for the various schemes are presented in Figure 2.10. For the orthogonal meshes, the numerical viscosity profiles, shown in Figure 2.10(a) and Figure 2.10(b), are nearly symmetric close to the discontinuity. This suggests that to maintain monotonicity, equal amounts of numerical diffusion were needed on either side of the step. As in the 1-D case, the coarser 46×46 mesh results in the numerical viscosity being applied over a wider region of the domain. It is also clear that superbee provides the least amount of viscosity and

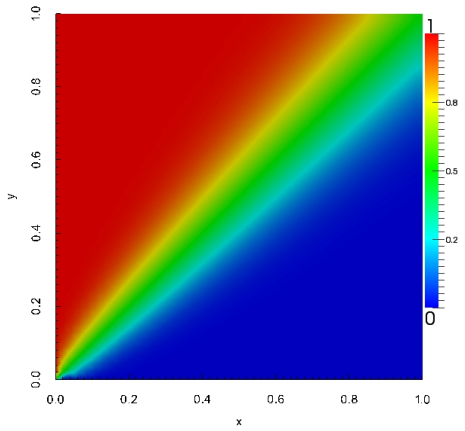

(a) UDS

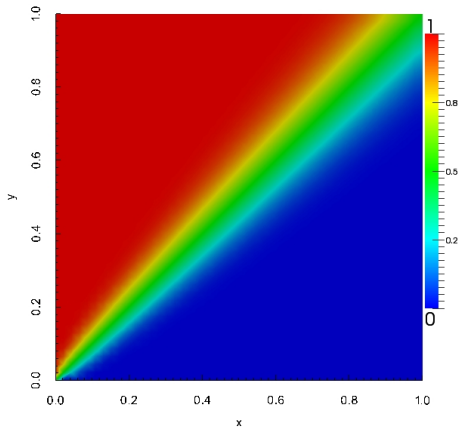

(b) Superbee

Figure 2.8: Contour plots of the advected scalar q for the 2-D step profile case. (a) UDS and (b) Superbee scheme. Results are for the 46×46 orthogonal mesh and $\Lambda = 2$.

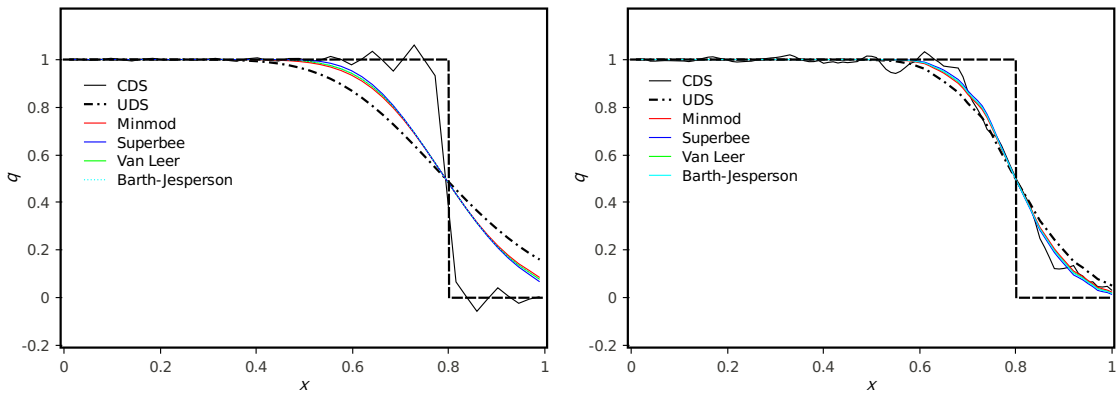

(a) 46×46 cells

(b) 2150 triangular cells

Figure 2.9: Comparison of profiles of the advected quantity q computed using UDS, CDS and the four flux limiters for the case of 2-D step profile: (a) mesh with 46×46 cells and (b) mesh with 2150 triangular cells. Plots are for the cross-sectional location $y = 0.8$ and $\Lambda = 2$.

is activated over a narrow region around the discontinuity, while the opposite is true for minmod. The diffusivities of the other two limiters are nearly the same.

For the triangular mesh, the ν_{num} profiles are shown in Figure 2.10(c). It is seen that the numerical diffusivities are no longer confined to the region around the discontinuity and are also not symmetrically distributed. Near the discontinuity, the minmod and superbee limiters again provide the maximum and minimum numerical diffusivities, respectively. This trend is generally true away from the discontinuity as well. Another interesting feature is that the magnitudes of the numerical diffusivities for the triangular mesh are in general smaller than those for the corresponding 46×46 structured mesh. This is because the ν_{num} profile depends not only on the limiter ψ, but also on the dot product $\mathbf{u} \cdot \mathbf{n}$ at a cell face. For this particular problem, the velocity is directed along the diagonal of the square domain. As a result, $|\mathbf{u} \cdot \mathbf{n}|$ for

the orthogonal mesh will, in general, be greater than that for the triangular mesh. Consequently, in this case, for nearly the same grid resolution, the orthogonal mesh provides greater numerical viscosity than the triangular mesh.

It is also important to point out that the magnitude of the numerical viscosity is highly sensitive to the denominator in the r-factor expression of Darwish and Moukalled (see (2.39)), which is simply the difference in the state quantities on either side of an interface. If, for example, this difference is very small or zero, which is typically the case away from the discontinuity, the r-factor is assigned an incorrect value. The error in r then propagates to not just the flux limiter ψ which depends on r but also to the numerical viscosity computed using (2.26). Therefore, diffusion may be added unnecessarily at locations where it is not needed. In order to ensure that unwanted diffusion is not being added, the r-factor expression is applied only when the difference in the state quantities on either side of a face is larger than a threshold value of $\epsilon = 10^{-5}$. When the difference is lower than ϵ, r is set to a very large number to ensure that $\psi(r) \approx 2$, which as Figure 2.2 indicates is CDS. Simulations were also conducted for $\epsilon = 10^{-10}$ and 10^{-15}, but these values resulted in large amounts of numerical viscosity being applied far away from the discontinuity.

To validate the current results, the scalar profiles from the 46×46 orthogonal mesh and the 2150 triangular cell mesh are compared against the data of Darwish and Moukalled [4] for the minmod and superbee limiters (see Figure 2.11). Darwish and Moukalled used a 2-D mesh consisting of 2094 triangular cells. Results from the current study are presented for both $\Lambda = 2$ and $\Lambda = 1$. It is to be noted that in [4], $\Lambda = 1$ implicitly. There is excellent agreement between the current $\Lambda = 1$ profiles and

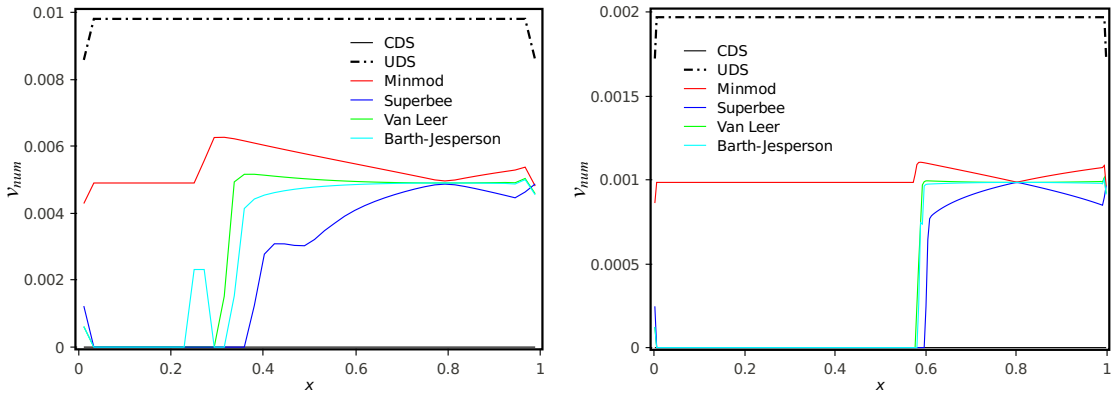

(a) 46×46 cells

(b) 249×249 cells

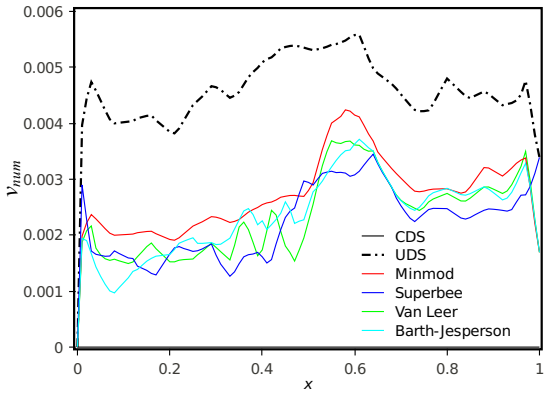

(c) 2150 triangular cells

Figure 2.10: Comparison of numerical viscosity profiles for UDS, CDS and the four flux limiters for the case of 2-D step profile: (a) 46×46 mesh, (b) 249×249 mesh and (c) 2150 triangular cell mesh. Plots are shown for the cross-sectional location $y = 0.8$ and $\Lambda = 2$.

those of Darwish and Moukalled. The $\Lambda = 2$ profiles are more smeared than those for $\Lambda = 1$, but are universally TVD. However, $\Lambda = 1$ does not necessarily preserve monotonicity as seen in Figure 2.11(b). This can be explained based on (2.26). It is clear from this equation that when $\Lambda = 1$ and $\psi = 2$, ν_{num} is negative, meaning that anti-diffusion is being added to the system. The addition of anti-diffusion occurs in regions where $\psi = 2$, i.e. in the regions away from the discontinuity. Therefore,

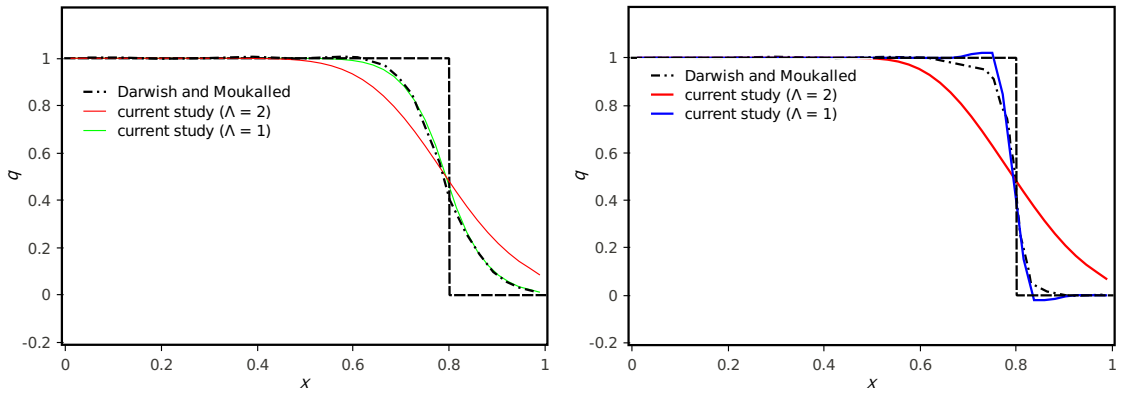

(a) Minmod (46×46 cells)

(b) Superbee (46×46 cells)

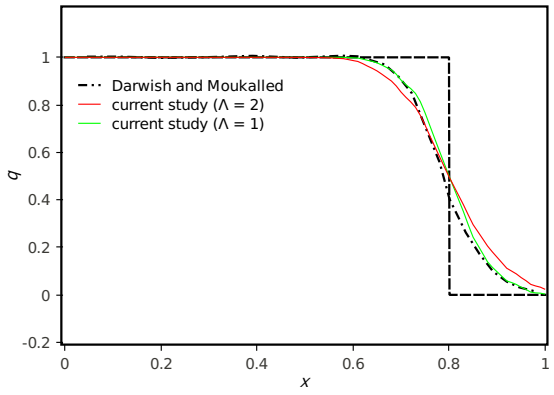

(c) Minmod (2150 triangular cells)

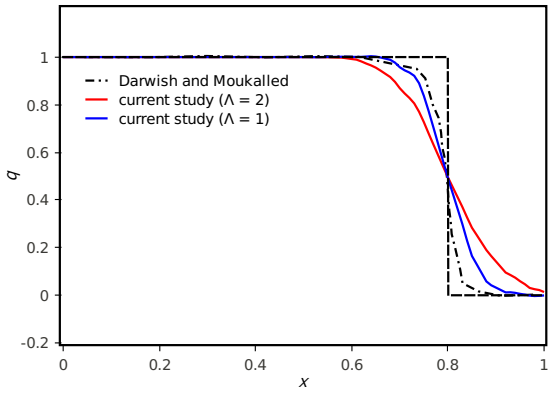

(d) Superbee (2150 triangular cells)

Figure 2.11: Comparison of q profiles from the current study with those from Darwish and Moukalled [4] for the case of 2-D step profile. Profiles are compared for the minmod and superbee schemes on: (a and b) 46×46 orthogonal mesh, and (c and d) 2150 triangular cell mesh.

one would observe oscillations in the regions away from the discontinuity, as seen in Figure 2.11(b). (In Figure 2.11(b), the Darwish and Moukalled profile uses a triangular mesh, where as the $\Lambda = 2$ curve is for an orthogonal mesh.)

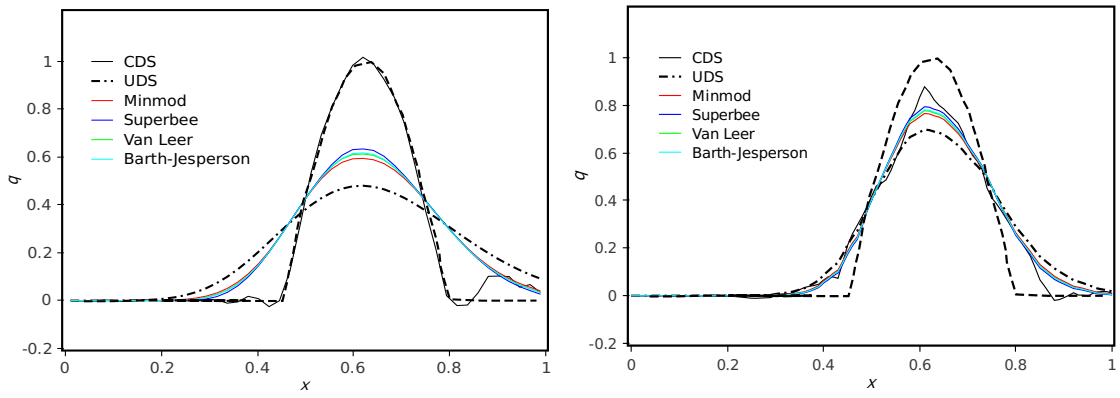

(a) 46×46 cells (b) 2150 triangular cells

Figure 2.12: Comparison of q profiles computed using UDS, CDS and the four flux limiters for the case of 2-D sinusoidal profile: (a) mesh with 46×46 cells and (b) mesh with 2150 triangular cells. Plots are shown for the cross-sectional location $y = 0.8$ and $\Lambda = 2$. Dashed line represents the exact profile.

2.4.2.2 2-D Sinusoidal Profile.

The domain is again a 2-D square region of side unity. The sinusoidal profile initialized at the left inlet boundary ($x = 0$) is given by [4]

$$q = \begin{cases} \sin\left[\frac{\pi}{2}\max\left(1 - \frac{|y-0.1707|}{0.1707}, 0\right)\right], & 0 \leq y \leq 0.3414 \\ 0, & \text{otherwise} \end{cases} \tag{2.40}$$

The profile was advected with the same velocity as the 2-D step function: $\mathbf{u} = (1, 1, 0)$. The steady-state results for the six numerical schemes (including UDS and CDS) at $y = 0.8$ are presented in Figure 2.12. Results shown are for the 46×46 orthogonal and 2150 triangular cell meshes, both when $\Lambda = 2$.

Numerical viscosity profiles for the 46×46 and 249×249 orthogonal meshes as well as the triangular mesh are presented in Figure 2.13. There is a sharp spike

in the numerical viscosity at $x \approx 0.65$ for all the limiters, particularly for the finer orthogonal mesh. This spike corresponds to the location where the sinusoidal profile peaks. Also, the magnitude of ν_{num} decreases by a factor of about 5 with increased grid resolution. Comparing Figure 2.13 with Figure 2.10(a) and Figure 2.10(b), it can be noted that ν_{num} magnitude for the current case is more than that for the 2-D step profile, especially in the region around the peak. This indicates that the sinusoidal profile is actually more challenging to simulate than the step profile due to a combination of high gradient regions and the extremum point. As a result, the sinusoidal profile requires additional diffusion near the peak to keep the solution not only stable but also TVD. For the triangular mesh (Figure 2.13(c)), the ν_{num} for the various limiters peaks at $x \approx 0.55$. Similar to the 2-D step case, the magnitude of ν_{num} for the triangular mesh is smaller compared to that for the coarser orthogonal mesh. As explained before, this trend can be attributed to the fact that in the current case, $|\mathbf{u} \cdot \mathbf{n}|$ for the orthogonal mesh will, in general, be greater than that for the triangular mesh.

In Figure 2.14, the scalar profiles for the minmod and superbee schemes are compared with the corresponding profiles of Darwish and Moukalled [4]. There is good agreement between the current $\Lambda = 1$ profiles and those of Darwish and Moukalled. The current $\Lambda = 2$ profiles are more smeared than those for $\Lambda = 1$, but are universally TVD. It can be seen from Figure 2.14(b) that when $\Lambda = 1$, both the current and the Darwish and Moukalled superbee profiles are not monotonic. Similarly, Figure 2.14(d) shows that Darwish and Moukalled's superbee profile does not maintain monotonicity. This is again attributable to the fact that $\Lambda = 1$ implicitly in their study. It is clear

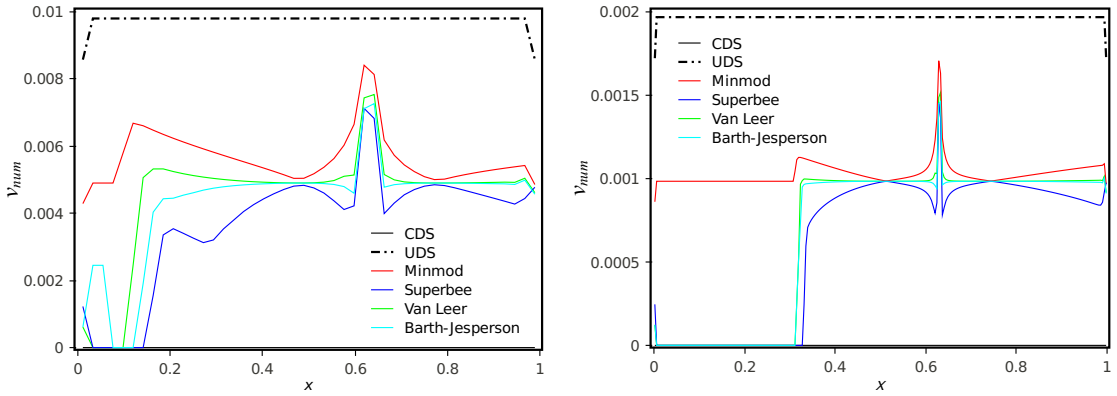

(a) 46×46 cells

(b) 249×249 cells

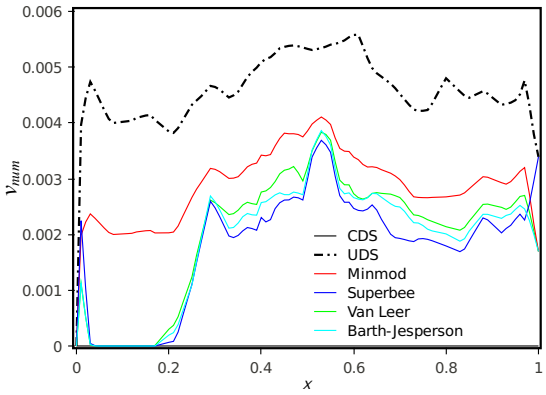

(c) 2150 triangular cells

Figure 2.13: Comparison of numerical viscosity profiles for UDS, CDS and the four flux limiters for the case of 2-D sinusoidal profile: (a) mesh with 46×46 cells, (b) 249×249 cells and c) 2150 triangular cells. Plots are shown for the cross-sectional location $y = 0.8$ and $\Lambda = 2$.

from (2.26) that for $\Lambda = 1$ and $\psi = 2$, ν_{num} is negative, meaning that anti-diffusion is being added to the system. The addition of anti-diffusion would lead to oscillations as observed for the Darwish and Moukalled's superbee profiles and also the $\Lambda = 1$ profiles from the current study.

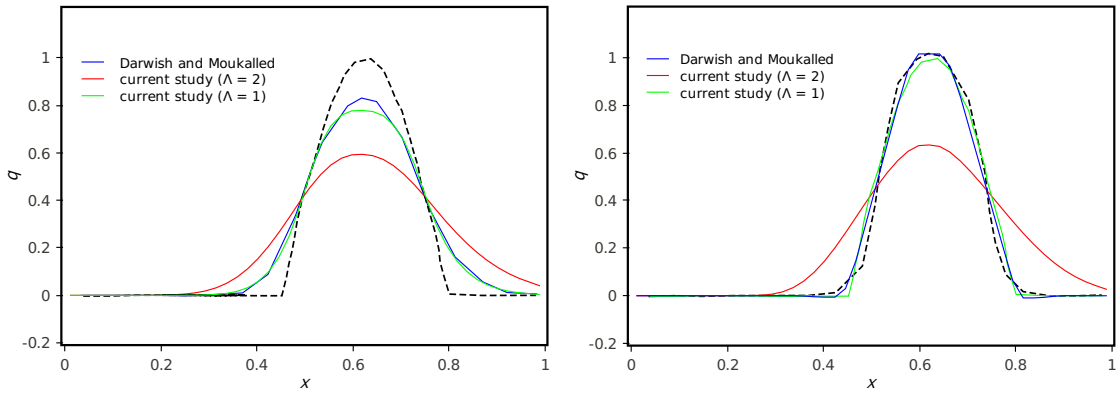

(a) Minmod (46×46 cells)

(b) Superbee (46×46 cells)

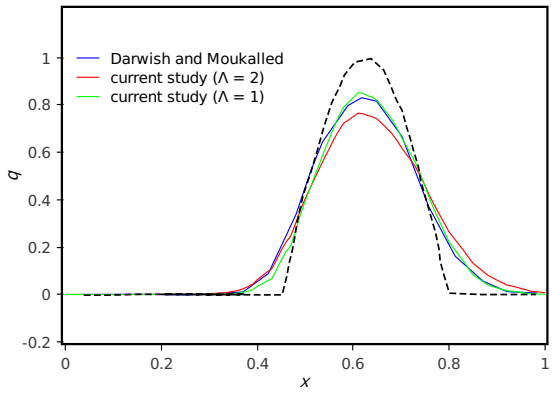

(c) Minmod (2150 triangular cells)

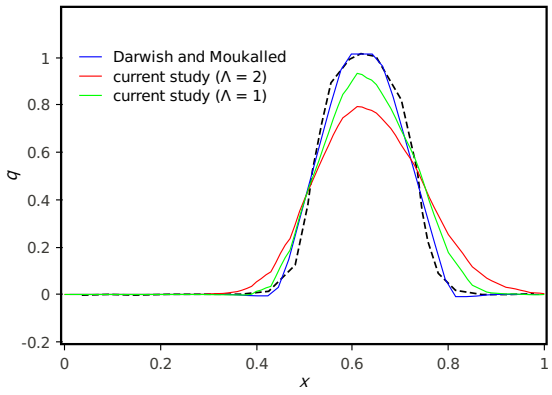

(d) Superbee (2150 triangular cells)

Figure 2.14: Comparison of q profiles from the current study with those from Darwish and Moukalled [4] for the case of 2-D sinusoidal profile. Profiles are compared for the minmod and superbee schemes on the (a and b) 46×46 orthogonal mesh, and (c and d) 2150 triangular cell mesh.

2.4.2.3 Double-Step Profile.

The double-step profile initialized at the left inlet boundary is given by

$$q = \begin{cases} 1 & 0 \leq y \leq 0.3 \\ 0 & y > 0.3 \end{cases} \tag{2.41}$$

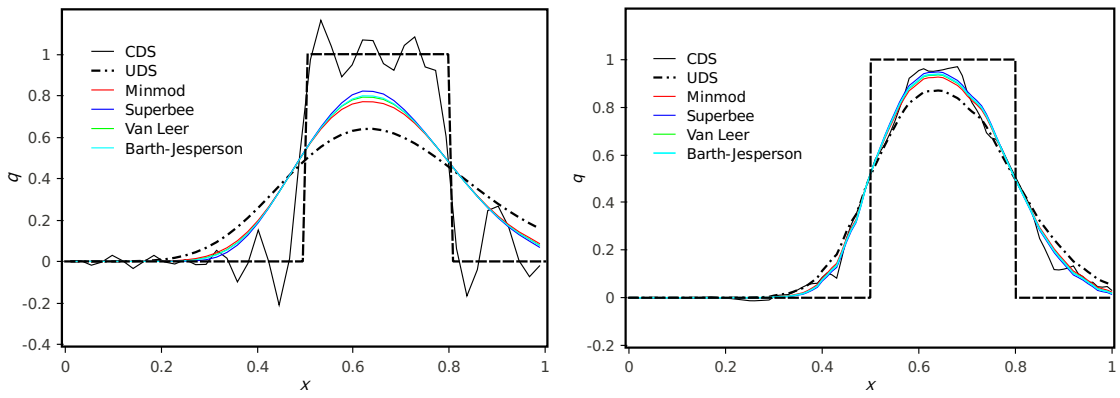

(a) 46x46 cells

(b) 2150 triangular cells

Figure 2.15: Comparison of q profiles computed using UDS, CDS and the four flux limiters for the case of 2-D double-step profile: (a) mesh with 46×46 cells and (b) mesh with 2150 triangular cells. Plots are shown for the cross-sectional location $y = 0.8$ and $\Lambda = 2$.

The steady-state profiles at $y = 0.8$ for the six numerical schemes are plotted in Figure 2.15 for the 46×46 and 2150 triangular meshes. The trends are similar to those for the 2-D step and sinusoidal cases. The numerical viscosity profiles for the orthogonal meshes are shown in Figure 2.16(a) and Figure 2.16(b), respectively. Similar to the 2-D sinusoidal profile case, these profiles show a sharp spike near the peak in the advected scalar profile. The numerical viscosity profile for the unstructured grid (Figure 2.16(c)) shows similar behavior as for the 2-D sinusoidal case.

To validate our results, the advected scalar profiles were compared against those of Li et al. [5]. In that study, a new r-factor formulation was presented that requires information from two cells upstream of a face instead of just one cell as in [4]. We performed simulations on two 3-D mesh systems that are nearly identical to those in Li et al. [5]: an orthogonal mesh with $20 \times 20 \times 5$ cells and an unstructured

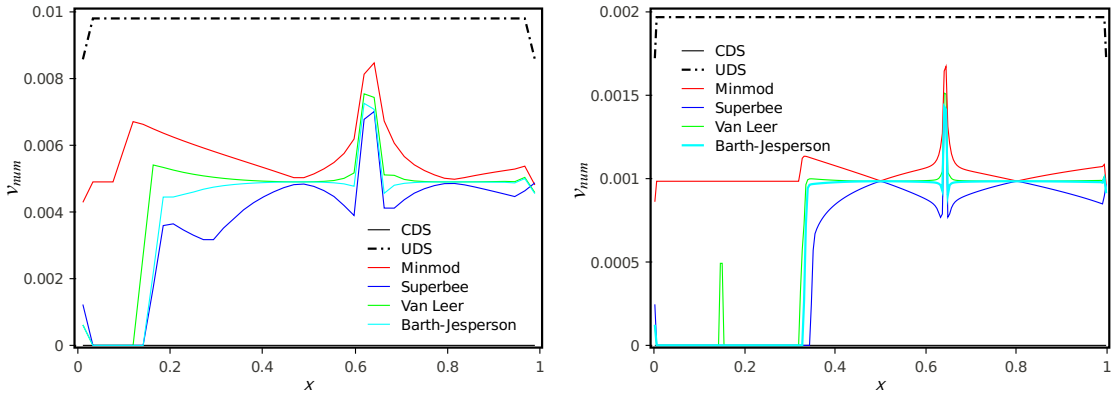

(a) 46x46 cells

(b) 249x249 cells

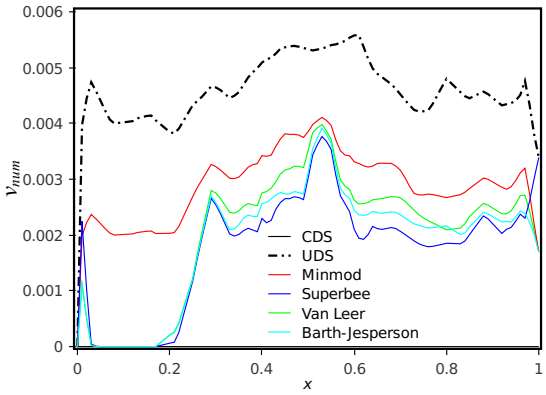

(c) 2150 triangular cells

Figure 2.16: Comparison of numerical viscosity profiles for UDS, CDS and the four flux limiters for the case of 2-D double-step profile: (a) 46×46 cell mesh, (b) 249×249 cell mesh, and c) 2150 triangular cell mesh. Plots are shown for the cross-sectional location $y = 0.8$ and $\Lambda = 2$.

mesh consisting of 7261 triangular cells. In Figure 2.17(a), the superbee profiles at $y = 0.8$ from the current simulations are compared with the profiles from [5]. Also included is the profile obtained using Darwish and Moukalled's r-factor. For the current study, the profiles are presented for both $\Lambda = 2$ and $\Lambda = 1$. It is clear from Figure 2.17(a) that the Li et al. profile, the Darwish and Moukalled profile, and the current profile for $\Lambda = 1$ all show non-monotonic behavior. Only the current profile

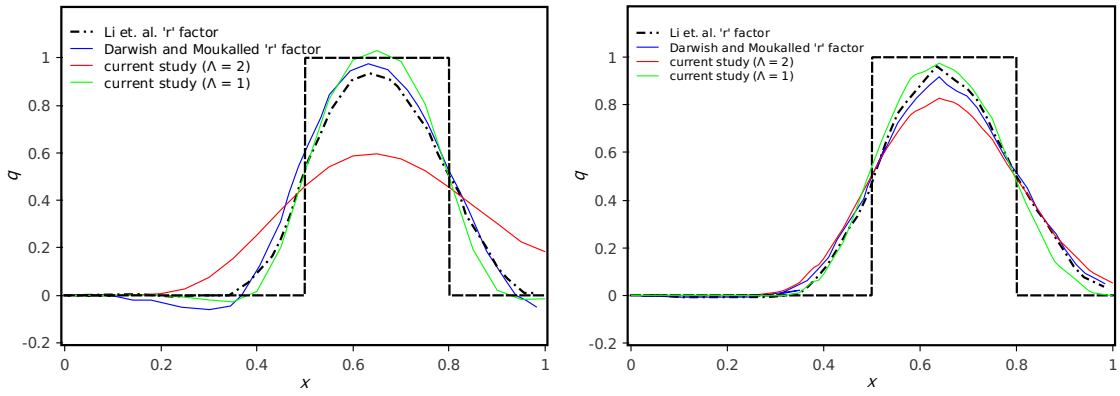

(a) Superbee ($20 \times 20 \times 5$ cells) (b) Superbee (7261 triangular cells)

Figure 2.17: Comparison of q profiles from the current study with those from Li et al. [5] for the case of 2-D double-step profile. Profiles are compared for the superbee scheme on (a) $20 \times 20 \times 5$ orthogonal mesh, and (b) 7261 triangular cell mesh.

for $\Lambda = 2$ is monotonic throughout the domain, which is achieved at the cost of increased smearing of the profile. Similar trends are seen in Figure 2.17(b) as well. However, the non-monotonicity is significantly reduced for the triangular mesh.

CHAPTER 3

EULER EQUATIONS

3.1 Introduction

The governing equations of gas dynamics are the Euler equations in compressible form. The system of equations together with the ideal gas equation of state govern the motion of inviscid fluids [6]. In general, for any non-linear, hyperbolic system of conservation laws of the form

$$\mathbf{Q}_t + \mathbf{F}_x = 0 \tag{3.1}$$

with the following initial conditions

$$\mathbf{Q}(x, t = 0) = \mathbf{Q}_0(x) \tag{3.2}$$

where $\mathbf{Q}$ is a vector of conserved variables and $\mathbf{F}$ is the non-linear flux function in the x direction, solvers based on Riemann's initial value problem (IVP) are considered to be the foundation of numerical methods in the finite volume framework [61]. The non-linearity of the governing equations allows for the existence of discontinuities in

the flow-field. Consequently, the numerical solution must converge to a weak solution. According to Lax-Wendroff theorem [62] any weak solution is considered valid if it satisfies the following Rankine-Hugoniot jump condition. This can only be achieved if the numerical method is in discrete conservation form

$$u\,[\mathbf{Q}] + [\mathbf{F}] = 0 \tag{3.3}$$

where u is the speed of the discontinuity and [.] denotes jump across it. The theorem does not guarantee that a weak solution obtained using the conservative method satisfies the entropy condition. Hence, numerical schemes must be capable of supplying correct amount of artificial viscosity for ensuring proper entropy change across discontinuities. Across a shock wave, the following entropy rise must be satisfied in a discrete sense [36], [63]

$$\Delta S = -\left.\frac{\partial^2 p}{\partial V^2}\right|_S \frac{\Delta u^3}{12T} \tag{3.4}$$

It can be argued that the artificial viscosity arising from the discretization of the convective fluxes is necessary and physical in order to obtain correct entropy rise across shocks.

In this dissertation, the convective fluxes of the 3-D conservative form of Euler equations are discretized using Roe's shock-capturing scheme [40]. Roe's upwind scheme is highly robust and has been utilized with much success in a wide range of practical flow problems. After a discussion of popular Riemann solvers and the approaches and challenges involved in extending them to three dimensions, an approach

to extending Roe's scheme to three dimensions and to second-order using van Leer's MUSCL extrapolation technique are presented. A scalar expression for numerical viscosity of the high-resolution scheme is then derived following the procedure outlined in Chapter 2. Subsequently, three TVD limiters (minmod, superbee and van Leer) are investigated for the 1-D shock-tube and 2-D inviscid supersonic wedge flows. Spatial profiles of numerical viscosities are plotted, which provide insights into the role of these limiters in controlling the dissipative nature of Roe's flux while maintaining monotonicity and stability in regions of high gradients.

Like all shock-capturing schemes, Roe's solver suffers from the problem of being excessively dissipative for turbulent flows. Hence, modifications to the dissipative portion of the scheme are needed to yield accurate results. In this study, the modifications proposed by Thornber et al. [9] and Bidadi and Rani [64] are discussed. A thorough investigation of the corrections are examined for two fundamental test problems concerning turbulent and transitional flows in subsequent chapters: (i) decaying compressible isotropic turbulence (Chapter 4), and (ii) Taylor-Green vortex (Chapter 5). The purpose is to demonstrate why ILES using shock-capturing schemes such as Roe's are capable of successfully capturing the physics of both flows.

3.2 Governing Equations

The 3-D Euler equations in conservative form are:

$$\frac{\partial \mathbf{Q}}{\partial t} + \frac{\partial \mathbf{F}}{\partial x} + \frac{\partial \mathbf{G}}{\partial y} + \frac{\partial \mathbf{H}}{\partial z} = 0 \tag{3.5}$$

$$\mathbf{Q} = \begin{bmatrix} \rho \\ \rho u \\ \rho v \\ \rho w \\ \rho e_t \end{bmatrix}, \quad \mathbf{F} = \begin{bmatrix} \rho u \\ \rho u^2 + p \\ \rho uv \\ \rho uw \\ \rho u e_t + pu \end{bmatrix}, \quad \mathbf{G} = \begin{bmatrix} \rho v \\ \rho vu \\ \rho v^2 + p \\ \rho vw \\ \rho v e_t + pv \end{bmatrix}, \quad \mathbf{H} = \begin{bmatrix} \rho w \\ \rho wu \\ \rho wv \\ \rho w^2 + p \\ \rho w e_t + pw \end{bmatrix} \tag{3.6}$$

The total energy e_t is given by

$$e_t = c_p T - \frac{p}{\rho} + \frac{1}{2}(u^2 + v^2 + w^2) \tag{3.7}$$

The ideal gas law is used to close the system of equations. Writing the Euler equations (3.5) in tensorial form we have

$$\frac{\partial \mathbf{Q}}{\partial t} + \nabla \cdot \mathbf{F}_Q = 0 \tag{3.8}$$

where $\mathbf{F}_Q = \mathbf{F}\hat{\mathbf{e}}_x + \mathbf{G}\hat{\mathbf{e}}_y + \mathbf{H}\hat{\mathbf{e}}_z$.

3.3 Numerical Method

Equation (3.8) is discretized using the finite volume method (FVM) in conjunction with the second-order Roe-MUSCL scheme. Integrating (3.8) over a grid cell of volume V, and applying the Gauss divergence theorem yields

$$\frac{d}{dt}\int_V \mathbf{Q}(\mathbf{x}, t)\, dV + \int_A \mathbf{F}_Q \cdot \mathbf{n}\; dA = 0 \tag{3.9}$$

Applying the mid-point numerical integration results in a semi-discretized equation of the form

$$\frac{d\mathbf{Q}(t)}{dt} V + \sum_{f \in \text{cell faces}} (\mathbf{F}_Q \cdot \mathbf{n})_f \; A_f = 0 \tag{3.10}$$

where the face-normal flux is given by

$$\begin{aligned} (\mathbf{F}_Q \cdot \mathbf{n})_f &= (\mathbf{F}\hat{\mathbf{e}}_x + \mathbf{G}\hat{\mathbf{e}}_y + \mathbf{H}\hat{\mathbf{e}}_z)_f \cdot (n_x\hat{\mathbf{e}}_x + n_y\hat{\mathbf{e}}_y + n_z\hat{\mathbf{e}}_z)_f & (3.11) \\ &= (\mathbf{F}n_x + \mathbf{G}n_y + \mathbf{H}n_z)_f & (3.12) \end{aligned}$$

Temporal discretization of the time derivative term in (3.10) for the inviscid test cases in this chapter and homogeneous isotropic turbulent flow simulations in Chapter 4 is performed using the following three-stage Runge-Kutta method proposed by Jameson et al. [15]

$$\begin{aligned} \mathbf{Q}^{(0)} &= \mathbf{Q}^n \\ \mathbf{Q}^{(1)} &= \mathbf{Q}^{(0)} - \frac{1}{3}\frac{\Delta t}{V}\mathbf{R}^{(0)} \\ \mathbf{Q}^{(2)} &= \mathbf{Q}^{(0)} - \frac{1}{2}\frac{\Delta t}{V}\mathbf{R}^{(1)} \\ \mathbf{Q}^{(3)} &= \mathbf{Q}^{(0)} - \frac{\Delta t}{V}\mathbf{R}^{(2)} \\ \mathbf{Q}^{(n+1)} &= \mathbf{Q}^{(3)} \end{aligned} \tag{3.13}$$

where $\mathbf{R}^{(.)}$ is the residual equal to the second term in (3.10) and the superscript n denotes the time level.

3.4 Riemann's Initial Value Problem

The concept of Riemann's initial value problem (IVP) has been successfully incorporated into the finite volume framework to accurately capture discontinuites in the flow field. They preserve both the mathematical as well as the physical character of the governing equations. Prior to considering a generalized Riemann problem in the solution to three-dimensional Euler equations, its role in numerically solving the 1-D system of Euler equations of the form (3.1) will be discussed in this section. The Riemann's IVP is obtained when the initial data (3.2) is specialised to

$$\mathbf{Q}(x,0) = \mathbf{Q}_L \forall\ x < 0;\ \mathbf{Q}(x,0) = \mathbf{Q}_R \forall\ x > 0 \tag{3.14}$$

where $\mathbf{Q}_L$ and $\mathbf{Q}_R$ are uniform states to the left and right sides of a discontinuity located at $x = 0$. The Riemann problem is the simplest, non-trival IVP that can be considered [7]. Moreover, the solution is self-similar or self-preserving [6] in that it depends solely on one independent variable (x/t or $t/\sqrt{x}$). Consequently, it is a straight line on the $x - t$ diagram.

The Riemann problem is a generalization of the famous shock-tube problem. Here, the tube is initially divided into two equal compartments by a diaphragm. The two compartments contain the same gas at rest but at different thermodynamic states. The upstream state L is characterized by the pressure p_L and density ρ_L, and the downstream state R by p_R and ρ_R, with $p_L > p_R$. The rupture of the diaphragm generates a wave system consisting of an expansion fan, a contact discontinuity and

a shock wave as shown in Figure 3.1. There exists exact analytical solutions for each of the waves. However, obtaining these solutions require solving the following non-linear implicit equation using a computationally expensive iterative technique for the pressure ratio (p_2/p_1) across the shock wave:

$$\frac{p_4}{p_1} = \frac{p_2}{p_1}\left\{1 + \frac{\gamma-1}{2a_4}\left[u_4 - u_1 - \frac{a_1}{\gamma}\frac{\frac{p_2}{p_1}-1}{\sqrt{\frac{\gamma+1}{2\gamma}}}\left(\frac{p_2}{p_1}-1\right)+1\right]\right\} \tag{3.15}$$

The above expression is obtained by combining the shock, contact and expansion fan equations. See Laney [6] for details. Once p_2 is determined, it is then relatively straightforward to compute the rest of the unknown quantities in between the two acoustic (non-linear) waves, commonly referred to as the Star Region which is divided into two sub-regions by the contact discontinuity. Across this linearly degenerate entropy wave, the density of the fluid changes whereas pressure and velocity remain constant. In the general case of non-zero initial velocities, there are four possible wave patterns in the solution to the Riemann problem, as shown in Figure 3.2. The left and right waves are either shock or expansion waves, while the contact discontinuity always lies in the middle.

Godunov [34] in 1959 developed the first successful algorithm to utilize the concept of Riemann problem in the numerical solution to the Euler equations. He suggested replacing the initial data by piecewise constant set of states resulting in local Riemann problems at all internal (non-boundary) faces. The interface state was computed by treating the local Riemann problem as being analogous to the one-dimensional (1-D) shock tube problem. This enabled Godunov to compute the

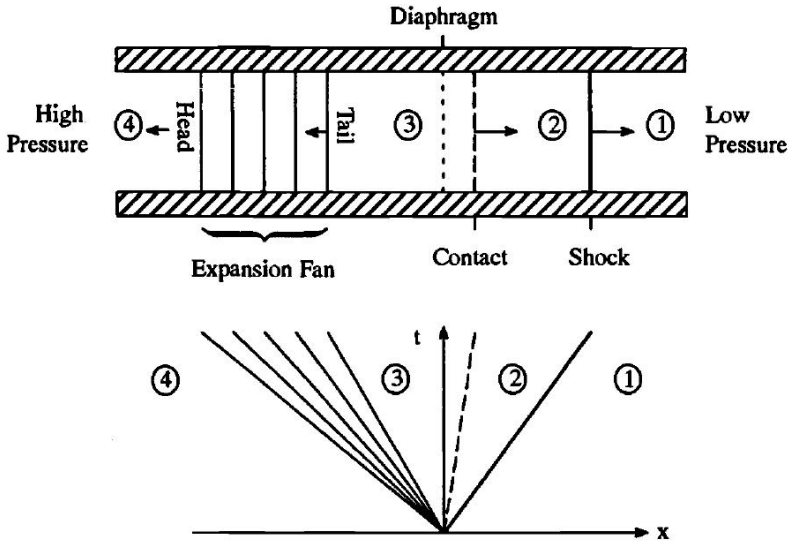

Figure 3.1: The Shock-tube problem and corresponding wave diagram with characteristics on the $x - t$ plane [6]

interface fluxes exactly since the analytical solution to the shock-tube problem can be obtained by solving the 1-D Euler equations. This is why Godunov's approach is commonly referred to as the "exact" Riemann Solver. In general, Godunov's scheme and those based on it are considered first-order upwind methods that reduce to the first-order upwind scheme for the linear advection equation. (see equation (2.19) in Chapter 2). Upwind schemes are very popular with the aerospace community since they produce highly accurate shock structures in transonic flow simulations [65, 66].

To preserve the self-similar nature of the solutions originating at each interface, left- and right-running waves from adjacent interfaces must be prevented from interacting with one another within a time interval Δt; as shown in Figure 3.3. The time step for preserving self-similarity can be computed as follows

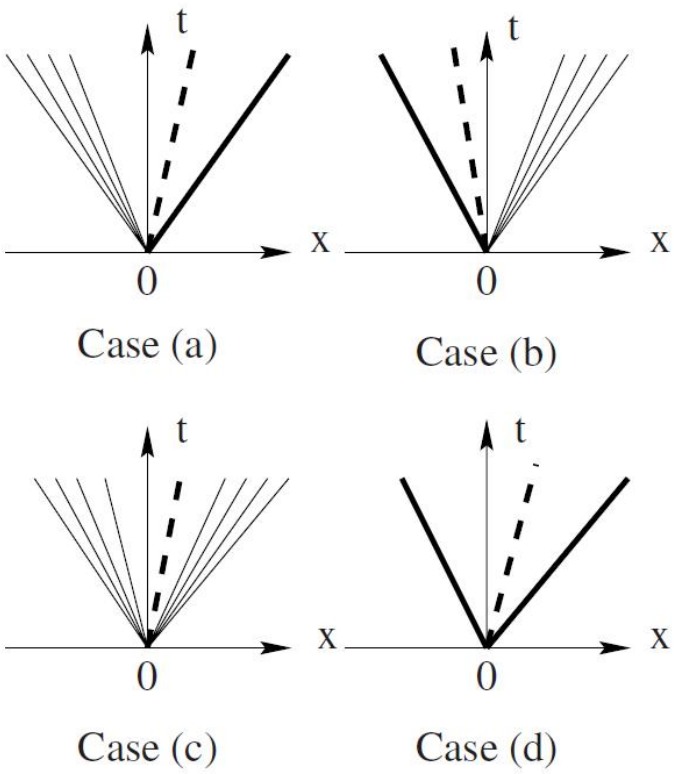

Figure 3.2: Four possible wave patterns (a - d) in the solution of the Riemann problem [7]. The expansion fan (rarefaction) and shock are represented by collection of four characteristic lines and a bold characteristic line, respectively. The middle wave indicated by the bold dashed line in all four figures is the contact discontinuity.

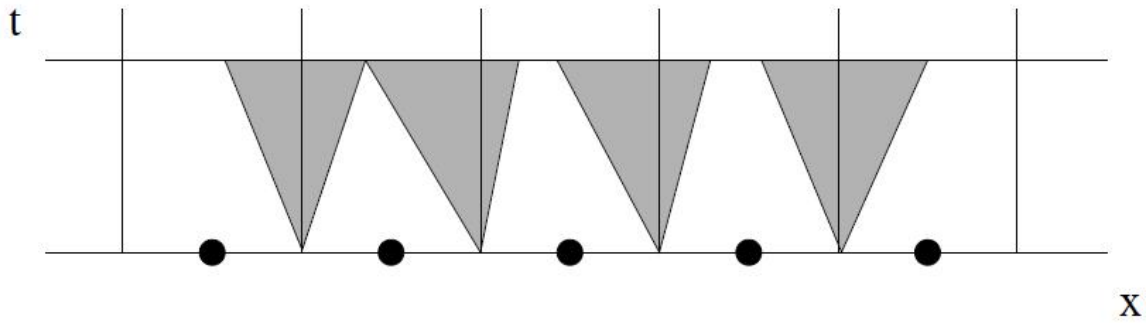

Figure 3.3: $x-t$ plot showing solutions to local Riemann problems at each interface in the domain. To preserve self-similarity, waves from adjacent interfaces must not overlap [8].

$$\Delta t \leq min(\Delta t_i) \tag{3.16}$$

where

$$\Delta t_i = \frac{x_{i+1/2} - x_{i-1/2}}{max(\lambda_{i-1/2,k^+}) - min(\lambda_{i+1/2,k^-})} \tag{3.17}$$

where $\lambda_{i-1/2,k^+}$ and $\lambda_{i+1/2,k^-}$ are the maximum positive and negative eigenvalues at $i-1/2$ and $i+1/2$ interfaces of cell i, respectively [8].

Since the data within a cell is treated as piecewise constant, Godunov's method is only first-order accurate in spite of computing the interface fluxes exactly. The principal advantages of Godunov's method for solving the 1-D Euler equations are that it is conservative and satisfies the entropy condition. In spite of these advantages, it is computationally expensive and inefficient since one has to solve the local Riemann problems through an iterative procedure. Consequently, researchers have developed a number of so-called "approximate" Riemann solvers that are computationally efficient than Godunov's exact solver.

3.5 Approximate Riemann Solvers

The computational resources necessary to solve the local Riemann problems exactly throughout the domain are significantly more than what is required to execute other parts of the numerical algorithm. This led to the development of less expensive, approximate Riemann solvers that produce equally accurate results at a fraction of the cost. Hence, most Riemann solvers in use today are of the approximate type. There are essentially two main classes of such solvers, namely the *Flux Vector Splitting*

methods (FVS) and *Flux Difference Splitting methods* (FDS). The former is well suited in the computation of steady aerodynamic flows. However, they are less accurate than FDS methods near stationary contacts and shear waves [7]. In the case of Navier-Stokes equations, the accuracy of FVS has been shown to be considerably less than FDS. Nevertheless, the methods are relatively simpler and more efficient since they involve vectors rather than matrices making them very popular within the CFD community. A scheme that combines the best of both techniques is the Advection Upwind Split Method (AUSM) [67], developed at NASA Lewis by Meng-Sing Liou and Chris Steffen. It is now a popular way of evaluating the numerical flux function. Following is a brief description of FVS and FDS.

The non-linear flux vector $\mathbf{F}(\mathbf{Q})$ in FVS is split into two parts:

$$\mathbf{F}(\mathbf{Q}) = \mathbf{F}^{+}(\mathbf{Q}) + \mathbf{F}^{-}(\mathbf{Q}) \tag{3.18}$$

where $\mathbf{F}^{+}(\mathbf{Q})$ and $\mathbf{F}^{-}(\mathbf{Q})$ account for positive and negative real eigenvalues, respectively. An alternative formulation to the above splitting is obtained by considering the following homogeneity property of the Euler equations [7]

$$\mathbf{F}(\mathbf{Q}) = \mathbf{A}(\mathbf{Q})\mathbf{Q} \tag{3.19}$$

where the jacobian $\mathbf{A} = \mathbf{L\Lambda R}$ can be analogously decomposed into positive and negative parts resulting in the following expressions

$$\mathbf{F}^{+} = \mathbf{A}^{+}\mathbf{Q} = \mathbf{L\Lambda}^{+}\mathbf{R} \tag{3.20}$$

$$\mathbf{F}^{-} = \mathbf{A}^{-}\mathbf{Q} = \mathbf{L\Lambda}^{-}\mathbf{R} \tag{3.21}$$

Two well known FVS methods are those of Steger-Warming [68] and van Leer [69]. The fluxes in the former are evaluated by considering the positive and negative wave speeds as

$$\lambda_i^{+} = max(0, \lambda_i) = \frac{1}{2}(\lambda_i + |\lambda_i|), \tag{3.22}$$

$$\lambda_i^{-} = min(0, \lambda_i) = \frac{1}{2}(\lambda_i - |\lambda_i|) \tag{3.23}$$

whereas in the van Leer's algorithm, the fluxes are written in terms of the Mach number (M) whose positive and negative components are split into two quadratic functions. However, their sum must satisfy the property, $M^{+} + M^{-} = M$. See Laney [6] for more details.

The most popular approximate Riemann solver is the FDS algorithm of Roe [40]. The method has been improved over the years by several authors and has been successfully applied to a large number of practical problems. Specific examples include solving the Magneto-Hydrodynamic equations (MHD) [70], reactive multi-phase problems [71] as well as the simulation of 2-D detonation waves in solid materials [72], among others. The principal idea of Roe's approach [40] is to approximate locally

the exact non-linear flux jacobian by a linearized matrix obtained using the Roe's averaged state variables. Similar to Godunov's solver, Roe's scheme also considers piecewise constant approximation of data within each cell. Following is a brief description of the scheme. Applying the chain rule to the flux derivative in (3.1) gives

$$\mathbf{Q}_t + \mathbf{A}\left(\mathbf{Q}\right)\mathbf{Q}_x = 0 \tag{3.24}$$

Roe replaced the exact jacobian $\mathbf{A}(\mathbf{Q})$ with an approximate matrix $\tilde{\mathbf{A}}\left(\mathbf{Q}_L, \mathbf{Q}_R\right)$ that depends on the local flow conditions

$$\mathbf{Q}_t + \tilde{\mathbf{A}}\left(\mathbf{Q}_L, \mathbf{Q}_R\right)\mathbf{Q}_x = 0 \tag{3.25}$$

$\tilde{\mathbf{A}}$ is chosen carefully so it satisfies the following list of properties:

1. Preserve the hyperbolicity of the system: Eigenvalues must be real and the eigenvectors need to be linearly independent
2. Consistency: $\tilde{\mathbf{A}}(\mathbf{Q}_L, \mathbf{Q}_R) \rightarrow \mathbf{A}(\mathbf{Q})$, as $(\mathbf{Q}_L, \mathbf{Q}_R) \rightarrow \mathbf{Q}$
3. Conservation across discontinuities (secant plane condition): $\mathbf{F}_R - \mathbf{F}_L = \tilde{\mathbf{A}}(\mathbf{Q}_L, \mathbf{Q}_R) \times (\mathbf{Q}_R - \mathbf{Q}_L)$

Together, the three properties are referred to as "Property U" since they are meant to ensure *uniform* validity across discontinuities. The third is a necessary condition to recognize a discontinuity in the flow field. To determine the eigenvalues and eigenvectors of $\tilde{\mathbf{A}}(\mathbf{Q}_L, \mathbf{Q}_R)$ that is capable of satisfying "Property U", Roe expressed all

variables in terms of components of the following parameter vector

$$\mathbf{w} = \rho^{1/2}(1, u, v, w, H)^T \tag{3.26}$$

Consequently, the jumps in the conserved variables $\Delta\mathbf{Q}$ and fluxes $\Delta\mathbf{F}$ can be written in terms of jump $\Delta\mathbf{w}$ by two matrices $\tilde{\mathbf{B}}$ and $\tilde{\mathbf{C}}$, respectively, as follows

$$\Delta\mathbf{Q} = \tilde{\mathbf{B}}\Delta\mathbf{w} \tag{3.27}$$

$$\Delta\mathbf{F} = \tilde{\mathbf{C}}\Delta\mathbf{w} \tag{3.28}$$

Hence, the matrix that maps $\Delta\mathbf{Q}$ onto $\Delta\mathbf{F}$ is $\tilde{\mathbf{A}} = \mathbf{C}\mathbf{B}^{-1}$.

In general, both the exact and approximate Riemann solvers can be expressed by the following numerical flux function [61]

$$\mathbf{F} = \frac{1}{2}\left[\mathbf{F}(\mathbf{Q}_L) + \mathbf{F}(\mathbf{Q}_R)\right] - \frac{1}{2}\mathbf{D}(\mathbf{Q}_L, \mathbf{Q}_R)(\mathbf{Q}_R - \mathbf{Q}_L) \tag{3.29}$$

where $\mathbf{D}$ is the viscosity [73] or dissipation matrix [61], which in the case of Godunov and Roe solvers are the jacobians $\mathbf{A}(\mathbf{Q})$ and $\tilde{\mathbf{A}}(\mathbf{Q}_L, \mathbf{Q}_R)$, respectively. The simplest and highly robust solver is that of Lax-Friedrichs (LF). The viscosity matrix for this scheme $\mathbf{D}^{LF} = \frac{\Delta x}{\Delta t}\mathbf{I}$, making it one of the most dissipative schemes. A scheme that was a workhorse of numerous aerodynamic codes in the 1960s and 70s is the famous Lax-Wendroff (LW) method. It is a stable, non-monotonic (linear) scheme that is second-order accurate in both space and time, and is derived by replacing the time

derivatives in the Taylor series with space derivatives. The dissipation matrix of LW scheme is

$$\mathbf{D}^{LW}(\mathbf{Q}_L, \mathbf{Q}_R) = \frac{\Delta t}{\Delta x}\mathbf{A}^2 \tag{3.30}$$

Roe's method falls under the category of FDS technique since the difference in the flux can be split into positive and negative parts

$$\mathbf{F}_R - \mathbf{F}_L = (\tilde{\mathbf{A}}_f^+ + \tilde{\mathbf{A}}_f^-)(\mathbf{Q}_R - \mathbf{Q}_L) \tag{3.31}$$

where f is the interface. Both FVS and FDS methods can be expressed as follows

$$\mathbf{F}_f = \frac{1}{2}\left[\mathbf{F}(\mathbf{Q}_L) + \mathbf{F}(\mathbf{Q}_R)\right] - \frac{1}{2}(\tilde{\mathbf{A}}_f^+ - \tilde{\mathbf{A}}_f^-)(\mathbf{Q}_R - \mathbf{Q}_L) \tag{3.32}$$

The difference lies in the manner in which the matrices $\tilde{\mathbf{A}}^{\pm}$ are defined. In the case of FDS, they are defined by (3.31), whereas in the case of FVS, they are defined as

$$\mathbf{F}^+(\mathbf{Q}_R) - \mathbf{F}^+(\mathbf{Q}_L) = \tilde{\mathbf{A}}_f^+(\mathbf{Q}_R - \mathbf{Q}_L) \tag{3.33}$$

$$\mathbf{F}^-(\mathbf{Q}_R) - \mathbf{F}^-(\mathbf{Q}_L) = \tilde{\mathbf{A}}_f^-(\mathbf{Q}_R - \mathbf{Q}_L) \tag{3.34}$$

It is interesting to note that solutions obtained using FVS technique are also solutions to FDS methods but the reverse is not true. Hence, all first-order upwind FVS methods can be considered as a subset of first-order upwind FDS methods.

3.6 Multidimensional Riemann Solvers

Godunov-based Riemann solvers such as Roe's were developed primarily to solve the x-split Euler equations. For multidimensional problems, the non-existence of a generalized Riemann problem can produce erroneous results [40] with multi-dimensional extension of classical Riemann solvers. On cartesian grids, there exists two main approaches to solving the system of hyperbolic conservation laws in multi-dimensions. The first method is termed *dimensional or method of fractal steps* and the second is the *finite volume method*.

In the dimensional splitting method [74, 75], the 1-D schemes are applied sequentially in all three coordinate directions in a manner similar to the predictor-corrector methods. This has been the traditional method of extending upwind differencing schemes to multidimensions [76]. The solution to the system of PDE in one direction is taken as the initial condition to the next chosen direction. For all three directions, the time step Δt is taken to be the same.

$$\mathbf{U}^{n+1} = z^{(\Delta t)} y^{(\Delta t)} x^{(\Delta t)} (\mathbf{U}^n) \tag{3.35}$$

where x, y and z signify the direction in which operations are being performed on the system. However, the final solution is independent of the order of operations.

The second approach for extending 1-D Riemann solvers to higher dimensions is termed *unsplit* finite volume method. Unlike the dimensional splitting method, the

solution here is advanced in a single step as follows

$$\mathbf{Q}_{i,j,k}^{n+1} = \mathbf{Q}_{i,j,k}^{n} + \frac{\Delta t}{\Delta x}\left[\mathbf{F}_{i-\frac{1}{2},j,k} - \mathbf{F}_{i+\frac{1}{2},j,k}\right] + \left[\mathbf{G}_{i,j-\frac{1}{2},k} - \mathbf{G}_{i,j+\frac{1}{2},k}\right] + \left[\mathbf{H}_{i,j,k-\frac{1}{2}} - \mathbf{H}_{i,j,k+\frac{1}{2}}\right] \tag{3.36}$$

where the numerical fluxes $\mathbf{F}$, $\mathbf{G}$ and $\mathbf{H}$ are determined by solving local Riemann problems in each direction.

The 1-D finite volume schemes extended to multidimensions using either of the above two techniques has been shown to be highly accurate in smooth regions of the flow. However, discontinuities oblique to the grid are badly resolved. Schemes that are highly diffusive can mask this deficiency in higher dimensions but this does not increase the accuracy of the solution. To resolve this problem, Rotated Riemann solvers were developed in the early 1980s. The solvers are activated in a rotated frame whereby the angle of rotation is determined by the local flow gradient across a discontinuity. The frame is rotated by this angle so that it aligns with the shock normal vector. This idea was first proposed by Davis [77] and has been subsequently improved and refined by several authors. A notable drawback of this technique is that higher-order Riemann solvers become less robust. To resolve these problems, "true" multidimensional solvers are being actively pursued. The issue of multidimensional extension of Roe's scheme for unstructured grids are addressed next.

3.6.1 Frink's Approach

Both dimensional splitting and finite volume methods were developed specifically for structured grids. In the case of flow around complex geometries where

unstructured meshed are common, such techniques cannot be applied due to lack of directional information. To address this issue, Frink [78] developed a formulation to successfully extend Roe's scheme to multidimensional unstructured grids. At any arbitrary interface, Roe's flux-difference splitting technique was expressed as follows

$$\mathbf{F}_k = \frac{1}{2}\left[\mathbf{F}(\mathbf{Q}_L) + \mathbf{F}(\mathbf{Q}_R)\right] - \frac{1}{2}|\tilde{\mathbf{A}}_k|\left(\mathbf{Q}_R - \mathbf{Q}_L\right) \tag{3.37}$$

where $\tilde{\mathbf{A}}_k$ is Roe's jacobian normal to an interface k. The product of the jacobian and jump in the vector of conserved variables $(\mathbf{Q}_R - \mathbf{Q}_L)$ was replaced by a sum of three flux vectors for each of the three waves propagating normal to the interface k. These are presented below

$$|\tilde{\mathbf{A}}_k|\left(\mathbf{Q}_R - \mathbf{Q}_L\right) = |\Delta\tilde{\mathbf{F}}_1| + |\Delta\tilde{\mathbf{F}}_4| + |\Delta\tilde{\mathbf{F}}_5| \tag{3.38}$$

$$|\Delta\tilde{\mathbf{F}}_1| = |\tilde{U}|\left\{\left(\Delta\rho - \frac{\Delta p}{\tilde{a}^2}\right)\begin{bmatrix} 1 \\ \tilde{u} \\ \tilde{v} \\ \tilde{w} \\ \frac{\tilde{u}^2+\tilde{v}^2+\tilde{w}^2}{2} \end{bmatrix} + \tilde{\rho}\begin{bmatrix} 0 \\ \Delta u - \hat{n}_x\Delta U \\ \Delta v - \hat{n}_y\Delta U \\ \Delta w - \hat{n}_z\Delta U \\ \tilde{u}\Delta u + \tilde{v}\Delta v + \tilde{w}\Delta w - \tilde{U}\Delta U \end{bmatrix}\right\} \tag{3.39}$$

$$|\Delta\tilde{\mathbf{F}}_{4,5}| = |\tilde{U} \pm \tilde{a}| \left\{ \left(\frac{\Delta p \pm \tilde{\rho}\tilde{a}\Delta U}{2\tilde{a}^2} \right) \begin{bmatrix} 1 \\ \tilde{u} \pm \hat{n}_x \tilde{a} \\ \tilde{v} \pm \hat{n}_y \tilde{a} \\ \tilde{w} \pm \hat{n}_z \tilde{a} \\ \tilde{h}_o \pm \tilde{U}\tilde{a} \end{bmatrix} \right\} \tag{3.40}$$

where $\tilde{U} = \tilde{u}\hat{n}_x + \tilde{v}\hat{n}_y + \tilde{w}\hat{n}_z$ and $\Delta U = \Delta u\hat{n}_x + \Delta v\hat{n}_y + \Delta w\hat{n}_z$. Higher-order reconstruction was achieved through van Leer's MUSCL extrapolation algorithm. Results were presented for transonic flow around around ONERA M6 wing to demonstrate the speed, accuracy and robustness of the solver. The method seemingly avoids oscillations in the vicinity of the shocks without limiters. However, the author's Ph.D. thesis [79] states that limiting may be necessary to avoid oscillations in 2-D.

3.6.2 Current Formulation

The current study also employs Roe's flux-difference splitting technique to discretize the convective fluxes in (3.12). Here, an alternative extension of Roe's fluxes to 3-D problems on unstructured meshes is presented. In a 3-D scenario on a generalized mesh, the Riemann problem normal to the cell interface (see Figure 2.1) can be decomposed into three 1-D Riemann problems, one each along x, y, and z

directions. Accordingly, the three components of flux vector can be written as:

$$\mathbf{F} = \frac{1}{2}\left[\mathbf{F}(\mathbf{Q}_L) + \mathbf{F}(\mathbf{Q}_R)\right] - \frac{1}{2}|\tilde{\mathbf{A}}_F|(\mathbf{Q}_R - \mathbf{Q}_L) \tag{3.41}$$

$$\mathbf{G} = \frac{1}{2}\left[\mathbf{G}(\mathbf{Q}_L) + \mathbf{G}(\mathbf{Q}_R)\right] - \frac{1}{2}|\tilde{\mathbf{A}}_G|(\mathbf{Q}_R - \mathbf{Q}_L) \tag{3.42}$$

$$\mathbf{H} = \frac{1}{2}\left[\mathbf{H}(\mathbf{Q}_L) + \mathbf{H}(\mathbf{Q}_R)\right] - \frac{1}{2}|\tilde{\mathbf{A}}_H|(\mathbf{Q}_R - \mathbf{Q}_L) \tag{3.43}$$

where $\tilde{\mathbf{A}}_{F,G,H}$ are the Roe-averaged constant Jacobians in each of the three directions. The first term on the RHS of each of the equations (3.41), (3.42) and (3.43) represents the central-differenced flux, whereas the second term known as dissipative flux provides the necessary artifical viscosity to ensure stability and monotonicity. Substituting (3.41), (3.42) and (3.43) into (3.12) we have,

$$(\mathbf{F}_Q \cdot \mathbf{n})_f = \mathbf{F}_{\text{CDS}} - \frac{1}{2}|\tilde{\mathbf{A}}_n|(\mathbf{Q}_R - \mathbf{Q}_L) \tag{3.44}$$

where

$$\begin{aligned}\mathbf{F}_{\text{CDS}} = {} & \frac{1}{2}\left[\mathbf{F}(\mathbf{Q}_L) + \mathbf{F}(\mathbf{Q}_R)\right] n_x + \frac{1}{2}\left[(\mathbf{G}(\mathbf{Q}_L) + \mathbf{G}(\mathbf{Q}_R)\right] n_y + \\ & \frac{1}{2}\left[\mathbf{H}(\mathbf{Q}_L) + \mathbf{H}(\mathbf{Q}_R)\right] n_z\end{aligned} \tag{3.45}$$

and

$$
\begin{aligned}
|\tilde{\mathbf{A}}_n| &= |\tilde{\mathbf{A}}_F|\ n_x + |\tilde{\mathbf{A}}_G|\ n_y + |\tilde{\mathbf{A}}_H|\ n_z && (3.46)\\
&= (\tilde{\mathbf{R}}_F\ |\tilde{\mathbf{\Lambda}}_F|\ \tilde{\mathbf{L}}_F)\ n_x + (\tilde{\mathbf{R}}_G\ |\tilde{\mathbf{\Lambda}}_G|\ \tilde{\mathbf{L}}_G)\ n_y + (\tilde{\mathbf{R}}_H\ |\tilde{\mathbf{\Lambda}}_H|\ \tilde{\mathbf{L}}_H)\ n_z && (3.47)\\
&= \sum_{(\theta,\alpha)} (\tilde{\mathbf{R}}_\theta\ |\tilde{\mathbf{\Lambda}}_\theta|\ \tilde{\mathbf{L}}_\theta)\ n_\alpha, \quad (\theta,\alpha) = (F,x),(G,y),(H,z) && (3.48)
\end{aligned}
$$

Here $\tilde{\mathbf{R}}_\theta$ and $\tilde{\mathbf{L}}_\theta$ are the right and left eigenvector matrices along α-direction, and $|\tilde{\mathbf{\Lambda}}_\theta|$ is the corresponding eigenvalue matrix. While Roe [40] derived the forms of $\tilde{\mathbf{R}}_F$ and $|\tilde{\mathbf{\Lambda}}_F|$ only, the current study presents $\tilde{\mathbf{R}}_\theta$ and $|\tilde{\mathbf{\Lambda}}_\theta|$ corresponding to $\theta = G,\ H$ as well. The $\tilde{\mathbf{R}}_\theta$ and $|\tilde{\mathbf{\Lambda}}_\theta|$ matrices for all three components are shown below.

$$
\tilde{\mathbf{R}}_F = \begin{bmatrix}
1 & 1 & 0 & 0 & 1 \\
\tilde{u}-\tilde{a} & \tilde{u} & 0 & 0 & \tilde{u}+\tilde{a} \\
\tilde{v} & \tilde{v} & 1 & 0 & \tilde{v} \\
\tilde{w} & \tilde{w} & 0 & 1 & \tilde{w} \\
\tilde{H}-\tilde{u}\tilde{a} & \frac{1}{2}(\tilde{u}^2+\tilde{v}^2+\tilde{w}^2) & \tilde{v} & \tilde{w} & \tilde{H}+\tilde{u}\tilde{a}
\end{bmatrix} \qquad (3.49)
$$

$$\tilde{\mathbf{R}}_G = \begin{bmatrix} 1 & 0 & 1 & 0 & 1 \\ \tilde{u} & 1 & \tilde{u} & 0 & \tilde{u} \\ \tilde{v} - \tilde{a} & 0 & \tilde{v} & 0 & \tilde{v} + \tilde{a} \\ \tilde{w} & 0 & \tilde{w} & 1 & \tilde{w} \\ \tilde{H} - \tilde{v}\tilde{a} & \tilde{u} & \frac{1}{2}(\tilde{u}^2 + \tilde{v}^2 + \tilde{w}^2) & \tilde{w} & \tilde{H} + \tilde{v}\tilde{a} \end{bmatrix} \tag{3.50}$$

$$\tilde{\mathbf{R}}_H = \begin{bmatrix} 1 & 0 & 0 & 1 & 1 \\ \tilde{u} & 1 & 0 & \tilde{u} & \tilde{u} \\ \tilde{v} & 0 & 1 & \tilde{v} & \tilde{v} \\ \tilde{w} - \tilde{a} & 0 & 0 & \tilde{w} & \tilde{w} + \tilde{a} \\ \tilde{H} - \tilde{w}\tilde{a} & \tilde{u} & \tilde{v} & \frac{1}{2}(\tilde{u}^2 + \tilde{v}^2 + \tilde{w}^2) & \tilde{H} + \tilde{w}\tilde{a} \end{bmatrix} \tag{3.51}$$

$$|\tilde{\mathbf{\Lambda}}_F| = \begin{bmatrix} |\tilde{u} - \tilde{a}| & 0 & 0 & 0 & 0 \\ 0 & |\tilde{u}| & 0 & 0 & 0 \\ 0 & 0 & |\tilde{u}| & 0 & 0 \\ 0 & 0 & 0 & |\tilde{u}| & 0 \\ 0 & 0 & 0 & 0 & |\tilde{u} + \tilde{a}| \end{bmatrix} \tag{3.52}$$

$$|\tilde{\mathbf{\Lambda}}_G| = \begin{bmatrix} |\tilde{v}-\tilde{a}| & 0 & 0 & 0 & 0 \\ 0 & |\tilde{v}| & 0 & 0 & 0 \\ 0 & 0 & |\tilde{v}| & 0 & 0 \\ 0 & 0 & 0 & |\tilde{v}| & 0 \\ 0 & 0 & 0 & 0 & |\tilde{v}+\tilde{a}| \end{bmatrix} \tag{3.53}$$

$$|\tilde{\mathbf{\Lambda}}_H| = \begin{bmatrix} |\tilde{w}-\tilde{a}| & 0 & 0 & 0 & 0 \\ 0 & |\tilde{w}| & 0 & 0 & 0 \\ 0 & 0 & |\tilde{w}| & 0 & 0 \\ 0 & 0 & 0 & |\tilde{w}| & 0 \\ 0 & 0 & 0 & 0 & |\tilde{w}+\tilde{a}| \end{bmatrix} \tag{3.54}$$

Roe's averaged variables in (3.49)-(3.54) are given by:

$$\tilde{\mathbf{u}} = \frac{\sqrt{\rho_L}\mathbf{u}_L + \sqrt{\rho_R}\mathbf{u}_R}{\sqrt{\rho_L} + \sqrt{\rho_R}} \tag{3.55}$$

$$\tilde{H} = \frac{\sqrt{\rho_L}H_L + \sqrt{\rho_R}H_R}{\sqrt{\rho_L} + \sqrt{\rho_R}} \tag{3.56}$$

$$\tilde{a} = \sqrt{(\gamma-1)\left[\tilde{H} - \frac{1}{2}(\tilde{u}^2+\tilde{v}^2+\tilde{w}^2)\right]} \tag{3.57}$$

Here, $\tilde{\mathbf{u}} = (\tilde{u}, \tilde{v}, \tilde{w})^{\mathrm{T}}$, $H = e_t + \frac{p}{\rho}$ is the total enthalpy, a is the sound speed, and subscripts L and R represent the left and right states at a cell interface.

The eigenvalues $|\tilde{\lambda}_F|_2$, $|\tilde{\lambda}_G|_3$ and $|\tilde{\lambda}_H|_4$ in (3.52), (3.53) and (3.54), respectively—i.e., $|\tilde{u}|$, $|\tilde{v}|$ and $|\tilde{w}|$—correspond to the propagation speeds of linear contact (entropy waves) along the three directions. The eigenvalues $|\tilde{\lambda}_F|_{\{3,4\}}$, $|\tilde{\lambda}_G|_{\{2,4\}}$ and $|\tilde{\lambda}_H|_{\{2,3\}}$ are

the propagation speeds of shear waves across which the two corresponding tangential velocity components—(v,w), (u,w), and (u,v)—change discontinuously [7]. Finally, the eigenvalues $|\tilde{\lambda}_\theta|_{\{1,5\}}$, $\theta = (F, G, H)$, are the left- and right-propagating acoustic waves along the three coordinate axes. It will be seen subsequently that the acoustic waves contribute the most to the dissipation of turbulent kinetic energy in the simulation of turbulent flows. It is interesting to note that on unstructured meshes, there are in general 15 waves originating at every interface in the domain, while on cartesian grids there are only 5 waves.

3.6.3 Second Order Extension and Scalar ν_{num} Formulation

In this section, an expression for the numerical viscosity of the Roe-MUSCL scheme is derived for the Euler equations. The current approach involves the extension of the viscosity formulation for the scalar advection equation to the 3-D Euler equations under consideration. Rieper [73] also developed an expression for the numerical viscosity inherent to the original Roe's upwind scheme for the 2-D x-split Euler equations (with two velocity components, but fluxes only along the x-direction). There are, however, important differences between the approach in the current study and that in Rieper [73]. First, we consider the full 3-D form of the Euler equations that are discretized using the second-order Roe-MUSCL scheme, whereas Rieper considered 2-D x-split Euler equations in conjunction with the first-order Roe's scheme. Second, the current formulation is derived for generalized 3-D unstructured meshes, while that of Rieper is applicable to 1-D uniform meshes only. Third, this study presents the spatial profiles and spectra of numerical viscosity, the former for shock-tube and

supersonic wedge flow cases, and the latter for isotropic turbulence. Rieper's study does not present this data, instead focusing on the behavior of Roe's scheme at low Mach numbers.

In van Leer's Monotone Upstream-Centered Scheme for Conservation Laws (MUSCL) approach [45], the contribution of cell-centered gradients to the variable reconstruction is limited using a function that is appropriately known as the limiter function. Using the MUSCL scheme, the left and right interface states, $\mathbf{Q}_L$ and $\mathbf{Q}_R$ respectively, of the conservation variables can be written as

$$\mathbf{Q}_L = \mathbf{Q}_{L,c} + \frac{\mathbf{\Psi}}{\Lambda} \nabla \mathbf{Q}_{L,c} \cdot \triangle \mathbf{r}_{Lf} \tag{3.58}$$

$$\mathbf{Q}_R = \mathbf{Q}_{R,c} + \frac{\mathbf{\Psi}}{\Lambda} \nabla \mathbf{Q}_{R,c} \cdot \triangle \mathbf{r}_{Rf} \tag{3.59}$$

where $\mathbf{Q}_{L,c}$ and $\mathbf{Q}_{R,c}$ are the left and right cell-centered states of the conservation variable vector $\mathbf{Q}$, $\nabla \mathbf{Q}_{L,c}$ and $\nabla \mathbf{Q}_{R,c}$ are the corresponding cell-centered gradients, $\triangle \mathbf{r}_{Lf}$ and $\triangle \mathbf{r}_{Rf}$ are the vectors from the face centroid to the left and right cell centers, respectively. The terms $\nabla \mathbf{Q}_{L,c} \cdot \triangle \mathbf{r}_{Lf}$ and $\nabla \mathbf{Q}_{R,c} \cdot \triangle \mathbf{r}_{Rf}$ in (3.58) and (3.59) should be interpreted as column vectors whose elements are the gradients of conserved variables dotted with $\triangle \mathbf{r}_{Lf}$ and $\triangle \mathbf{r}_{Rf}$. For example, the first element in the two column vectors are $\nabla \rho \cdot \triangle \mathbf{r}_{Lf}$ and $\nabla \rho \cdot \triangle \mathbf{r}_{Rf}$, respectively.

The flux limiter matrix $\mathbf{\Psi}$ is a diagonal matrix of limiters for each of the conserved variables, and is given by

$$\mathbf{\Psi} = \begin{bmatrix} \psi_\rho & 0 & 0 & 0 & 0 \\ 0 & \psi_{\rho u} & 0 & 0 & 0 \\ 0 & 0 & \psi_{\rho v} & 0 & 0 \\ 0 & 0 & 0 & \psi_{\rho v} & 0 \\ 0 & 0 & 0 & 0 & \psi_{\rho e_t} \end{bmatrix} \tag{3.60}$$

Inclusion of the scaling parameter Λ in (3.58) and (3.59) was motivated by Bidadi and Rani [80] (see Chapter 2), who showed that choosing $\Lambda = 2$ ensures solution monotonicity when the originally 1-D limiters are extended to multi-dimensional (2-D and 3-D) problems. However, $\Lambda = 2$ increases the artificial viscosity of the MUSCL scheme, and should rather be avoided in case of turbulent flows to prevent excessive dissipation of turbulent kinetic energy.

Substituting (3.58) and (3.59) into Roe's flux(5.8) gives

$$\begin{aligned} (\mathbf{F}_Q \cdot \mathbf{n})_f &= \mathbf{F}_{\text{CDS}} - \frac{1}{2} \left|\tilde{\mathbf{A}}_n\right| (\mathbf{Q}_{R,c} - \mathbf{Q}_{L,c}) - \\ &\quad \frac{\mathbf{\Psi}}{2\Lambda} \left|\tilde{\mathbf{A}}_n\right| (\nabla \mathbf{Q}_{L,c} \cdot \triangle \mathbf{r}_{Lf} - \nabla \mathbf{Q}_{R,c} \cdot \triangle \mathbf{r}_{Rf}) \qquad (3.61) \\ &= \mathbf{F}_{\text{Roe}} + \mathbf{F}_{\text{ADF}} \qquad (3.62) \end{aligned}$$

where

$$\mathbf{F}_{\text{Roe}} = \mathbf{F}_{\text{CDS}} - \frac{1}{2} \left|\tilde{\mathbf{A}}_n\right| \left(\mathbf{Q}_{R,c} - \mathbf{Q}_{L,c}\right) \tag{3.63}$$

$$\mathbf{F}_{\text{ADF}} = -\frac{\boldsymbol{\Psi}}{2\Lambda} \left|\tilde{\mathbf{A}}_n\right| \left(\nabla \mathbf{Q}_{L,c} \cdot \triangle \mathbf{r}_{Lf} - \nabla \mathbf{Q}_{R,c} \cdot \triangle \mathbf{r}_{Rf}\right) \tag{3.64}$$

Recognizing that $\nabla \mathbf{Q}_{L,c} \cdot \triangle \mathbf{r}_{Lf}$ and $\nabla \mathbf{Q}_{R,c} \cdot \triangle \mathbf{r}_{Rf}$ are the first-order terms in the Taylor-series expansions of $\mathbf{Q}_R$ and $\mathbf{Q}_L$ about the respective cell-centered quantities $\mathbf{Q}_{R,c}$ and $\mathbf{R}_{L,c}$, the anti-diffusive flux vector $\mathbf{F}_{\text{ADF}}$ becomes

$$\mathbf{F}_{\text{ADF}} = -\frac{\boldsymbol{\Psi}}{2\Lambda} \left|\tilde{\mathbf{A}}_n\right| \left[\left(\mathbf{Q}_R - \mathbf{Q}_L\right) - \left(\mathbf{Q}_{R,c} - \mathbf{R}_{L,c}\right)\right] \tag{3.65}$$

However, as shown in [80] and Appendix A, $[(\mathbf{Q}_i)_R - (\mathbf{Q}_i)_L] \ll [(\mathbf{Q}_i)_{R,c} - (\mathbf{Q}_i)_{L,c}]$, where $[(\mathbf{Q}_i)_R - (\mathbf{Q}_i)_L]$ is the difference at the interface between the reconstructed quantities of the i^{th} conserved variable in the $\mathbf{Q}$ vector, while $[(\mathbf{Q}_i)_{R,c} - (\mathbf{Q}_i)_{L,c}]$ represents the difference between the corresponding cell-centered quantities. The anti-diffusive flux $\mathbf{F}_{ADF}$ then becomes

$$\mathbf{F}_{\text{ADF}} \approx \frac{\boldsymbol{\Psi}}{2\Lambda} \left|\tilde{\mathbf{A}}_n\right| \left(\mathbf{Q}_{R,c} - \mathbf{R}_{L,c}\right) \tag{3.66}$$

Substituting (3.66) into (3.62) and using a face-centered Taylor series expansion for $(\mathbf{Q}_{R,c} - \mathbf{R}_{L,c})$ yields

$$
\begin{aligned}
(\mathbf{F}_Q \cdot \mathbf{n})_f &\approx \mathbf{F}_{\text{CDS}} - \frac{1}{2} \left|\tilde{\mathbf{A}}_n\right| (\mathbf{Q}_R - \mathbf{Q}_L) + \frac{\boldsymbol{\Psi}}{2\Lambda} \left|\tilde{\mathbf{A}}_n\right| (\mathbf{Q}_R - \mathbf{Q}_L) && (3.67)\\
&= \mathbf{F}_{\text{CDS}} - \frac{1}{2} \left(\mathbf{I} - \frac{\boldsymbol{\Psi}}{\Lambda}\right) \left|\tilde{\mathbf{A}}_n\right| (\mathbf{Q}_R - \mathbf{Q}_L) && (3.68)\\
&= \mathbf{F}_{\text{CDS}} - \frac{1}{2} \left(\mathbf{I} - \frac{\boldsymbol{\Psi}}{\Lambda}\right) \left|\tilde{\mathbf{A}}_n\right| (\mathbf{d} \cdot \mathbf{n})_f \, (\nabla \mathbf{Q} \cdot \mathbf{n})_f && (3.69)\\
&= \mathbf{F}_{\text{CDS}} - \mathbf{F}_{\text{Diss}} && (3.70)
\end{aligned}
$$

where $\mathbf{d}$ is the vector from the left to right cell centroid, and $\mathbf{F}_{\text{Diss}}$ is the net diffusive flux.

With the central differencing flux in (3.69) approximating the true flux function (3.12), and the artificial dissipation terms being analogous to the viscous terms in the Navier-Stokes equations, the modified Euler equations can now be expressed as

$$\frac{\partial \mathbf{Q}}{\partial t} + \nabla \cdot \mathbf{F}_Q - \nabla \cdot (\boldsymbol{\nu}_{\text{RM}} \nabla \mathbf{Q}) = 0 \tag{3.71}$$

The numerical viscosity matrix $\boldsymbol{\nu}_{\text{RM}}$ of the Roe-MUSCL scheme at a cell interface is given by

$$\boldsymbol{\nu}_{\text{RM}} = \frac{1}{2} \left(\mathbf{I} - \frac{\boldsymbol{\Psi}}{\Lambda}\right) \left|\tilde{\mathbf{A}}_n\right| (\mathbf{d} \cdot \mathbf{n})_f \tag{3.72}$$

where the subscript RM refers to the origins of $\boldsymbol{\nu}_{\text{RM}}$ in the Roe-MUSCL scheme.

3.6.4 Modification of Numerical Viscosity due to Harten's Entropy Fix

Linearized approximate Riemann solvers such as Roe's can accurately capture shocks and contact discontinuities [6, 7]. However, unlike Godunov's exact Riemann solver [34], Roe's scheme generates entropy-violating expansion shock instead of an expansion fan. That is, the expansion shock satisfies the Rankine-Hugoniot jump condition, but flow expansion across the wave violates the second law of thermodynamics. The eigenvalue associated with the expansion shock is $\lambda = \tilde{u} - \tilde{a}$. As the wave is traversed from left to right, the eigenvalue $\lambda = \tilde{u} - \tilde{a}$ changes from negative to positive. This means that there exits a point where the flow becomes sonic ($\tilde{u} = \tilde{a}$) [7]. In the case of entropy waves, sonic points occur for $M = 1$. From the condition that numerical viscosity is directly proportional to wave speed (see (3.80)), the dearth of numerical viscosity at or in the neighborhood of sonic points results in entropy-violating solutions. Harten's [81] correction of artificially increasing the viscosity in a quadratic manner for wave speeds falling below a threshold level ensures a smooth change in the flowfield variables. This correction is employed in the current study, and is presented below.

$$H(\lambda) = \begin{cases} \frac{\lambda+\delta}{2\delta}, & |\lambda| < \delta \\ |\lambda|, & |\lambda| \geq \delta \end{cases} \tag{3.73}$$

The Harten-corrected normal flux then becomes

$$(\mathbf{F}_Q \cdot \mathbf{n})_f = \mathbf{F}_{\text{CDS}} - \frac{1}{2}\left(\mathbf{I} - \frac{\mathbf{\Psi}}{\Lambda}\right)\left(\sum_\theta \tilde{\mathbf{R}}_\theta \, |H(\tilde{\mathbf{\Lambda}}_\theta)| \, \tilde{\mathbf{L}}_\theta\right)(\mathbf{Q}_R - \mathbf{Q}_L) \tag{3.74}$$

where $\theta = (F, G, H)$, $|H(\tilde{\mathbf{\Lambda}}_\theta)|$ refers to the Harten-factor-scaled eigenvalue matrices $|\tilde{\mathbf{\Lambda}}_F|$, $|\tilde{\mathbf{\Lambda}}_G|$ and $|\tilde{\mathbf{\Lambda}}_H|$ in (3.52), (3.53) and (3.54), respectively.

The numerical viscosity $\boldsymbol{\nu}_{\text{RMH}}$ of the Harten-corrected Roe-MUSCL scheme at a cell interface is given by

$$\boldsymbol{\nu}_{\text{RMH}} = \frac{1}{2}\left(\mathbf{I} - \frac{\mathbf{\Psi}}{\Lambda}\right)|H(\tilde{\mathbf{A}}_n)|\ (\mathbf{d}\cdot\mathbf{n})_f \tag{3.75}$$

where the subscript RMH refers to Harten-corrected Roe-MUSCL scheme.

3.6.5 Mitigation of numerical Viscosity in Roe-MUSCL

Shock-capturing schemes such as Roe's Riemann solver were principally developed for flows with a small number of isolated discontinuities. The fundamental characteristic of Godunov-based schemes is that the discontinuity in the left and right reconstructed states at a cell interface is treated as being conceptually similar to Riemann's initial-value problem. Hence, to impart stability and monotonicity to the solution, Riemann solvers represent the interface flux as the combination of a central-differenced flux term and a dissipation term. When extending such schemes to compressible turbulent flows with randomly fluctuating flow properties (see Chapter 4), Godunov schemes perceive a Riemann problem (i.e., a discontinuous jump) at every cell interface. To capture this perceived discontinuity, these solvers apply artificial dissipation everywhere in the domain. The resulting excessive numerical viscosity leads to unphysically high dissipation of turbulent kinetic energy, which is manifested as the non-recovery of the -5/3 power law of kinetic energy spectrum in

the inertial subrange. To alleviate the problem of excessive dissipation, Thornber et al. [9] developed an approach wherein the artificially large velocity jumps due to Godunov schemes are reduced by incorporating a Mach-number-dependent z-factor into the reconstruction, as follows.

$$\mathbf{u}_L = \frac{\mathbf{u}_L + \mathbf{u}_R}{2} + z\frac{\mathbf{u}_L - \mathbf{u}_R}{2} \tag{3.76}$$

$$\mathbf{u}_R = \frac{\mathbf{u}_L + \mathbf{u}_R}{2} + z\frac{\mathbf{u}_R - \mathbf{u}_L}{2} \tag{3.77}$$

Here $z = \min[1, \max(M_L, M_R)]$ is a Mach-number-dependent factor that increasingly central differences velocity with decreasing Mach number [9], thereby removing the $O(1/M)$ dependence of numerical dissipation.

The current study adopts this approach but with two distinctions. First, the z-factor is applied directly to the numerical viscosity, instead of to the jump in state variables at an interface. Second, the factor is applied to all conservation variables, and not just to the velocity components. The Roe-MUSCL flux with Harten's correction and the z-factor then becomes:

$$(\mathbf{F}_Q \cdot \mathbf{n})_f = \mathbf{F}_{CDS} - \frac{z}{2}\left(\mathbf{I} - \frac{\mathbf{\Psi}}{\Lambda}\right)\left[\sum_\theta \tilde{\mathbf{R}}_\theta \, |H(\tilde{\mathbf{\Lambda}}_\theta)| \, \tilde{\mathbf{L}}_\theta\right](\mathbf{Q}_R - \mathbf{Q}_L) \tag{3.78}$$

where M_L and M_R are the Mach numbers based on the left and right velocities at an interface. The z-factor acts as a shock detection switch [82] that reduces numerical viscosity in the subsonic regions of the turbulent flow. The scaled numerical viscosity

matrix is now denoted as $\boldsymbol{\nu}_{\mathrm{RMH}z}$, and is given by

$$\boldsymbol{\nu}_{\mathrm{RMH}z} = \frac{z}{2}\left(\mathbf{I} - \frac{\boldsymbol{\Psi}}{\Lambda}\right)\left|H(\tilde{\mathbf{A}}_n)\right|\ (\mathbf{d}\cdot\mathbf{n})_f \tag{3.79}$$

where the subscript RMHz refers to the Harten-corrected Roe-MUSCL scheme with the current z-factor modification.

The components of the numerical viscosity matrix corresponding to the individual conservation variables are:

$$\begin{aligned}
\nu_\rho &= \frac{z}{2}\left(1 - \frac{\psi_\rho}{\Lambda}\right) \\
&\quad (H(|\tilde{u}-\tilde{a}|)\ n_x + H(|\tilde{v}-\tilde{a}|)\ n_y + H(|\tilde{w}-\tilde{a}|)\ n_z)(\mathbf{d}\cdot\mathbf{n})_f && (3.80)\\
\nu_{\rho u} &= \frac{z}{2}\left(1 - \frac{\psi_{\rho u}}{\Lambda}\right)(H(|\tilde{u}|)\ n_x + H(|\tilde{v}|)\ n_y + H(|\tilde{w}|)\ n_z)(\mathbf{d}\cdot\mathbf{n})_f && (3.81)\\
\nu_{\rho v} &= \frac{z}{2}\left(1 - \frac{\psi_{\rho v}}{\Lambda}\right)(H(|\tilde{u}|)\ n_x + H(|\tilde{v}|)\ n_y + H(|\tilde{w}|)\ n_z)(\mathbf{d}\cdot\mathbf{n})_f && (3.82)\\
\nu_{\rho w} &= \frac{z}{2}\left(1 - \frac{\psi_{\rho w}}{\Lambda}\right)(H(|\tilde{u}|)\ n_x + H(|\tilde{v}|)\ n_y + H(|\tilde{w}|)\ n_z)(\mathbf{d}\cdot\mathbf{n})_f && (3.83)\\
\nu_{\rho e_t} &= \frac{z}{2}\left(1 - \frac{\psi_{\rho e_t}}{\Lambda}\right) \\
&\quad (H(|\tilde{u}+\tilde{a}|)\ n_x + H(|\tilde{v}+\tilde{a}|)\ n_y + H(|\tilde{w}+\tilde{a}|)\ n_z)(\mathbf{d}\cdot\mathbf{n})_f && (3.84)
\end{aligned}$$

It is evident from (3.80)-(3.84) that only the eigenvalues of the Jacobian matrix $|\tilde{\mathbf{A}}_n|$ contribute to the numerical viscosity. The viscosity in the continuity and energy equations arises due to the left- and right-traveling acoustic waves, respectively, while that in the three momentum equations contains contributions from both the entropy and shear waves. Since numerical viscosity $\boldsymbol{\nu}_{\mathrm{RMH}z}$ is a tensor, there are multiple ways of quantitatively representing this tensor. For example, the first tensor invariant,

$\mathrm{Tr}\left(\boldsymbol{\nu}_{\mathrm{RMH}z}\right) = \nu_\rho + \nu_{\rho u} + \nu_{\rho v} + \nu_{\rho w} + \nu_{\rho e_t}$, may be used to represent the overall viscosity inherent to TVD-MUSCL for Euler equations.

The effects of Harten's entropy correction, z-factor and limiter ψ_i on the numerical viscosity of Roe-based schemes are qualitatively illustrated in Figure 3.4. Numerical viscosities inherent to Lax-Wendroff and Roe are also included for reference. As is well known, Lax-Wendroff scheme applies the bare minimum amount of viscosity that ensures stability but not monotonicity. Roe's numerical viscosity, higher than Lax-Wendroff's, ensures both stability and monotonicity. Harten's correction further increases Roe's viscosity for a certain range of eigenvalues $[-\delta, \delta]$ so that the entropy condition is not violated. The arrows indicate the direction in which viscosity reduces as ψ_i increases and z decreases. The effects of the z-factor on viscosity may also deduced from the dependence of z on Mach number which scales with wavespeed λ_i.

The numerical viscosities in (3.80)-(3.84) are evaluated at a cell face. In the current study, the cell-centered viscosity is obtained using the interpolation scheme given by equation (2.28).

3.6.6 High Resolution Flux Limiters

The TVD limiters considered in this chapter are minmod, van Leer and superbee. A detailed investigation of the diffusive characteristics of these limiters was conducted by Bidadi and Rani [80] (see Chapter 2) for the scalar advection equation. The dimensionless quantity r in the limiter $\psi(r)$ is again computed using Darwish and Moukalled's formulation [4] that was derived specifically for unstructured meshes.

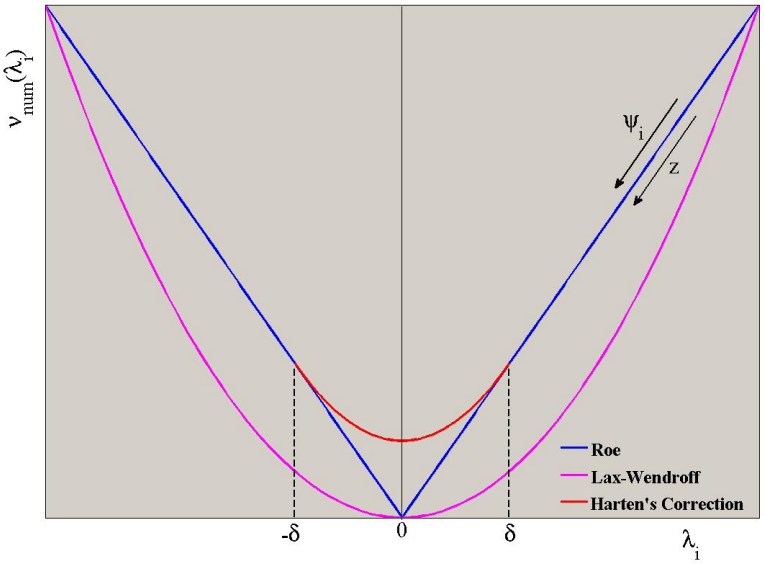

Figure 3.4: Qualitative comparison of numerical viscosity ν_{num} as a function of wavespeed λ_i for Roe, Lax-Wendroff, and Harten's schemes [6].

The advantage of Darwish and Moukalled's expression is that it requires information only from the left and right centroids of the interface. For the Euler equations, r factors are determined for each of the conserved variables as follows.

$$r_{Q_i} = \frac{\left[2(\nabla Q_i)_{(L,c)} \cdot \mathbf{r}_{L,c\to R,c}\right]}{(Q_i)_{(R,c)} - (Q_i)_{(L,c)}} - 1 \tag{3.85}$$

where L,c and R,c are the cell centroids to the left and right of an interface, Q_i corresponds to the i^{th} conserved variable in the vector $\mathbf{Q}$, and $(\nabla Q_i)_{(L,c)}$ refers to the spatial gradient of Q_i at the left cell centroid.

3.7 Results

Using the developed numerical viscosity formulation, dissipation characteristics of the Roe-MUSCL scheme are studied for: (1) 1-D shock tube, (2) 2-D inviscid supersonic wedge flow. The TVD limiters considered are minmod, van Leer and superbee. The effects of Thornber et al. [9] z-factor, as well as of the current z-factor on numerical viscosity are quantified. For both cases, spatial profiles of numerical viscosity are shown.

3.7.1 1-D Shock Tube Problem

Sod's 1-D shock-tube problem is a fundamental test case to validate Riemann solvers such as Roe-MUSCL. The initial conditions are obtained from Sod's study [83] with the diaphragm initially located at $x_0 = 0.5$ and the thermodynamic variables being assigned the following values: $\rho_L = 1.0, p_L = 1.0, u_L = 0.0, \rho_R = 0.125, p_R = 0.1, u_R = 0.0$. The domain of unit length was discretized into 100 cells. Simulations were conducted with a CFL number of 0.5 and for a time of 0.225 time-units. The results presented here are at $t = 0.225$. Harten's correction with the threshold parameter $\delta = 3$ was chosen for this problem.

Figure 3.5 shows the density and numerical viscosity profiles for five cases: (1) Roe's first-order Riemann solver; and Roe-MUSCL scheme with (2) minmod limiter and scaling factor $\Lambda = 2$; (3) van Leer limiter and $\Lambda = 2$; (4) superbee limiter and $\Lambda = 2$; and (5) minmod limiter and $\Lambda = 1$. All five simulations were conducted without the z-factor modifications to the diffusive flux. The density profiles in Figure 3.5(a)

show the Roe's scheme (Case 1) to be the most diffusive, and minmod with $\Lambda = 1$ (Case 5) to be the least diffusive among the TVD schemes considered. This trend is confirmed by the profiles of the trace of numerical viscosity, $\nu_{\text{num}} = \text{Tr}\left(\boldsymbol{\nu}_{\text{RMH}_z}\right) = \nu_\rho + \nu_{\rho u} + \nu_{\rho v} + \nu_{\rho w} + \nu_{\rho e_t}$, shown in Figure 3.5(b). It is seen that minmod with $\Lambda = 1$ provides the least amount of numerical viscosity in most regions of the flow, particularly in regions upstream of the shock and contact discontinuity. Roe's scheme provides uniformly high numerical viscosity throughout the domain. It is therefore clear that minmod limiter not only minimizes numerical viscosity in smooth regions, but also provides the appropriate amount of viscosity near discontinuities so as to ensure stability and monotonicity. Among Cases 2, 3 and 4 with $\Lambda = 2$, superbee supplies the minimum viscosity. The effect of the Λ parameter can be deduced by comparing Cases 2 and 5. It is evident that $\Lambda = 2$ results in higher numerical viscosity, which has important implications when applying Roe-MUSCL to simulate turbulent flows.

The effects of z-factor on the shock tube solution are shown in Figure 3.6 for three scenarios: (1) No z-factor modification (NM), which is equivalent to setting $z = 1$ in equations (3.80)-(3.84); (2) Current z-factor modification (CM); and (3) Thornber et al. z-factor modification (LM [9]). The CM approach, described by equations (3.80)-(3.84), involves a direct modification of numerical viscosity without affecting the variable jump at an interface $\mathbf{Q}_R - \mathbf{Q}_L$. In the LM [9] approach, the z-factor reduces the jump in velocity vector at the interface, $\mathbf{u}_R - \mathbf{u}_L$.

All three scenarios employ Roe-MUSCL with minmod and $\Lambda = 1$. Profiles of density, velocity, pressure and numerical viscosity are shown in Figure 3.6(a)-

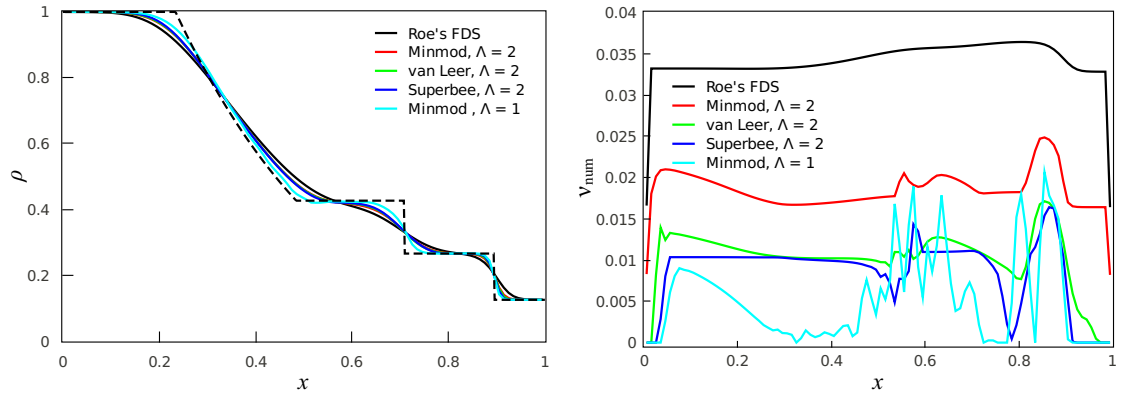

(a) Density (b) Numerical Viscosity

Figure 3.5: Profiles of (a) density, and (b) numerical viscosity are compared for five cases without the z-factor modification: (1) Roe's original flux-difference splitting (FDS) scheme; and Roe-MUSCL with (2) minmod limiter and $\Lambda = 2$; (3) van Leer limiter and $\Lambda = 2$; (4) superbee limiter and $\Lambda = 2$; and (5) minmod limiter and $\Lambda = 1$.

Figure 3.6(d), respectively. While the profiles of density, velocity, and pressure are apparently similar for NM, CM and LM [9], careful observation reveals that the profiles corresponding to the current modification are the least diffusive. This is also confirmed by the numerical viscosity shown in Figure 3.6(d). While the numerical viscosity profiles for NM, CM and LM [9] are similar near discontinuities, away from them CM provides least viscosity. In fact, the viscosity of CM is nearly zero across the rarefaction fan.

3.7.2 2-D Supersonic Flow over Wedge

The freestream conditions for this problem are: Mach number $M_\infty = 2$, pressure $p_\infty = 1$bar, and temperature $T_\infty = 273.15$K. The wedge deflection angle is 10°. Boundary conditions enforced at the wall are described by the following pressure

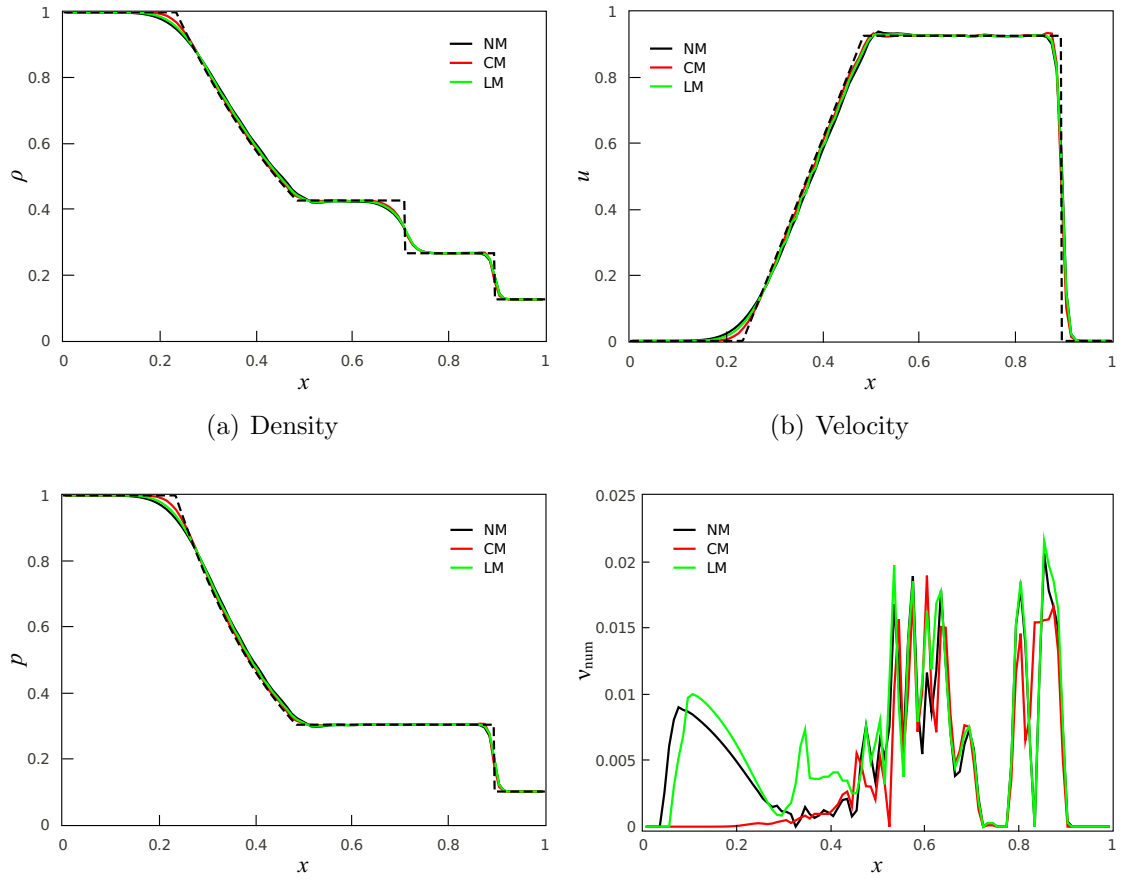

(a) Density (b) Velocity

(c) Pressure (d) Numerical Viscosity

Figure 3.6: Comparison of (a) density, (b) velocity, (c) pressure, and (d) numerical viscosity profiles for no modification (NM), current modification (CM) and Thornber et al. Low-Mach number modification (LM [9]) cases. Minmod limiter and $\Lambda = 1$ were applied for all three scenarios.

extrapolation method [84]:

$$(\mathbf{F}_Q \cdot \mathbf{n})_{\text{wall}} = p_{\text{wall}} \cdot [0 \; n_x \; n_y \; 0]^{\text{T}} \tag{3.86}$$

Here $\mathbf{F}_Q$ represents the fluxes of conservation variables, and $\mathbf{n}$ is the normal vector.

The pressure at the wall p_{wall} is computed by linearly extrapolating the pressure from

the boundary cell to the face. Equation (3.86) satisfies both slip and no-penetration boundary conditions for the wall-tangential and wall-normal velocity components, respectively.

The steady-state contours of density, Mach number and numerical viscosity $\nu_{\text{num}} = \text{Tr}\,(\boldsymbol{\nu}_{\text{RMH}z})$ are shown in Figure 3.7. These results are for minmod limiter, $\Lambda = 1$ and no z-factor modification (NM). Simulations conducted with either CM or LM [9] have no impact on the contours. The oblique shock at the compression corner is evident from the contours of density and Mach number in Figure 3.7(a) and Figure 3.7(b). The width of the shock essentially remains constant along the length of the wedge. Figure 3.7(c) shows that the numerical viscosity is maximum at/near the compression corner. This large increase in numerical viscosity is necessary to prevent the occurrence of overshoots or undershoots when capturing the sharp gradients in flow and thermodynamic variables in this region. Downstream of the oblique shock, the viscosity is quite small, which is also the case all along the wall.

The steady-state spatial profiles of density and numerical viscosity along the $y = 0.5$ line are presented in Figure 3.8. As for the shock-tube problem, these profiles are shown for five cases (without the z-factor modification): (1) Roe's scheme; and Roe-MUSCL scheme with (2) minmod limiter and scaling factor $\Lambda = 2$; (3) van Leer limiter and $\Lambda = 2$; (4) superbee limiter and $\Lambda = 2$; and (5) minmod limiter and $\Lambda = 1$. It can be seen from the density profiles shown in Figure 3.8(a) that Roe's scheme is most diffuse, while that for minmod limiter with $\Lambda = 1$ is least diffuse. These trends are also reflected in the numerical viscosity profiles shown in Figure 3.8(b). Clearly, the original Roe scheme has the maximum viscosity. Among the two minmod cases,

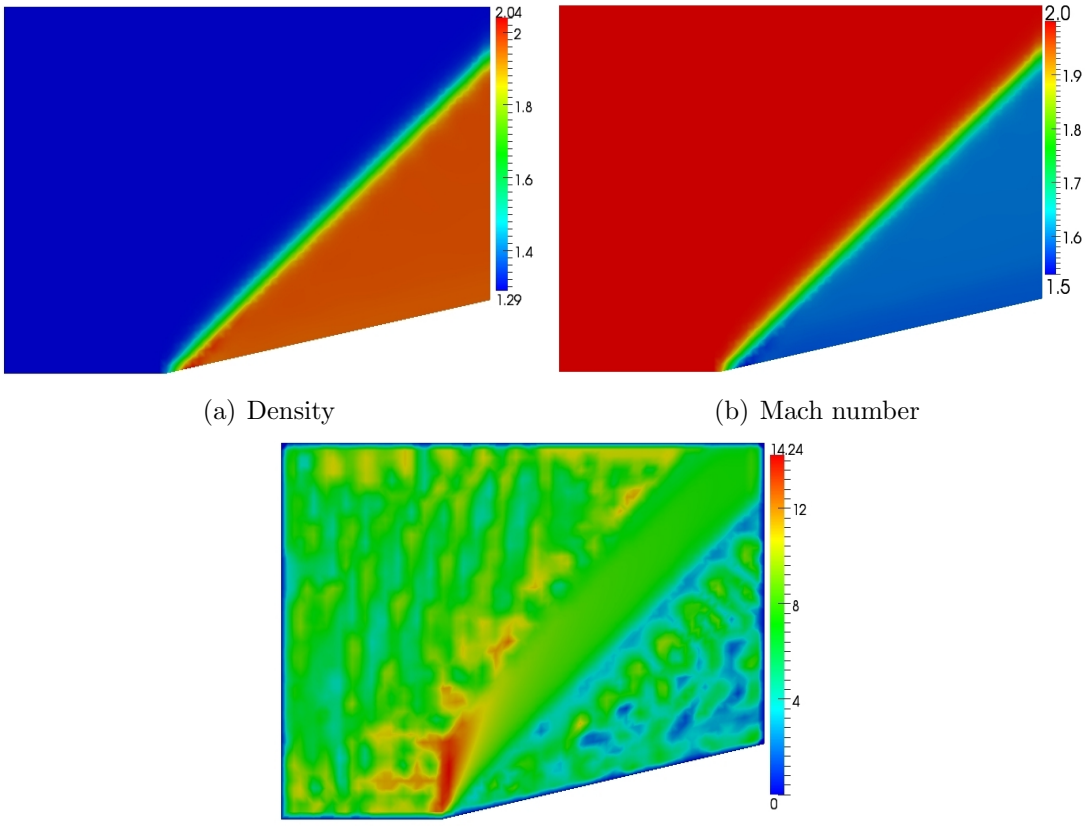

(a) Density

(b) Mach number

(c) Numerical Viscosity

Figure 3.7: Isocontours of (a) density, (b) Mach number and (c) numerical viscosity for 2-D inviscid supersonic flow over a wedge. Results are for a mesh resolution of 3626 cells. Minmod limiter and $\Lambda = 1$ were applied with no z-factor modification (NM).

the case with $\Lambda = 2$ results in higher numerical viscosity when compared to the case with $\Lambda = 1$. For all cases, there is a rise in the magnitude of viscosity immediately upstream of the shock front, which is necessary to resolve the shock while maintaining stability and preventing spurious oscillations. The effects of z-factor on the solution are shown in Figure 3.9 for three scenarios: (1) No z-factor modification (NM); (2) Current z-factor modification (CM); and (3) Thornber et al. z-factor modification (LM [9]). Profiles shown are along the $y = 0.1$ line, and were obtained using two

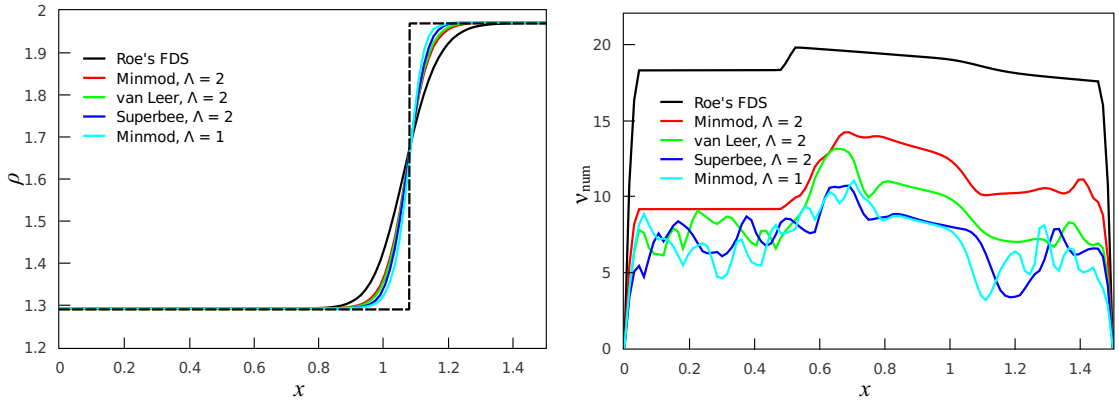

(a) Density (b) Numerical Viscosity

Figure 3.8: Profiles of (a) density, and (b) numerical viscosity along the $y = 0.5$ line are compared for five cases: (1) Roe's original flux-difference splitting (FDS) scheme; and Roe-MUSCL with (2) minmod limiter and $\Lambda = 2$; (3) van Leer limiter and $\Lambda = 2$; (4) superbee limiter and $\Lambda = 2$; and (5) minmod limiter and $\Lambda = 1$.

combinations: superbee with $\Lambda = 2$, and minmod with $\Lambda = 1$. For each of the two combinations, it is observed that the NM, CM and LM [9] profiles for density and numerical viscosity are identical since $z = 1$ throughout the domain. Comparing the density profiles of the two limiters, it can be seen that minmod with $\Lambda = 1$ violates the TVD-Monotonicity criterion as it exhibits noticeable over-shoot downstream of the shock. This is primarily due to insufficient numerical viscosity (see Figure 3.9(b)) supplied by this scheme in this region compared to superbee with $\Lambda = 2$.

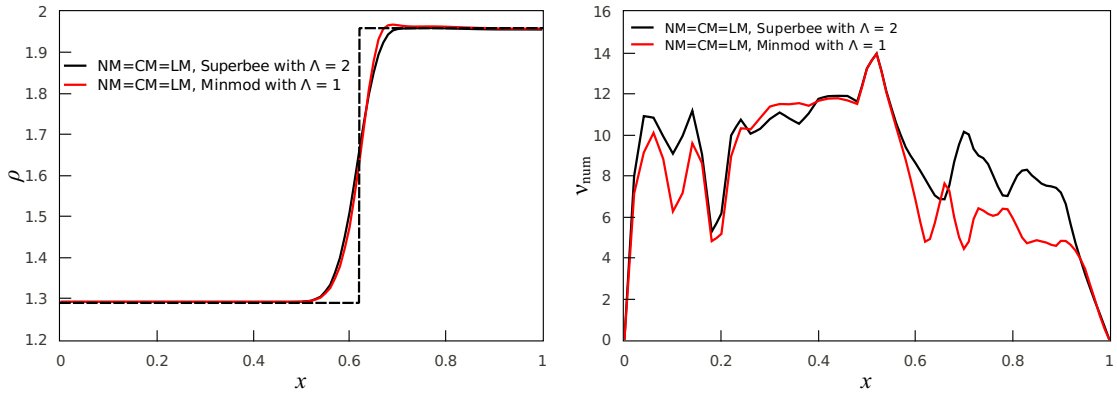

(a) Density

(b) Numerical Viscosity

Figure 3.9: Comparison of (a) density, and (b) numerical viscosity profiles along the $y = 0.1$ line for no modification (NM), current modification (CM) and Thornber et al. modification (LM [9]) cases. Minmod with $\Lambda = 1$, and superbee with $\Lambda = 2$ were considered. Results are for a mesh resolution of 3626 cells. The profiles for NM, CM and LM [9] schemes are identical for both limiter-Λ combinations.

CHAPTER 4

DECAYING COMPRESSIBLE ISOTROPIC TURBULENCE

4.1 Introduction

Compressible turbulent flows are significantly more challenging to simulate than incompressible flows. The numerical algorithms and turbulence models must work in tandem to preserve both the mathematical as well as physical symmetries which are considerably larger in compressible fluids [2]. Incompressible fluids are fully characterized by the velocity field since the pressure is correlated with the velocity field through the divergence-free criterion. However, in the case of compressible flows, an equation of state for pressure is necessary and hence the above condition no longer holds true. There are in general two main approaches to analyzing compressible flows; *Kovasznay decomposition* [85] and *Helmholtz decomposition*. The former is based on the assumption that the turbulent fluctuations are small compared to the mean flow. This allows for the decomposition of the velocity field into acoustic, entropy and vorticity modes. However, such a decomposition is limited to flows that does not exhibit significant compressibility. Kovasznay approach begins by performing

asymptotic expansions of the flow quantities as follows:

$$\begin{aligned} \mathbf{u} &= \mathbf{u}_0 + \epsilon \mathbf{u}_1 + \epsilon^2 \mathbf{u}_2 + ... \\ \rho &= \rho_0 + \epsilon \rho_1 + \epsilon^2 \rho_2 + ... \\ p &= p_0 + \epsilon p_1 + \epsilon^2 p_2 + ... \\ s &= s_0 + \epsilon s_1 + \epsilon^2 s_2 + ... \end{aligned} \tag{4.1}$$

Substituting the above expansions (excluding ϵ^2 terms) into the Navier-Stokes equations results in a linearized set of equations for each of the three modes. The vorticity mode is present in both incompressible and compressible flows. Although linear decomposition makes it possible to analyze the three physical modes, it fails to account for the interaction between them. In a subsequent paper, Chu and Kovasznay [86], accounted for the modal interactions by including the terms of the order of ϵ^2 in (4.1). In flows where non-linear mechanism dominates, the well known Helmholtz decomposition is typically applied to the velocity field [87]

$$\mathbf{u} = \mathbf{u}_s + \mathbf{u}_d \tag{4.2}$$

where $\mathbf{u}_s$ is the solenoidal component satisfying the divergence-free condition $\nabla \cdot \mathbf{u}_s = 0$, and $\mathbf{u}_d$ is irrotational since $\nabla \times \mathbf{u}_s = 0$. A similar decomposition in the Fourier space was proposed by Moyal [88].

In order to investigate the performance of new numerical schemes or turbulence models, researchers typically conduct decaying homogenous isotropic turbulence

(HIT) simulations first. It is the simplest form of turbulent motion that provide us with a fundamental understanding of the fine-scale structure of both compressible and incompressible turbulent flows [89]. Most of the turbulence theories are based on such idealized form of turbulent motion. In fact, a number of popular subgrid-scale (SGS) models were developed specifically for such flows. The first documented simulation of DNS of compressible isotropic turbulence was performed by Feiereisen et al. [90]. Numerical experiments conducted since then have shown the existence of three dynamical regimes in decaying isotropic turbulent flows. These are low-Mach number quasi-isentropic regime, nonlinear subsonic regime and supersonic regime. The effects of compressibility in the domain are characterized to the first order by the turbulent Mach number (M_t) and is defined as [2]

$$M_t = \frac{\sqrt{3}\ u_{\text{rms}}}{\langle c \rangle} \tag{4.3}$$

where $u_{\text{rms}} = \left(\frac{1}{3}\langle u^2 + v^2 + w^2 \rangle\right)^{1/2}$ is the rms turbulent fluctuating velocity, and $\langle c \rangle$ is the mean sound speed. The domain is considered quasi-isentropic for $M_t \leq 0.2 - 0.4$. The flow regime is characterized by weak interactions between acoustic and vorticity modes as compared to their respective self-interactions. As a result, the energy transfer from vorticity to acoustic modes is of very small intensity and the flow is considered weakly compressible. The entropy modes do not play a significant role in this flow regime.

In the case of non-linear subsonic regime ($0.4 \leq M_t \leq 1.0$), prior DNS studies [87, 91, 92] have shown the non-linear interactions between dilatational and

solenoidal velocity components to be sufficiently strong to trigger the formation of eddy shocklets. These weak normal shocks, generated due to complex interactions among turbulent eddies [2,91], satisfy the Rankine-Hugoniot jump conditions. About 1/3 of the total volume is associated with compression ($\nabla \cdot \mathbf{u} < 0$) and the rest expands the flow. The decay of turbulent kinetic energy in this case is given by the following expression [91]:

$$\frac{\partial}{\partial t}\left\langle \frac{1}{2}\rho u_i u_i \right\rangle = -\left\langle \frac{4}{3}\mu\theta^2 \right\rangle - \langle \mu\omega_i\omega_i \rangle + \langle p\theta \rangle \tag{4.4}$$

where the first term on the RHS is the compressible dissipation ϵ_d, second is the solenoidal dissipation ϵ_s and the third is pressure-dilation transfer term, respectively. Prior studies have reported ϵ_d to be less than 10% of the total dissipation. Moreover, shocklets are responsible for up to 20% of the total dilatational dissipation.

The supersonic regime corresponds to $M_t \geq 1$. There have been very few numerical experiments conducted for this flow regime since it is encountered primarily in the field of astrophysics. Porter et al. [93] performed the first successful numerical experiment for this case. Their ILES simulations at $M_t = 1.0$ showed three phases in the development of the flow: (i) "onset phase" which culminates with formation of shocks; (ii) supersonic phase consisting of strong density gradients; and (iii) post-supersonic phase that is dominated by vortex interaction and vortical decay [30]. Inertial subrange is absent and interscale energy transfer is mainly due to nonlinear acoustic phenomena and shock wave interactions. Hence, the LES-SGS models are

not valid and shock-capturing schemes seem to be the most adequate way of capturing the flow physics.

Until recently, LES research of turbulent flows focused mainly on incompressible fluids. In the case of high-speed compressible flows, SGS models must not only account for interscale energy transfer but also the energy exchange between acoustic, entropy and vorticity modes. The latter is not considered by traditional subgrid models. To address this issue, a number of advanced models have been developed recently [94]. But most are highly complex, computational expensive and may not accurately represent the compressible flow phenomena. Hence, there has been increasing interest in the use of shock-capturing (Godunov-type) schemes to not only mimic LES-SGS models but to also capture the intermodal energy transfer present in highly compressible regions of the flow. As discussed in Chapter 1, this relatively new approach to turbulence modeling is termed implicit large-eddy simulation (ILES).

Recent ILES research involves, among other aspects, extending Godunov-based schemes to low Mach number turbulent flows. Such an extension gives rise to two main problems—the stiffness problem and the accuracy problem [73]. The *stiffness problem* results from the increased spread in acoustic and entropy wave speeds as the Mach number decreases, which unless controlled can lead to rapid accumulation of numerical instabilities resulting in solution "blow-up". The *accuracy problem* for low Mach number turbulent flows results from the increased numerical dissipation that has been shown to be $O(1/M)$ [39], where M is the local Mach number. Garnier et al. [30] performed an extensive investigation of the dissipative properties of high-resolution and high-order shock capturing schemes when applied to freely decay-

ing isotropic turbulence with varying initial turbulent Mach numbers, compressibility ratios, and grid resolutions. They concluded that the dissipation inherent to these schemes was much greater than that due to SGS models in all flow regimes. Consequently, they do not capture the $-5/3$ slope of the turbulent energy spectrum in the inertial subrange. To minimize stiffness while maintaining accuracy (i.e., reduce dissipation), typically preconditioning techniques were applied that artificially reduce viscosity, as well as the large spread in the characteristic speeds at low Mach numbers.

Rider and Margolin [33] expanded the work of Garnier et al. [30] by deriving the orders of magnitude of 1-D dissipative fluxes in multiple high resolution schemes, as well as in a fifth order WENO scheme. They showed that for the minmod limiter, the nonlinear dissipation term was $\sim \Delta x^2$, while for the double minmod limiter and median limiter of the UNO scheme, it was $\sim \Delta x^3$. This scaling analysis suggests that while minmod is more "active" in the inertial subrange, the latter two limiters restrict dissipation to the highest wavenumbers. Rider and Margolin [33] also provided an explanation for the excessive dissipation of the 5^{th} order WENO scheme tested by Garnier et al. [30]. Their analysis showed that the highly dissipative nature of the WENO scheme was primarily due to the higher order interpolation being applied to the fluxes rather than to the variables themselves.

Thornber et al. [59] performed a detailed quantitative investigation of the behavior of a number of high-resolution and high-order methods in ILES of homogeneous decaying turbulence. They presumed that since the entropy rise across a shock scales as $O(\Delta u^3)$ and because shock wave is a solution to the Riemann problem at an interface, the local entropy and consequently the dissipation rate at an interface must also

be of the same order. This scaling is analogous to the Kolmogorov hypothesis [22, 95] that relates dissipation rate to the third-moment of the turbulent fluctuating velocity. In a subsequent study, Thornber et al. [39] performed a fundamental theoretical analysis to demonstrate that the entropy increase at an interface is $O(\Delta u^2)$, and not $O(\Delta u^3)$ as previously thought. Consequently, the dissipation rate of kinetic energy (related to the product of temperature and entropy change) scales as $O(\Delta u^2 \cdot a)$, where a is the speed of sound. Motivated by this [39] study, Thornber et al. [9] developed a modified velocity reconstruction process, wherein the jump in the velocity vector at a cell interface is reduced by incorporating a Mach-number-dependent z-factor into the reconstruction. Since the diffusive flux is directly proportional to the jump in state variables at the cell interface, the modified reconstruction would result in reduced numerical dissipation.

To better understand the behavior of Godunov-based schemes when simulating turbulent flows, it is important to gain quantitative insights into the numerical viscosity inherent to such schemes. Here, we utilize the 3-D Roe-MUSCL flux formulation derived in Chapter 3. The motivating factor for choosing high-resolution upwind-biased schemes based on Roe's formulation [40] is their superior ability to capture both the shock front and its speed when compared to other common linearized Riemann solvers. Roe's scheme, however, suffers from the problem of excessive dissipation due to the tendency of "perceiving" a Riemann problem at every cell interface, irrespective of whether the interface is located in smoothly varying or high-gradient regions. To alleviate this artifact, a Mach-number-dependent z-factor, motivated by [9], is introduced that reduces the viscosity considerably in low Mach number flow

fields. The current study applies Roe-MUSCL flux directly to the conservative form of the Euler equations, while prior studies such as [73] considered the characteristic form of the Euler equations. In the latter form, the convective fluxes are expressed in terms of the propagation of characteristic variables or Riemann invariants along their respective characteristics with the corresponding eigenspeeds. As demonstrated for the case of scalar advection equation by the current authors [80], the form and effects of numerical viscosity can be readily deduced by using the conservative form, rather than the characteristic form, of the governing equations.

In this chapter, the Roe-MUSCL scheme together with Thornber et al. [9] z-factor modification and its variant is investigated for decaying isotropic turbulence (HIT) with varying degrees of compressibility. The purpose of this study is to address why Godunov-based ILES approach with modifications is a viable alternative to LES approach at all Mach number turbulent flows. Compressibility is modulated by varying the initial turbulent Mach number considered, M_{t_0}. Three turbulent Mach numbers are considered along with varying grid resolution. The quantified numerical viscosity (see Chapter 3) and dissipation rate are investigated in spectral space. These spectra enable us to gain quantitative insights into the wavenumber range where the effects of dissipation are most significant. It is seen that both the current and Thornber et al. [9] modifications perform similarly in terms of reducing dissipation, except in a few cases where the current approach performs marginally better in capturing Kolmogorov's slope.

4.2 Compressible Isotropic Turbulence Statistics

In decaying compressible homogeneous isotropic turbulence (HIT), the temporal evolution of velocity fluctuations and other quantities of interest depends mainly on the initial conditions of three parameters: turbulent Mach number M_t (4.3), compressibility ratio χ, and the thermodynamic state [2]. The compressibility ratio χ, which is a measure of the fluid's compressibility, can be expressed as the ratio of the dilatational to total turbulent kinetic energies:

$$\chi = K_d/K \tag{4.5}$$

where $K = \frac{1}{2}\langle \rho \mathbf{u} \cdot \mathbf{u} \rangle$ is the total turbulent kinetic energy, and $K_d = \frac{1}{2}\langle \rho \mathbf{u}_d \cdot \mathbf{u}_d \rangle$ is the dilatational kinetic energy. Additional statistics such as velocity structure functions [30]- [39] are given by the following general expression

$$S_n = (-1)^n \frac{\langle \left(\frac{\partial u}{\partial x}\right)^n \rangle}{\langle \left(\frac{\partial u}{\partial x}\right)^2 \rangle^{\frac{n}{2}}} \tag{4.6}$$

Skewness ($n = 3$) is a measure of vortex stretching or compression [20] that provides information on the magnitude of turbulence, whereas, flatness ($n = 4$) is a measure of turbulence intermittency [92]. Both parameters vary with compressibility and turbulent (Taylor microscale) Reynolds number Re_λ defined as

$$Re_\lambda = \frac{u_{rms}\lambda}{\langle \nu \rangle} \tag{4.7}$$

where the Taylor microscale λ is

$$\lambda^2 = \frac{u_{rms}^2}{\langle(\partial u/\partial x)^2\rangle} \tag{4.8}$$

Skewness is closely related to enstrophy Ω which is expressed as

$$\Omega = \frac{1}{2}\langle|\nabla \times \mathbf{u}|^2\rangle \tag{4.9}$$

In addition to the above statistics, it is also necessary to estimate the rate of dissipation due to numerical viscosity in Roe-MUSCL. Garnier et al. [30] provided an approximation for the numerical dissipation rate in the momentum equations. Extending the Garnier et al. expression to all five governing equations yields the following expressions for the volume-averaged numerical diffusion of turbulent kinetic energy.

$$\epsilon_{\text{num},\rho}(t) = \left\langle \frac{1}{V} u_i u_i \sum_{f \in \text{cell faces}} [-(\mathbf{F}_{\text{Diss},\rho})_f \; A_f] \right\rangle \tag{4.10}$$

$$\epsilon_{\text{num},\rho u_\alpha}(t) = \left\langle \frac{1}{V} u_\alpha \sum_{f \in \text{cell faces}} [-(\mathbf{F}_{\text{Diss},\rho u_\alpha})_f \; A_f] \right\rangle \tag{4.11}$$

$$\epsilon_{\text{num},\rho e_t}(t) = \left\langle \frac{1}{V} \sum_{f \in \text{cell faces}} [-(\mathbf{F}_{\text{Diss},\rho e_t})_f \; A_f] \right\rangle \tag{4.12}$$

Here $\langle \cdots \rangle$ represent spatial averaging, V is the cell volume, A_f is the area of the cell face, $u_i u_i$ is the contraction of velocity, and u_α is one of the three velocity components; $\mathbf{F}_{\text{Diss},\rho}$, $\mathbf{F}_{\text{Diss},\rho u_i}$, and $\mathbf{F}_{\text{Diss},\rho e_t}$ are the components of $\mathbf{F}_{\text{Diss}}$ corresponding to the continuity, momentum, and energy equations, respectively. The other statistics computed in this study are the rms values of pressure (p'), specific volume (v'), and

temperature (T'), obtained using the following expressions: $p' = \frac{p_{\text{rms}}}{\gamma p_0 M_{t_0}^2}$, $v' = \frac{v_{\text{rms}}}{v_0 M_{t_0}^2}$, $T' = \frac{T_{\text{rms}}}{(\gamma-1)T_0 M_{t_0}^2}$. Another important parameter that is a measure of compressibility in the flow field is the rms of the velocity divergence, $\theta' = \langle(\partial u_i/\partial x_i)^2\rangle^{1/2}$. Finally, all statistics are plotted as functions of the initial eddy turn-over time τ defined as

$$\tau = \lambda_0/u_{rms,0} \tag{4.13}$$

4.3 Initial and Boundary Conditions

The simulation domain for decaying compressible isotropic turbulence is a triply-periodic cube. Three initial turbulent Mach numbers M_{t_0} are considered representing three flow regimes: quasi-isentropic, non-linear subsonic, and nearly incompressible. For the quasi-isentropic ($M_{t_0} = 0.3$) and non-linear subsonic ($M_{t_0} = 0.5$) flow regimes, the domain is initialized using the following energy spectrum [10, 82]:

$$E(k) = \frac{16}{3}\sqrt{\frac{2}{\pi}} M_{t_0}^2 \frac{k^4}{k_0^4} exp(-2k^2/k_0^2), \quad k_0 = 4 \tag{4.14}$$

where k is the wavenumber, and k_0 is the wavenumber at which the energy spectrum peaks. In this study, $k_0 = 4$. Using Rogallo's method [96], an isotropic Fourier-space velocity field is generated from (4.14). While this velocity field is divergence-free in Fourier space, the continuity equation is not exactly satisfied in physical space [20]. To reduce compressibility, we follow Feiereisen's [21] approach in which a vector potential ϕ is introduced as follows.

$$u_i^S = u_i^R + \frac{\partial \phi}{\partial x_i} \tag{4.15}$$

where u_i^R is the inverse Fourier transform of the random Fourier modes. Applying divergence on both sides of (4.15), the Laplacian of the potential $\nabla^2\phi = -\frac{\partial u_i^R}{\partial x_j}$. In the Fourier space, the vector potential is computed using $\widehat{\phi} = \frac{Ik_j\widehat{u}_j^R}{k^2}$, where $I = \sqrt{-1}$.

For the nearly incompressible isotropic turbulence case, $M_{t_0} = 0.1$. The velocity field for this case is initialized using the Comte-Bellot-Corrsin experimental data [23] at dimensionless time $tU_0/M = 42$, where U_0 is the free stream velocity, and M is the grid size for generating turbulent flow in their experiments. For all three Mach number cases, zero fluctuations in thermodynamic quantities are enforced.

4.4 Spectral Statistics

A useful way of determining the accuracy of a numerical scheme in HIT cases is to examine whether Kolmogorov's $-5/3$ slope can be captured upto the cut-off wavenumber $k_c = \pi/\Delta$, where $\Delta = (\Delta x \Delta y \Delta z)^{1/3}$ is the filter or cell size [2]. This requires computing the energy spectrum $E(k)$ using [21, 30]

$$E(k,t) = \sum_{|\mathbf{k}'|=k} \widehat{u}_i(\mathbf{k}',t)\ \widehat{u}_i^*(\mathbf{k}',t) \tag{4.16}$$

where k is the wavenumber magnitude, and the superscript $*$ refers to the complex conjugate. The solenoidal and dilatational energy spectra E_s and E_d may be obtained by using the respective velocity components in (4.16), where the dilatational Fourier mode is given by $\widehat{\mathbf{u}}^d(\mathbf{k},t) = [\mathbf{k}\cdot\widehat{\mathbf{u}}(\mathbf{k},t)]\,\mathbf{k}/k^2$, and the solenoidal mode by $\widehat{\mathbf{u}}_\mathbf{k}^s = \widehat{\mathbf{u}}_\mathbf{k} - \widehat{\mathbf{u}}_\mathbf{k}^d$ [30].

In addition to energy spectra, numerical viscosity and dissipation rate spectra can provide quantitative information on the numerical dissipation inherent to the scheme, and on its accuracy. A popular method to estimate the effective numerical viscosity for incompressible flows was proposed by Domaradzki et al. [97]. The procedure considers the transport equation for kinetic energy spectrum given by

$$\frac{\partial}{\partial t}E(k,t) = -2\widehat{\nu}k^2E(k,t) + T(k,t) \tag{4.17}$$

The first term on the RHS of (4.17) is the rate of dissipation of kinetic energy, while the second accounts for the nonlinear energy cascade. For inviscid flow simulations, $\widehat{\nu}$ in (4.17) is replaced by $\widehat{\nu}_{\text{num}}$ so that one may then estimate $\widehat{\nu}_{\text{num}}$ in Fourier space using [59, 97, 98]

$$\widehat{\nu}_{\text{num}}(k,t) = \frac{\widehat{\epsilon}_{\text{num}}(k,t)}{2k^2E(k,t)} \tag{4.18}$$

Here $\widehat{\nu}_{\text{num}}$ and $\widehat{\epsilon}_{\text{num}}$ are numerical viscosity and dissipation rate in Fourier space, and $\widehat{\nu}_{\text{num}}$ may be normalized as

$$\widehat{\nu}^{+}_{\text{num}} = \frac{\widehat{\nu}_{\text{num}}}{\sqrt{E(k_c)/k_c}} \tag{4.19}$$

where $E(k_c)$ is the spectral energy at cut-off wavenumber k_c.

Equation (4.18) provides a reasonably good approximation of numerical viscosity in the less compressible regions, but is inaccurate in highly compressible regions, as well as in the vicinity of shocks. In this study, the spectral numerical viscosity is estimated from the cell-centered values of ν_{RM} or ν_{RMH} or $\nu_{\text{RMH}z}$ of a conservation

variable of interest as follows.

$$\widehat{\nu}_{\text{num}}(k,t) = \sqrt{\sum_{|\mathbf{k}'|=k} \widehat{\nu}_{\text{num}}(\mathbf{k}',t)\ \widehat{\nu}^{*}_{\text{num}}(\mathbf{k}',t)} \tag{4.20}$$

When compared to (4.18), our formulation (4.20) is valid for all Mach numbers. In the current study, $\widehat{\nu}_{\text{num}}(k,t)$ is normalized using the reference value at the cut-off wavenumber:

$$\widehat{\nu}^{+}_{\text{num}} = \frac{\widehat{\nu}_{\text{num}}(k,t)}{\widehat{\nu}_{\text{num,ref}}(k_c,t)} \tag{4.21}$$

The spectral distribution of the numerical dissipation rate is then estimated from

$$\widehat{\epsilon}_{\text{num}}(k,t) = 2\ \widehat{\nu}_{\text{num}}(k,t)\ k^2 E(k,t) \tag{4.22}$$

where $\nu_{\text{num}}(k,t)$ is the spectral numerical viscosity computed from (4.20).

Although (4.22) is strictly valid for incompressible flows, it does provide a good measure of the numerical dissipation rate since compressibility effects are already incorporated into $\widehat{\nu}_{\text{num}}$. Moreover, prior DNS studies [91,92] of compressible isotropic turbulence have reported that for $M_{t_0} \leq 1.0$, the solenoidal dissipation ϵ_s dominates the dilatational dissipation ϵ_d at all times. Lee et al. [92] show ϵ_d to be less than 10% of the total dissipation for M_t of upto 0.6. Hence, equation (4.22) may be considered as a reliable estimate of dissipation spectrum. Numerical dissipation rate is normalized with the reference value at k_c as follows.

$$\widehat{\epsilon}^{+}_{\text{num}}(k,t) = \frac{\widehat{\epsilon}_{\text{num}}(k,t)}{\widehat{\epsilon}_{\text{num,ref}}(k_c,t)} \tag{4.23}$$

4.5 Results

Application of Roe-based TVD-MUSCL schemes to compressible decaying isotropic turbulence is the principal focus of this study. Three values of initial turbulent Mach number M_{t_0} corresponding to three different flow regimes were considered: $M_{t_0} = 0.1$ (nearly incompressible), $M_{t_0} = 0.3$ (quasi-isentropic), and $M_{t_0} = 0.5$ (nonlinear subsonic). The initial compressibility ratio $\chi_0 = 0$ (see (4.5)) and the initial thermodynamic state has zero fluctuations. The flow domain is a cubic periodic box with edge length $L \approx 2\pi$. The initial velocity field is generated using Rogallo's method [96], as discussed in Section 4.3. The CFL number for the $M_{t_0} = 0.1$ case is 0.2, while that for $M_{t_0} = 0.3$ and $M_{t_0} = 0.5$ cases is 0.1.

4.5.1 Nearly Incompressible Flow: $M_{t_0} = 0.1$

This case enables us to investigate the performance of TVD-MUSCL schemes when used for MILES of low-Mach-number turbulent flows. The effects of z-factor modification on numerical dissipation inherent to the schemes are also quantified. Simulations are performed using three grid resolutions, 32^3, 64^3 and 128^3. The results obtained are compared with the experimental data of Comte-Bellot and Corrsin [23].

In Figure 4.1 and Figure 4.2, energy spectrum $E(k)$ from current simulations is compared with that from Comte-Bellot and Corrsin (CBC) experiments at dimensionless time $tU_0/M = 98$, where U_0 is the free stream velocity, and M is the grid size for generating turbulent flow in CBC. Figure 4.1 shows the energy spectra for CBC, as well as for the following cases: Roe-MUSCL scheme with (1) minmod limiter and

$\Lambda = 2$; (2) van Leer limiter and $\Lambda = 2$; (3) superbee limiter and $\Lambda = 2$; and (4) minmod limiter and $\Lambda = 1$. All four cases include the effects of the current z-factor modification. It can be seen that at low wavenumbers, the four numerical spectra are nearly identical. However, closer to the cut-off wavenumber, it is seen that minmod with $\Lambda = 2$ is the most diffusive among the cases considered. In the context of ILES, a crucial observation in Figure 4.1 is that the dissipative effects of the TVD-MUSCL schemes are predominantly felt at high wavenumbers. This behavior is qualitatively similar to that of explicit SGS models whose eddy diffusivity is also weighted toward the high-wavenumber end of the resolved energy spectrum.

The numerical energy spectra shown in Figure 4.2(a) demonstrate the effects of the z-factor by considering three scenarios, all with minmod limiter and $\Lambda = 1$ on the 32^3 grid: (1) No z-factor modification (NM); (2) Current z-factor modification (CM); and (3) Thornber et al. z-factor modification (LM [9]). It is clear that TVD-MUSCL with no z-factor modification (NM) is extremely dissipative even when $\Lambda = 1$; NM with $\Lambda = 2$ would only make the scheme even more dissipative. But, the spectra obtained using current and original Thornber et al. z-factors, CM and LM respectively, show excellent agreement with the CBC experimental spectrum up to the cut-off wavenumber $k_c = 16$ even at the coarse resolution of 32^3. This suggests that the principal contributing factor to the excessive "dissipativeness" of TVD-MUSCL stems from the fact that Godunov-based schemes "perceive" a Riemann problem and apply numerical diffusion at every internal cell interface. Both CM and LM z-factor modifications are seen to successfully limit the scheme's perception of Riemann problem to high-gradient regions of the flow. Figure 4.2(b) is similar to Figure 4.2(a),

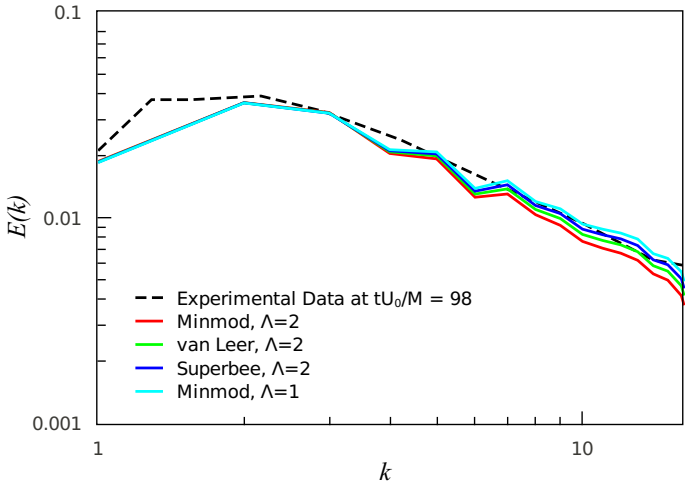

Figure 4.1: Comparison of energy spectra with CBC experimental data at $tU_0/M = 98$ for minmod, van Leer, and superbee limiters with $\Lambda = 2$; and minmod limiter with $\Lambda = 1$ on 32^3 mesh. All profiles were obtained using current modification (CM).

except that Figure 4.2(b) shows the spectra for a finer 64^3 grid. The trends are nearly the same for both grid resolutions. It is again observed that CM and LM spectra show good agreement with the CBC spectrum up to $k_c = 32$. Figure 4.3 presents the spectra of normalized numerical viscosity $\widehat{\nu}^+_{\text{num}}$ and normalized dissipation rate obtained using minmod and $\Lambda = 1$ on a 32^3 grid. Spectra are compared for cases with no z-factor modification (NM), current z-factor modification (CM) and Thornber et al. z-factor modification (LM). In Figure 4.3(a), the spectra of normalized numerical viscosity are shown, where normalization is as defined in (4.21). The viscosity at the cut-off wavenumber k_c from the NM case is used as the reference. There are interesting trends that need elucidation in Figure 4.3(a). At all wavenumbers, normalized viscosity for the CM case is the smallest, while the viscosities for NM and LM are very close to each other. The former is a manifestation of the fact that in CM, the

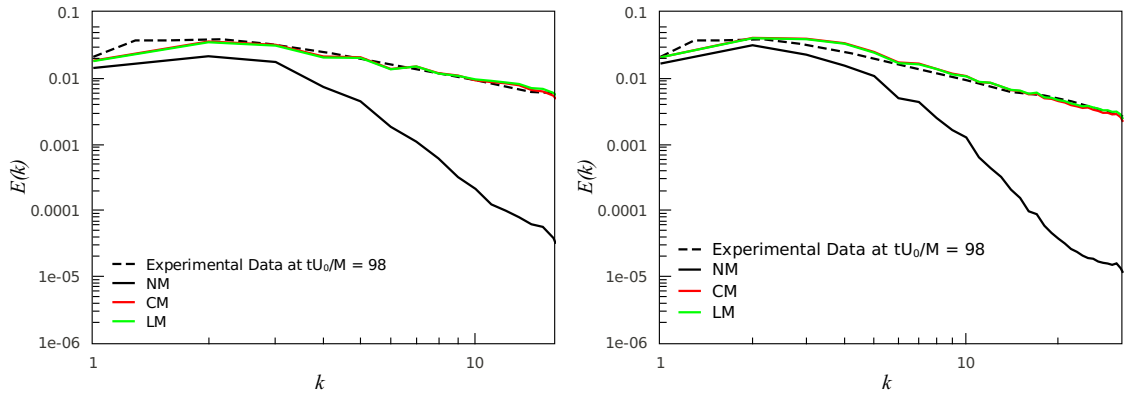

(a) 32^3 (b) 64^3

Figure 4.2: Comparison of energy spectra with CBC experimental data at $tU_0/M = 98$ for NM, CM and LM schemes with minmod limiter and $\Lambda = 1$ on (a) 32^3 mesh, and (b) 64^3 mesh.

z-factor is directly applied to reduce numerical viscosity , while in LM the z-factor is used to reduce the velocity jump at an interface without affecting the numerical viscosity.

The normalized dissipation rate spectra in Figure 4.3(b) provide greater clarity on the dissipative behavior of the three schemes. Here, normalization for each of the three modifications is done using their respective dissipation rate values at k_c. It is seen that the spectral dissipation rate of NM is much larger than that of both CM and LM for most of the spectrum, except near k_c where all three spectra collapse. This explains the highly dissipative $E(k)$ of NM in Figure 4.2. As expected, the dissipation spectra of CM and LM are quite close explaining the agreement between their energy spectra in Figure 4.2. It is also encouraging to see from Figure 4.3(b) that dissipation for both CM and LM increases with wavenumber peaking near k_c. This behavior is qualitatively similar to the role of SGS models in LES, and is crucial in order for

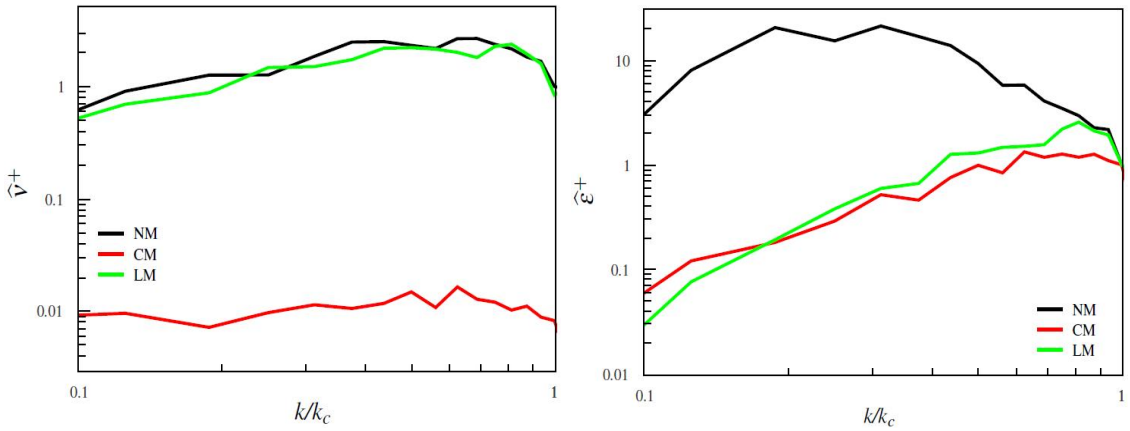

(a) Spectral numerical viscosity (b) Spectral dissipation rate

Figure 4.3: Spectra of (a) numerical viscosity and (b) dissipation rate for NM, CM and LM at $tU_0/M = 98$. Results are for a 32^3 mesh resolution. Minmod limiter with $\Lambda = 1$ was applied.

TVD-MUSCL to be a viable tool for ILES. The numerical viscosity and dissipation spectra for the 64^3 grid are shown in Figure 4.4. The overall trends are similar to those observed for the 32^3 grid shown in Figure 4.3. However, viscosity spectrum for CM shows a steeper rise and is larger compared to its 32^3 grid counterpart. The larger magnitude is a direct consequence of the higher amount of turbulent kinetic energy that is to be dissipated for the 64^3 case. The dissipation spectrum for CM is marginally higher than that for LM at all k/k_c. In the 32^3 case, we observed that the CM dissipation spectrum is slightly smaller than the LM spectrum at higher wavenumbers. The temporal evolution of skewness S_3 (see (4.6)) and dissipation rate ϵ are illustrated in Figure 4.5. NM and LM profiles are shown for the 32^3 grid, while CM profiles are shown for three grids: 32^3, 64^3 and 128^3. Since the initial velocity field is Gaussian distributed, skewness $S_3 = 0$ at $t = 0$. As shown in Figure 4.5(a), skewness of NM does not attain steady state during the simulation window. The

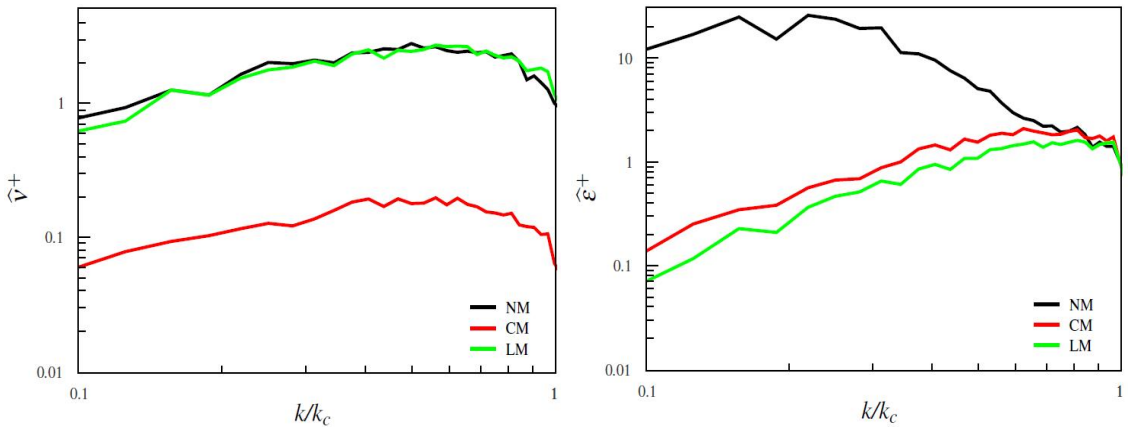

(a) Spectral numerical viscosity (b) Spectral dissipation rate

Figure 4.4: Spectra of (a) numerical viscosity and (b) dissipation rate for NM, CM and LM at $tU_0/M = 98$. Results are for a 64^3 mesh resolution. Minmod limiter with $\Lambda = 1$ was applied.

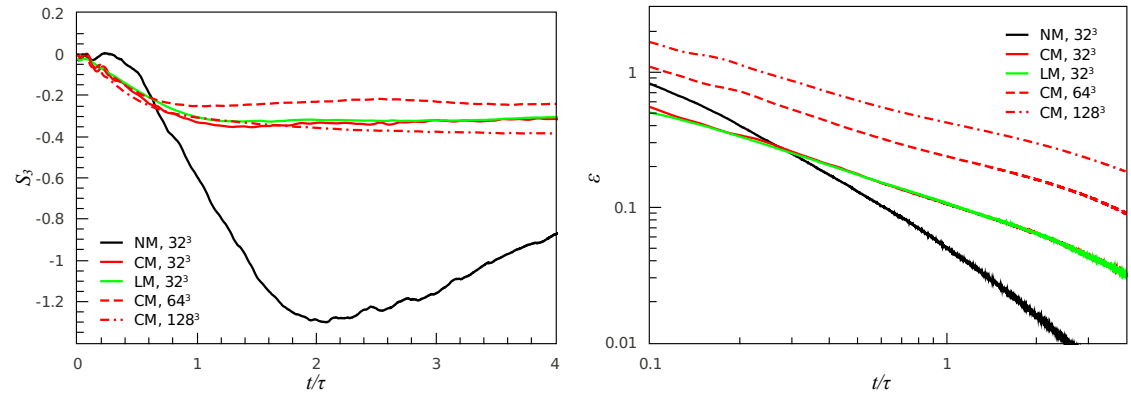

(a) Skewness (b) Dissipation rate

Figure 4.5: Comparison of profiles of (a) skewness and (b) dissipation rates for NM, CM and LM on 32^3 and 64^3 grid resolutions. Results of NM scheme on 128^3 grid are also presented. All profiles are for minmod limiter with scaling parameter $\Lambda = 1$.

skewness profiles for the z-factor modifications with 32^3 grid are close to one another, and approach a steady-state value of $S_3 \approx -0.31$. This value of skewness shows good agreement with the experimentally observed value of $S_3 \approx -0.34$ of Kang et al. [11] for Taylor microscale Reynolds number, $Re_\lambda = 720$. For CM with 64^3 grid, $S_3 \approx -0.24$. The decrease in $|S_3|$ is a bit surprising, since $|S_3|$ typically increases with grid refinement until it asymptotes to the DNS/experimental value. However, for CM with 128^3 grid, we indeed observe a drop to $S_3 \approx -0.35$, which agrees very well with the experimental value. The temporal evolution of dissipation-rate (ϵ) is shown in Figure 4.5(b). For NM with 32^3 grid, ϵ decays steeply with time suggesting an equally fast decay of turbulent kinetic energy. The LM and CM cases with 32^3 grid show nearly identical temporal profiles of dissipation, which is to be expected since the current and Thornber et al. [9] z-factor approaches provide similar amounts of dissipation. For CM with 64^3 and 128^3 grids, the dissipation magnitude increases with resolution, which may be attributed to the larger amount of residual turbulent kinetic energy in the domain.

4.5.2 Quasi-Isentropic Regime: $M_{t_0} = 0.3$

This section presents the results for the case with initial conditions $M_{t_0} = 0.3$, compressibility ratio $\chi_0 = 0$, and zero initial fluctuations in thermodynamic quantities. With these conditions, the flow may be considered weakly compressible [99]. The initial velocity field is generated using the procedure outlined in Section 4.3. Simulations were run for approximately three eddy-turnover times, using minmod

limiter with $\Lambda = 1$. All three z-factor modifications NM, CM and LM are considered, and their predictions compared.

Energy spectra at time $t/\tau = 2$ on 32^3 and 64^3 grids for NM, CM and LM are shown in Figure 4.6. It is seen that NM is excessively dissipative, and consequently fails to capture the inertial subrange. The current and Thornber et al. [9] z-factor modifications both lead to reduced dissipation, thereby their energy spectra are closer to Kolmogorov's $-5/3$ slope. Yet, even with CM and LM, energy at high wavenumbers is subjected to greater than optimal dissipation. Energy spectra for the solenoidal and dilatational velocity components, $E_s(k)$ and $E_d(k)$ respectively, are plotted in Figure 4.7 for the same grids. These spectra are shown at the early time $t/\tau = 0.4$ so as to demonstrate the temporal rate at which energy is accumulated in the solenoidal and dilatational modes. It is observed that $E_d(k)$ builds up faster and contains more energy at high wavenumbers when compared to $E_s(k)$ on both grids. Moreover, E_d exceeds E_s for a greater range of wavenumbers on the 64^3 grid than on the 32^3 grid. This indicates a relatively slower development of modes on the finer grid. Figure 4.8 shows the profiles of normalized numerical viscosity and dissipation spectra at $t/\tau = 2$ on 32^3 and 64^3 grids. For all three z-factor schemes, viscosities peak near the cut-off wavenumber k_c. As for the $M_{t_0} = 0.1$ case, NM and LM provide more viscosity than CM. However, to understand the role played by current and Thornber et al. [9] schemes, it is again pertinent to look at their corresponding dissipation-rate spectra. At lower wavenumbers, dissipation rate for NM is nearly an order of magnitude greater than that for CM and LM, suggesting that NM dissipates even the large energy-containing eddies. In the high-wavenumber end of the spectrum, dissipation rate for

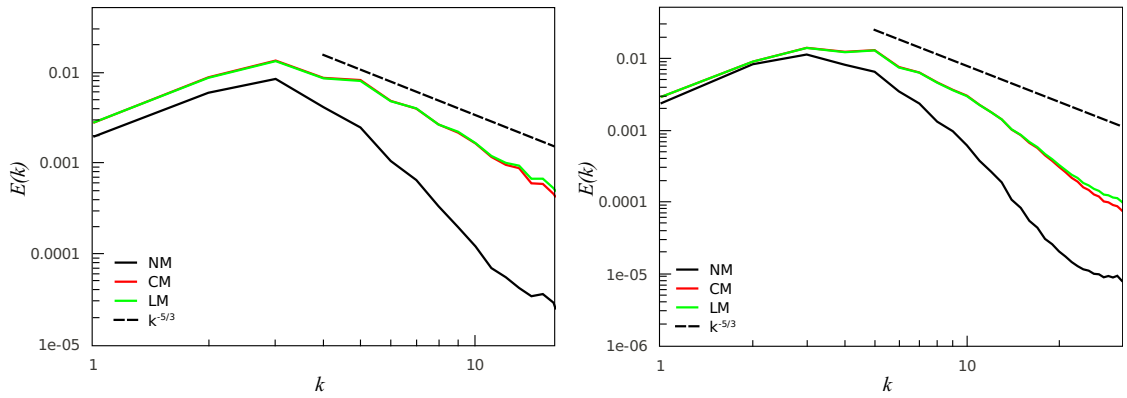

(a) 32^3 (b) 64^3

Figure 4.6: Comparison of energy spectra with Kolmogorov's $-5/3$ slope for NM, CM and LM schemes on (a) 32^3 and (b) 64^3 grids at $t/\tau = 2$.

NM is marginally smaller than the other two, this trend being more pronounced on the 64^3 grid. On both grids, dissipation spectra for current and Thornber et al. [9] schemes peak at wavenumbers lower than k_c, but these wavenumbers are smaller than the corresponding wavenumbers for the $M_{t_0} = 0.1$ case. It is seen on the 64^3 grid that close to $k = k_c$ dissipation for CM and LM drops precipitously, which also explains the greater than $-5/3$ slope of their corresponding energy spectra at higher wavenumbers in Figure 4.6(b).

Figure 4.9 shows the normalized viscosity spectra at $t/\tau = 2$ for the individual governing equations (3.80)-(3.84), obtained using CM on 32^3 grid. Not surprisingly, most of the contribution to the overall viscosity seen in Figure 4.8(a) is from the acoustic modes. The current z-factor scheme (CM) has the effect of considerably reducing these sound-speed-dependent viscosities, and consequently the dissipation rates.

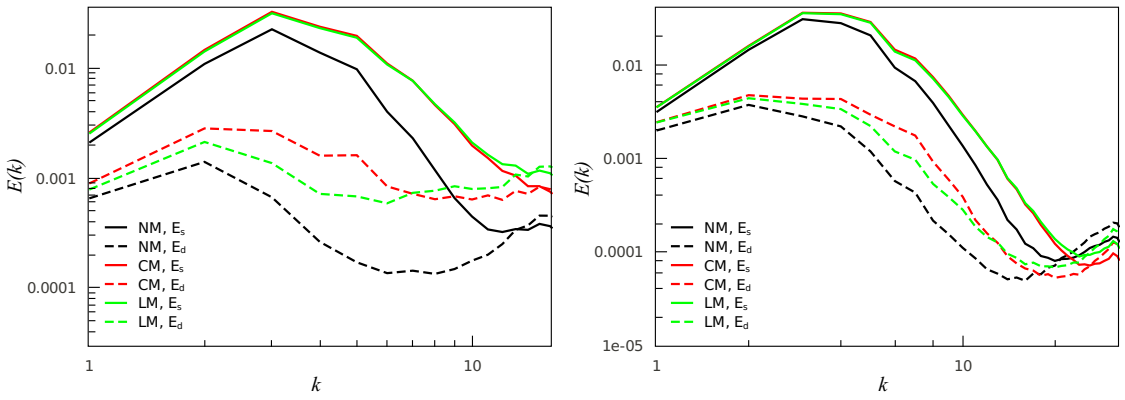

(a) 32^3 (b) 64^3

Figure 4.7: Spectra of dilatational (E_d) and solenoidal (E_s) velocity components for NM, CM and LM schemes on (a) 32^3 and (b) 64^3 grids at $t/\tau = 0.4$.

The iso-surfaces of vorticity magnitude for the two grids and NM and CM schemes are shown in Figure 4.10. On the 32^3 grid with NM, shown in Figure 4.10(a), the high numerical dissipation causes even large-scale structures to be dissipated without undergoing the normal eddy turnover process associated with the turbulent energy cascade. On the same grid, CM shows a somewhat better developed turbulent field, as can be seen in Figure 4.10(b). Figure 4.10(c) and (d) show vorticity contours for the same schemes on the 64^3 grid. The current scheme evidently captures more small-scale vortical structures compared to NM. Some of the vortex tubes in Figure 4.10(d) are rod-like, which is an indication of high vorticity in these regions, whereas some structures are ribbon-shaped, which are associated with high shear. It is expected that dissipation in highly vortical regions is greater than that in shear-dominated regions [20]. Temporal evolution of normalized turbulent kinetic energy (K), enstrophy (Ω) and dissipation rates (ϵ) are plotted in Figure 4.11. DNS data of K [10] for

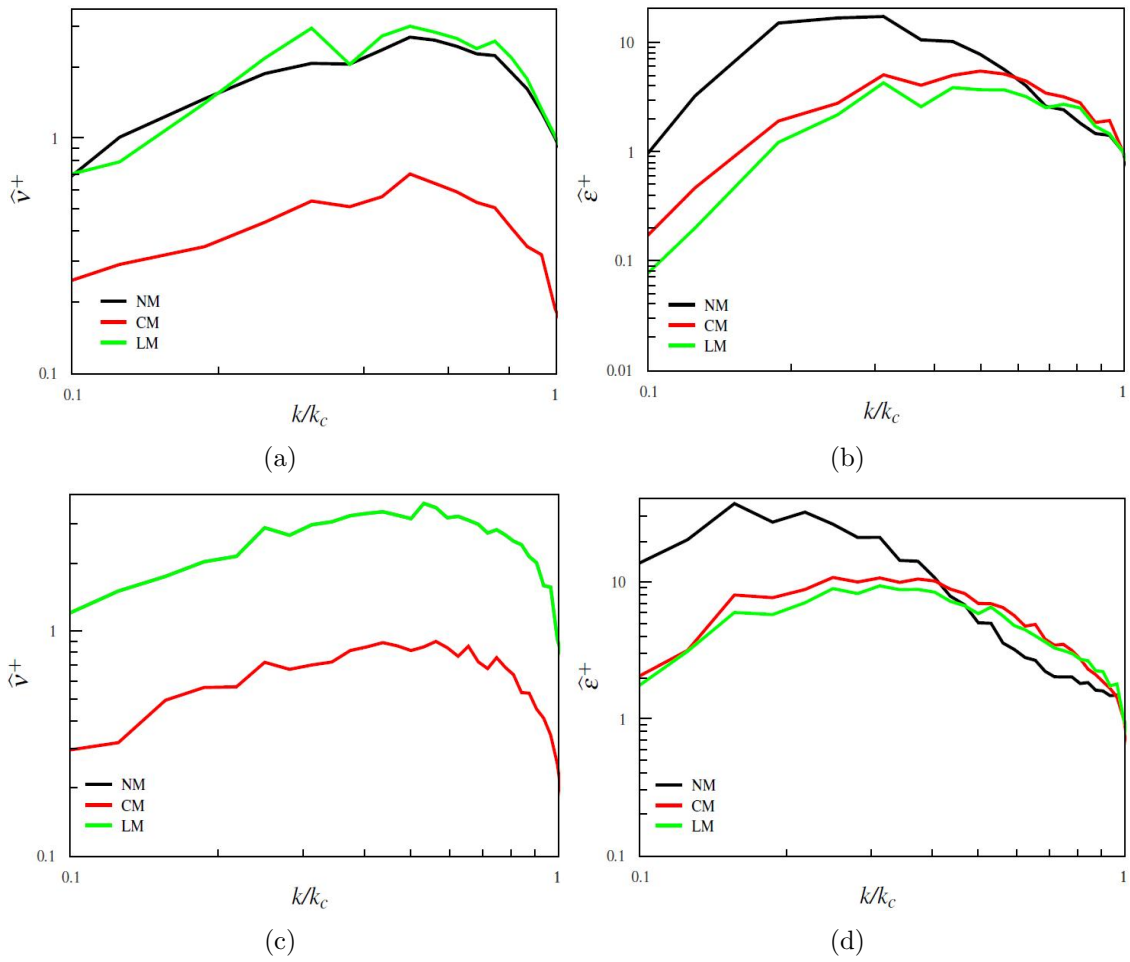

Figure 4.8: Spectra of normalized numerical viscosities (a,c) and dissipation rates (b,d) for NM, CM and LM on 32^3 (top) and 64^3 (bottom) mesh resolutions at $t/\tau = 2$.

the same initial turbulent Mach number M_{t_0} and initial Taylor microscale Reynolds number $Re_{\lambda_0} = 30$ are also presented in Figure 4.11(a). The NM scheme on both grids shows poor comparison with DNS data. The current and Thornber et al. [9] profiles on 32^3 grid are nearly identical. They show reasonably good agreement with the DNS data, particularly at longer simulation times. Moreover, on 64^3 grid, the schemes preserve more energy than DNS data, suggesting an effectively higher Re_{λ_0} simulation compared to the DNS [10]. The enstrophy curves for NM on both grids,

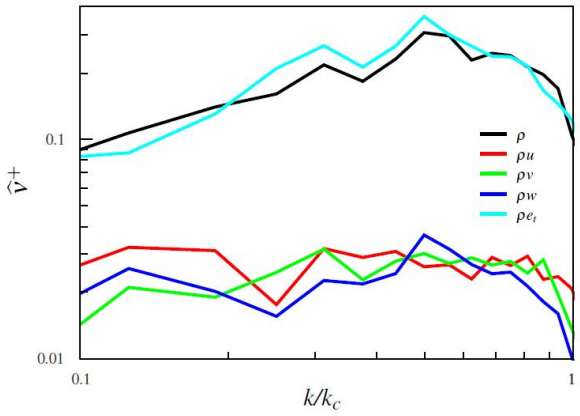

Figure 4.9: Spectra of normalized numerical viscosities for each of the governing equations, Equation 3.80-Equation 3.84 obtained using the CM scheme on 32^3 grid at $t/\tau = 2$.

and for CM and LM on 32^3 grid do not show the peak that has been observed in prior DNS and LES studies. Indeed, the peak in enstrophy is only seen for current and Thornber et al. [9] schemes on the finer 64^3 grid. The absence of peak in enstrophy is an indicator of significiant diffusion taking place in the early stages of flow development, thereby affecting the formation of small-scale structures [30, 32]. The CM and LM schemes on the 64^3 mesh show two stages in the evolution of enstrophy Ω. The first stage corresponds to the development of a turbulent flow field characterized by the formation of vortex tubes or worm-like structures. Once the turbulent flow field is fully developed and the higher wavenumber modes of the energy spectra are populated, numerical damping becomes significant enough to reduce the kinetic energy, leading to a sharp drop in Ω. This is evident in the dissipation-rate evolution plotted in Figure 4.11(c). It is seen that ϵ profiles of both current and Thornber et

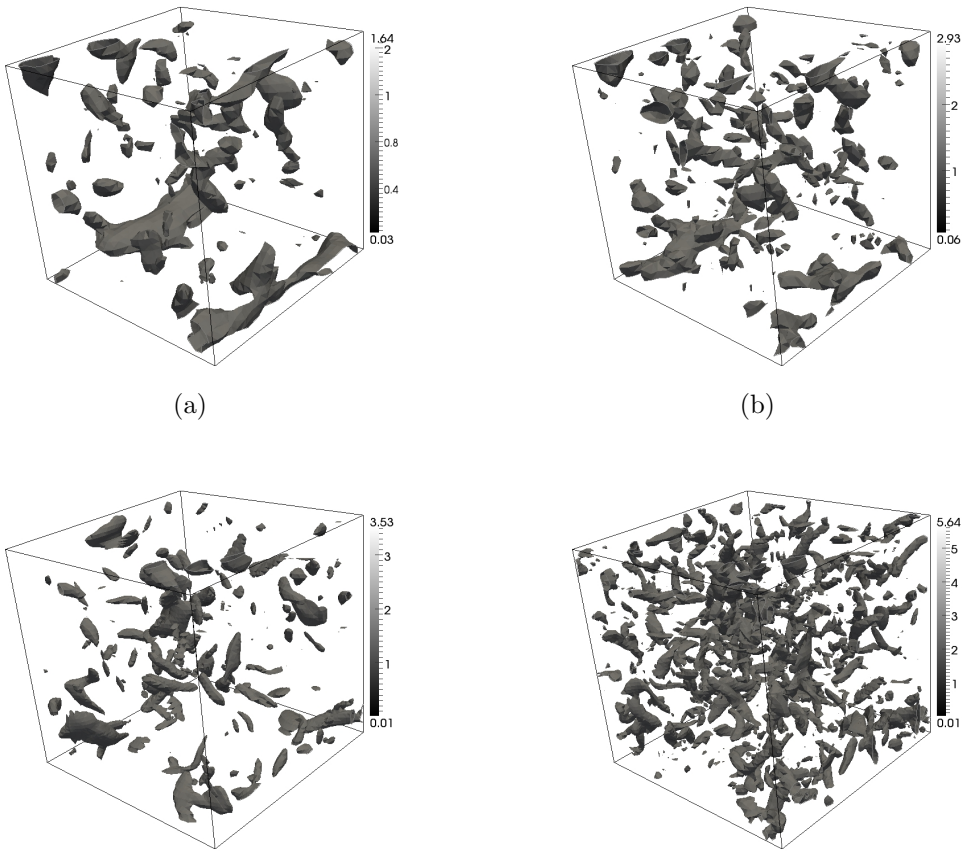

(a) (b)

Figure 4.10: Iso-vorticity surfaces for (a) NM and (b) CM on 32^3 grid, and (c) NM and (d) CM on 64^3 grid at $t/\tau = 2$.

al. [9] modifications remain essentially flat till $t/\tau \approx 1$ before experiencing a steady decline.

Motivated by the relationship between kinetic energy dissipation rate ($-dK/dt$) and enstrophy (Ω) in incompressible isotropic turbulence, one may consider the following equation to be approximately applicable for weakly compressible decaying isotropic turbulence as well.

$$\frac{dK}{dt} = -2\nu\Omega \tag{4.24}$$

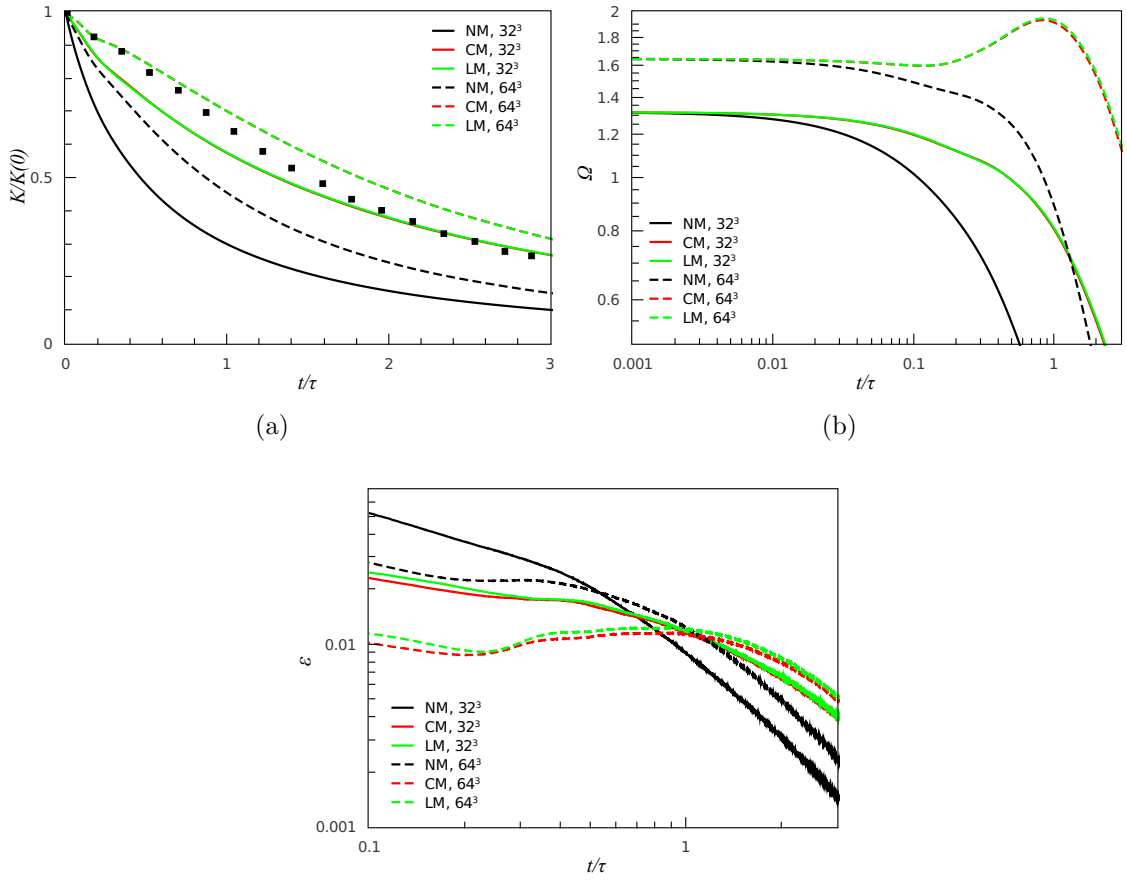

Figure 4.11: Comparison of profiles of (a) normalized turbulent kinetic energy (b) enstrophy (c) effective numerical viscosity and (d) numerical dissipation rate with time for NM, CM and LM schemes on 32^3 and 64^3 mesh resolutions. The symbols in (a) correspond to de-aliased spectral computation of Honein and Moin [10].

For inviscid ILES simulations, Drikakis et al. [100] reasoned that an estimate for numerical viscosity (or effective Reynolds number) could be obtained by replacing ν with ν_{eff} in (4.24). Figure 4.12 shows the temporal development of ν_{eff} for all three modifications on both 32^3 and 64^3 grid resolutions. As expected, increasing the grid resolution has the effect of reducing the viscosity which consequently results in greater enstrophy production for all three modifications. Moreover, all schemes with the exception of NM on 32^3 grid exhibit a noticeable hump in the early stages

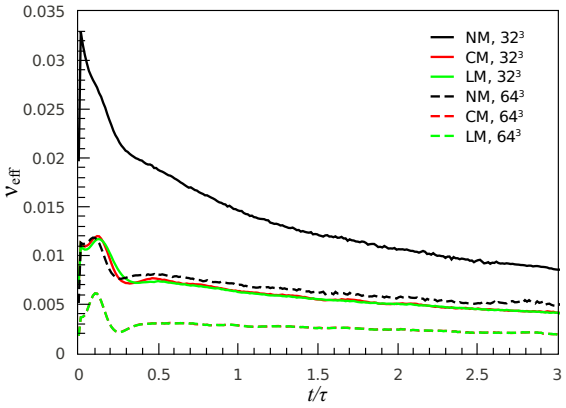

Figure 4.12: Time evolution of numerical viscosity in equation Equation 4.24 for NM, CM and LM schemes on 32^3 and 64^3 mesh resolutions.

of flow development (close to $t \sim 0.1$). The amplitude of the hump is maximum for the modified schemes (CM and LM) on the 64^3 grid. This is a reflection of the fact that for these two cases, enstrophy does not change appreciably during the initial times (see Figure 4.11(b)). Consequently, the increase in viscosity is entirely due to the increase in $-dK/dt$. While the plot yields useful information on numerical viscosities inherent to the various schemes, it is to be noted that ν_{eff} provides a single global value for the entire domain, whereas ν_{num} derived in this study provides spatial variation also, which enables us to obtain insights in the wavenumber space.

Table 4.1: Skewness (S_3), Flatness (S_4), and mean kinetic energy decay exponent (p)

	32^3			64^3		
	NM	CM	LM	NM	CM	LM
S_3	-0.41	-0.43	-0.43	-0.16	-0.23	-0.25
S_4	5.48	4.22	4.21	3.81	4.33	4.73
p	2.95	1.80	1.80	2.23	1.24	1.24

The values of skewness, flatness and the decay exponent p of mean kinetic energy are presented in Table 4.1 for all three schemes on both grids. The exponent p controls the decay of resolved kinetic energy in isotropic turbulence and is given by the following well known expression [59]:

$$K = A(t - t_0)^{-p} \tag{4.25}$$

Here A is a proportionality constant, and t_0 is the time when K begins to decay. In the present study, t_0 is chosen to be zero. Kolmogorov's theory predicts the decay exponent to be 10/7 for high Re_λ flows, whereas Saffman's analysis [101] determined the value to be 6/5. Experimental measurements have found p to lie in the range 1.2-1.4, while some numerical studies have reported $p = 2$. It is seen from Table 4.1 that the magnitude of skewness on the 32^3 grid for all three falls within the range expected for homogeneous isotropic turbulence. However, the decay exponent p for NM is unrealistically high. CM and LM result in significantly reduced values of p that are nevertheless different from the values predicted by theory.

It may also be noticed from Table 4.1 that the magnitudes of skewness on the 64^3 grid are smaller than those for the 32^3 grid, as well as lower than prior experimental or DNS data. However, the exponent p for the modified schemes are close to the value predicted by Saffman's theory. The variation in flatness, S_4, with grid resolution is smaller than that for skewness. Flatness values, are in general, found to be in a realistic range. A 128^3 grid simulation was also conducted with CM, yielding

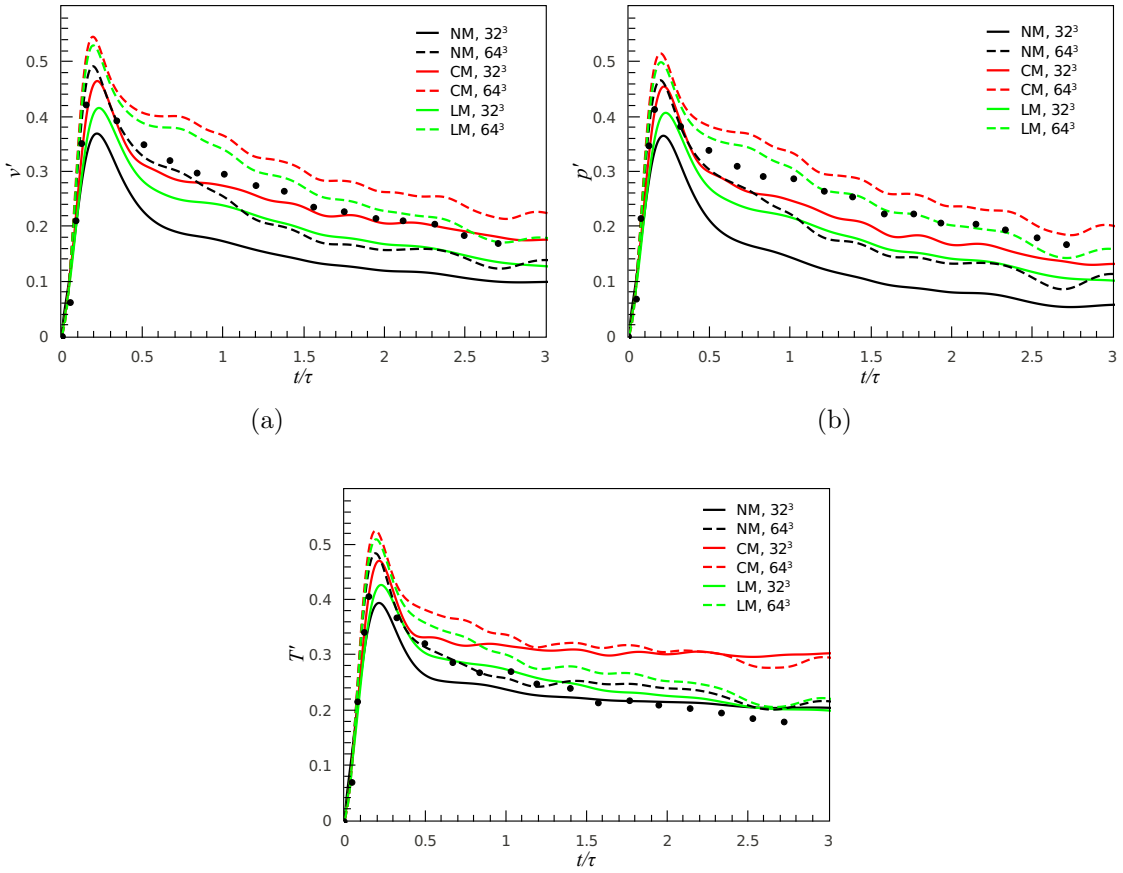

Figure 4.13: Temporal evolution of RMS values of (a) specific volume (v'), (b) pressure (p') and (c) temperature (T') on 32^3 and 64^3 grids. The symbols correspond to de-aliased spectral computation of Honein and Moin [10].

steady-state skewness and flatness parameters of -0.35 and 3.97, respectively. These values are in excellent agreement with Kang et al. [11] experimental data.

The RMS fluctuations in specific volume v', pressure p' and temperature T' are presented in Figure 4.13, along with the corresponding DNS data from [10]. For all schemes, at the time $t/\tau \approx 0.2$, the profiles of v', p' and T' attain a maximum indicating that the flow has attained maximum compressibility. Since the peak RMS fluctuations are the largest for CM on 64^3 mesh, flow is most compressible for this

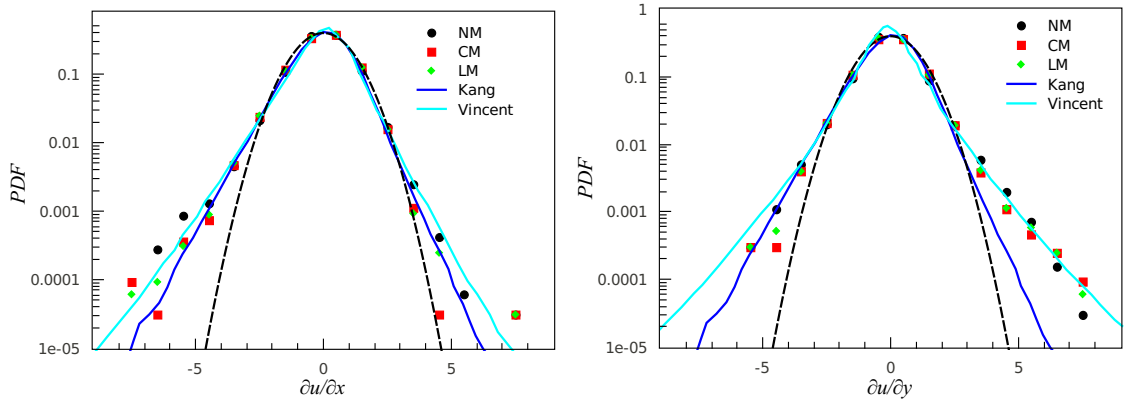

(a) 32^3

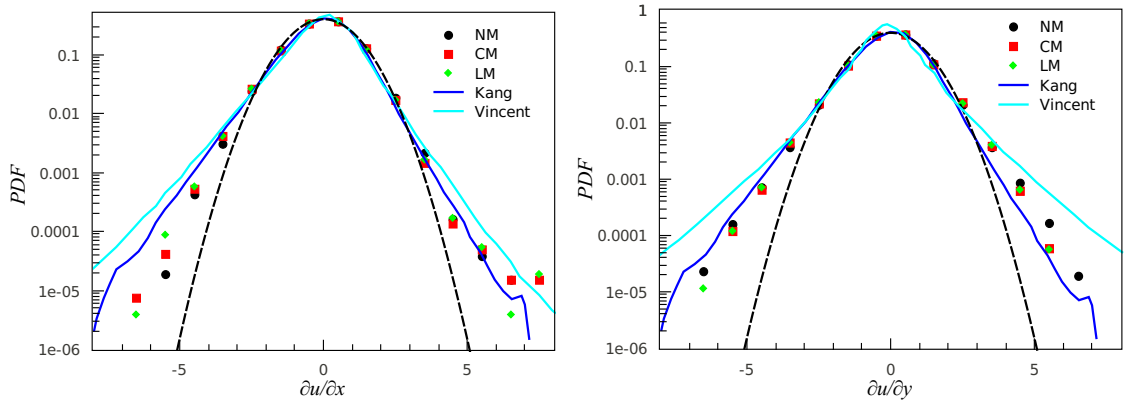

(b) 64^3

Figure 4.14: Probability density functions (PDFs) of the velocity derivatives normalized with their respective RMS values for the three schemes along with experimental data of Kang et al. [11] and DNS of Vincent and Meneguzzi [12] on (a) 32^3 and (b) 64^3 grids at $t/\tau = 2$.

case with strong anisotropic events. On the 64^3 mesh, the rates of decay of all three fluctuations are the smallest for CM. It is also seen in Figure 4.13(c) that T' decays at a slower rate than the DNS data.

Figure 4.14 presents the PDFs of velocity derivatives $\partial u/\partial x$ and $\partial u/\partial y$ normalized by their respective RMS values. PDFs are shown for all three schemes on 32^3 and 64^3 meshes at $t/\tau = 2$. Also shown are the corresponding PDFs from the

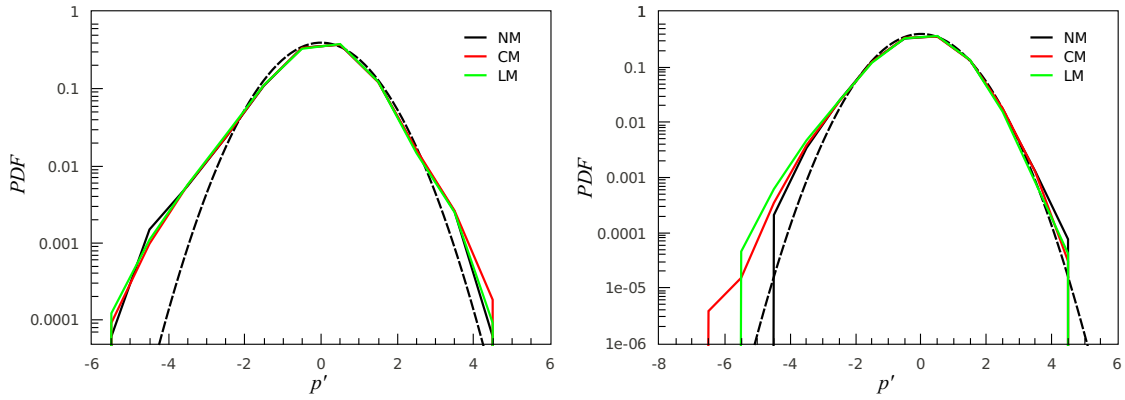

(a) 32^3 (b) 64^3

Figure 4.15: PDFs of pressure fluctuations (p') for NM, CM and LM schemes on (a) 32^3 and (b) 64^3 grids at $t/\tau = 2$.

Kang et al. experiments [11] at $Re_\lambda = 626$, and Vincent and Meneguzzi DNS [12] at $Re_\lambda = 150$. It is evident that all schemes capture the non-Gaussian nature of velocity derivatives. Further, for higher magnitudes of velocity derivatives, the PDFs are tending toward an exponential behavior. The exponential nature of PDFs is indicative of a scheme's ability to capture the inertial-scale energy-transferring eddies that are directly linked to intermittency. For both grid resolutions, NM generally captures smaller magnitudes of velocity derivatives when compared to CM and LM, suggesting that NM does not perform as well as the other two schemes in accounting for the rare, high-velocity-gradient fluid events.

The PDFs of pressure fluctuations p' are shown in Figure 4.15. On the coarser mesh, PDFs for all three schemes have a negative skewness, and are close to one another. The trends are broadly similar for the 64^3 grid as well, except that the CM and LM schemes capture negative pressure fluctuations of higher magnitude when

compared to NM, i.e. PDFs for CM and LM have higher skewness than for NM. This suggests that CM and LM perform better than NM in predicting the correlation between pressure and vorticity arising from turbulent intermittency. Further, the comparatively smaller skewness of the NM scheme signifies a higher degree of dissipation and consequently a greater decorrelation of pressure from vorticity [30, 59]. Clearly, minimizing numerical viscosity has the greatest impact on restoring the pressure-vorticity coupling that is observed in DNS studies of isotropic turbulence [20]. It is evident from the results presented in this section that both current and Thornber et al. [9] z-factor modifications are capable of successfully capturing the physics of decaying isotropic turbulence.

4.5.3 Non-Linear Subsonic Regime: $M_{t_0} = 0.5$

As discussed previously, temporal evolution of the turbulent flow field in this regime is characterized by significant compressibility effects. This section addresses the physics of shocket development, as well as the statistics associated with such a flow field in the context of ILES using the Roe-MUSCL flux formulation.

The energy spectra for the modified schemes on 32^3 and 64^3 grids at $t/\tau = 2$ are shown in Figure 4.16(a). These spectra are similar to those observed for the $M_t = 0.3$ case (Figure 4.6). Not suprisingly, the spectra for the 64^3 grid contain a broader wavenumber range of the inertial scales of turbulence. However, even with the finer mesh, the spectra exhibit noticeable deviation from the $-5/3$ slope at the high wavenumber end. The dilatational and solenoidal spectra on 64^3 grid at $t/\tau = 0.48$ are shown in Figure 4.16(b) for the CM scheme. The difference in the energy content

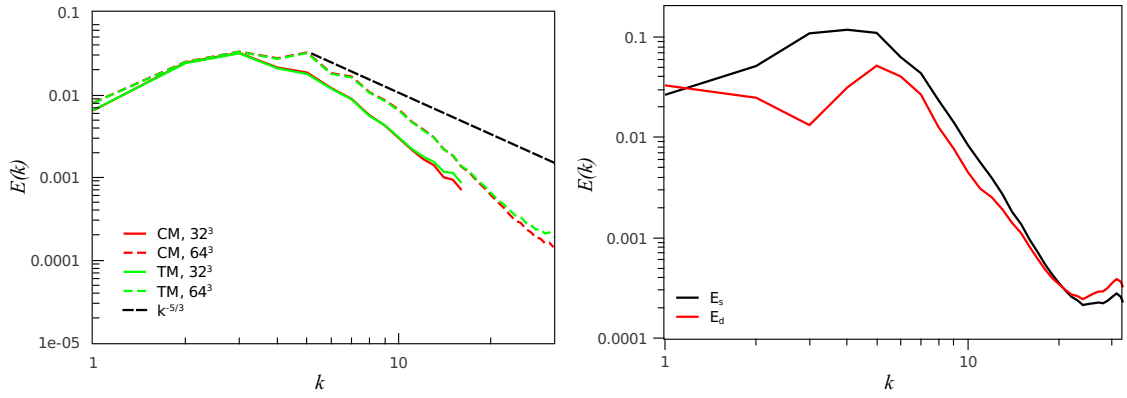

(a) 32^3 (b) 64^3

Figure 4.16: Energy spectra of (a) CM and LM schemes on 32^3 and 64^3 grid resolutions at $t/\tau = 2$ and (b) dilatational and solenoidal velocities for CM on 64^3 grid at $t/\tau = 0.48$.

between the two spectra is smaller as compared to the corresponding profiles for the $M_t = 0.3$ case (Figure 4.7). This is primarily due to the greater amount of dilatational energy present in the flow field, arising from the increased compressibility effects at higher Mach numbers. The spectra of numerical viscosity and dissipation rate display similar trends as those for $M_t = 0.3$, and are not shown.

Figure 4.17 presents the RMS of dilatation fluctuations (θ'), turbulent kinetic energy (K), enstrophy (Ω), and dissipation rate (ϵ) as a function of time. In Figure 4.17(a), it can be seen that dilatation evolves from an initial value corresponding to a random, weakly compressible field, and increases rapidly during the *acoustic transient* regime corresponding to the simulation time: $0 < t/\tau < 0.16$. The flow then evolves into the *convective time-scale* regime during which time non-linear interactions begin to take place between the dilatational and solenoidal modes. For all schemes, on the 32^3 and 64^3 grids, the non-linear interactions are too weak to produce

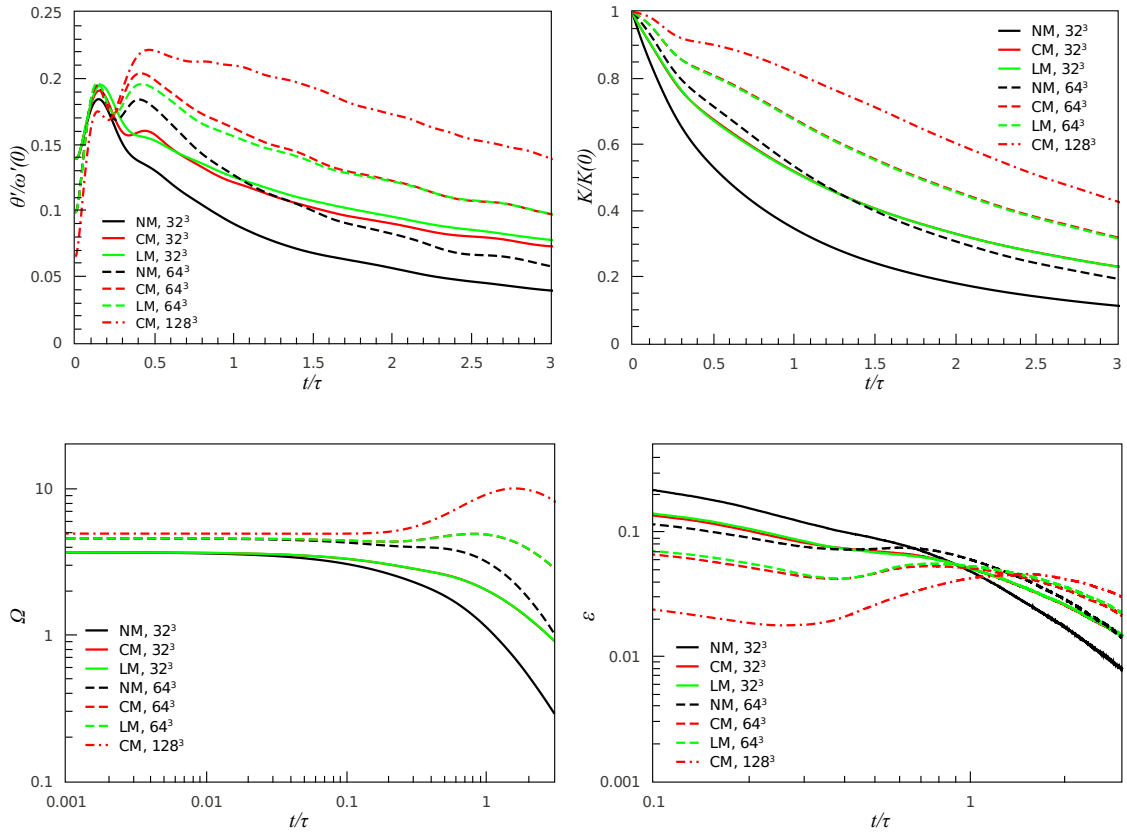

Figure 4.17: Temporal evolution of (a) normalized RMS of velocity divergence, (b) normalized turbulent kinetic energy, (c) enstrophy and (d) numerical dissipation rate with time for NM, CM and LM schemes on 32^3 and 64^3 mesh resolutions. Results of NM scheme on 128^3 grid are also presented.

the conditions necessary for shocklet formation. Specifically, both NM and LM profiles fail to display any secondary peak on the 32^3 mesh which is an indication of their highly diffusive nature. On the 64^3 mesh, all three schemes display a secondary peak, with the CM profile being the only one to develop a higher secondary peak than the primary one. But, even for CM on 64^3 mesh, the secondary peak is not high enough for shocklet formation. Large eddy simulations (LES) employing explicit subgrid-

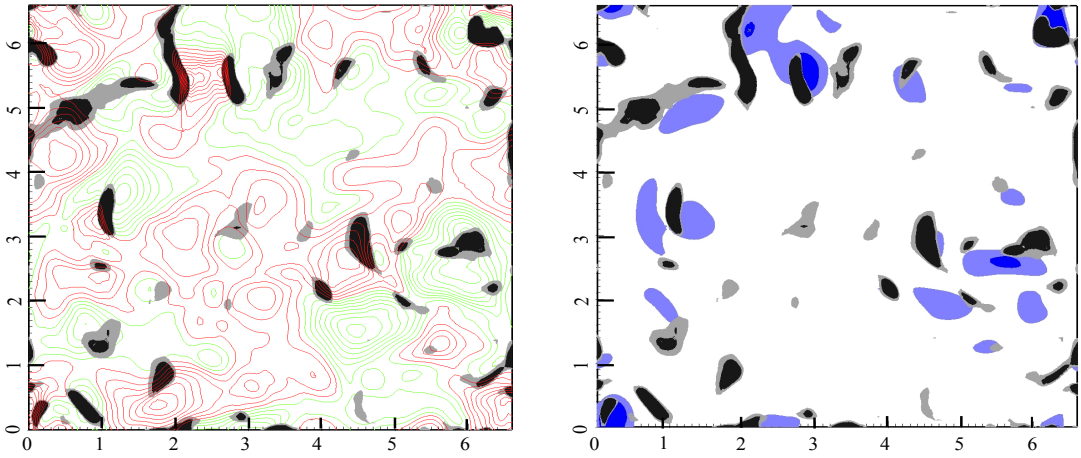

Figure 4.18: Contours of (a) density and (b) local Mach number superimposed on contours of dilatation at $t/\tau = 0.43$ for 128^3 grid and CM scheme. The green and red contours in (a) correspond to negative and positive density fluctuations, while the dark and light blue regions in (b) indicate supersonic and subsonic regions, respectively. The grey and black contours in both figures are regions where $\theta < -\theta'$.

scale models too have been unsuccessful in capturing shocklets since their thicknesses are of order of the Kolmogorov length scales [94], which are unresolved in LES.

In Figure 4.17(b) and (c), the K and Ω profiles for all three schemes on the coarser 32^3 and 64^3 grids display trends similar to those reported for the $M_t = 0.3$ case. As expected, the 128^3 mesh case dissipates the least amount of kinetic energy, and also exhibits the highest enstrophy peak toward the end of the simulation. The dissipation rates corresponding to CM and LM on 64^3 and 128^3 grids (Figure 4.17(d)) increase for a certain time period, with the finer grid giving rise to higher values after $t/\tau = 2$ due to the relatively stronger non-linear interactions and to the rise in the compressibility of the flow field.

Motivated by the above trends, simulation on a 128^3 mesh was conducted using CM scheme. It is clear from Figure 4.17(a) that for this simulation, the secondary peak in θ' is the highest among all the cases considered, and is also substantially greater than the primary peak. As a result, it is conjectured that the non-linear interactions between the dilatational and solenoidal modes are strong enough to develop shocklets. To establish this conjecture, we present in Figure 4.18 the contours of density and local Mach number on a 2-D plane of the domain at $t/\tau = 0.43$. These contours are in turn superimposed on the contours of dilatation. The flow field at this time is highly compressed with the minimum dilatation $\theta_{\min} = -13.7$ and RMS dilatation $\theta' = 0.7$. In Figure 4.18(a), the regions of large negative dilatation are indicated in black. It may be noticed that in the vicinity of these regions, flow density increases rapidly, which is indicative of the flow decelerating from supersonic to subsonic velocities across shocklets. The presence of shocklets may be explicitly seen in Figure 4.18(b), where one notices regions of supersonic to subsonic transition.

Finally, skewness and flatness are provided in Table 4.2 for the 32^3 and 64^3 simulations. On both grids, it is seen that CM and LM give rise to higher skewness than NM. For flatness as well, we see that the values for the modifications are marginally higher than those for NM. The decay exponent p is unrealistically high for NM, but attains expected values for CM and LM. As expected, S_3 reduces to -0.35 with an increase in the grid resolution to 128^3 but S_4 remains unchanged.

Table 4.2: Skewness (S_3), Flatness (S_4), and mean kinetic energy decay exponent (p)

	32^3			64^3		
	NM	CM	LM	NM	CM	LM
S_3	-0.27	-0.36	-0.34	-0.14	-0.23	-0.25
S_4	4.00	4.03	4.19	3.57	3.85	3.89
p	2.95	2.10	2.10	2.00	1.30	1.30

CHAPTER 5

TAYLOR-GREEN VORTEX

5.1 Introduction

Application of shock-capturing methods for implicit large-eddy simulation (ILES) of fully turbulent, as well as transitional flows is a topic of current research interest. As discussed previously, according to Drikakis et al. [26], in order for a scheme to be suitable for ILES, it must capture: (i) the $-5/3$ slope of the energy spectrum in the inertial subrange, and (ii) the instabilities driving laminar to turbulent flow transition. The previous chapter focused on the first criterion by examining the numerical viscosities and dissipation rates of TVD-MUSCL schemes for ILES of nearly incompressible and weakly compressible isotropic turbulent flows. The current chapter principally concerns the second criterion through a study of the stability and dissipation of second-order Roe-MUSCL scheme when implemented in conjunction with various Runge-Kutta-based temporal schemes. In this regard, the Taylor-Green vortex problem is ideally suited since it is characterized by laminar, transitional, as well as turbulent flow regimes during various times of the simulation.

Numerical simulation of an initially stable laminar flow-field transitioning to a fully developed non-linear turbulent motion is regarded as one of the most challenging

problems confronting current numerical schemes. A fundamental requirement for such problems is that algorithms must not dissipate turbulent kinetic energy in the early stages of the simulation so as to allow for growth of perturbations in the flow field. These fluctuations then trigger the vortex stretching mechanism which is cited as the primary cause of transition to turbulence [13]. Furthermore, in order for the subsequent turbulent motion to be considered well developed, there should be proper scale separation between the integral and dissipative eddies [14]. Arguably, an ideal test case for studying transition to turbulence is the three-dimensional (3-D) Taylor-Green vortex (TGV) system introduced by Taylor and Green [24]. It is a fundamental canonical problem that provides critical insights into the physics of vortex stretching and the subsequent production of dissipative eddies [100].

Direct numerical simulations (DNS) of TGV were performed by a number of authors, notable among which are those of Brachet et al. [13], Brachet [14], and more recently of Shu et al. [16]. Brachet et al. [13] conducted de-aliased pseudo-spectral simulations of both inviscid and viscous TGV on 32^3, 64^3, 128^3 and 256^3 grids. The inviscid spectral runs were, however, limited to very early times due to the absence of a damping mechanism for stabilizing the growth of perturbations. Subsequently, Brachet [14] repeated the numerical experiment on a 864^3 grid. Both studies [13, 14] exploited the inherent symmetries of TGV to achieve a Reynolds number (Re) in excess of 3000. Shu et al. [16] conducted inviscid TGV simulations using fifth-order WENO finite difference, as well as Fourier collocation spectral methods. To suppress non-linear instabilities in spectral simulations, Shu et al. considered low pass filters such as the exponential filter and sharp-cutoff filter.

As discussed previously, due to the prohibitively high computational cost of DNS for realistic, high-Reynolds-number turbulent flows [26], large-eddy simulations (LES) have emerged as a promising, computationally feasible alternative. A number of LES-SGS models have been explored for transitional flows, with mixed success. For instance, in the simulation of TGV, Hickel et al. [102] found eddy viscosity models such as the standard Smagorinsky model (SSM) [28] and the structure-function model of Metais and Lesieur [103] to be unsuitable due to excessive dampening of flow perturbations. However, they observed significant improvements in flow structure when using the dynamic Smagorinsky model (DSM) [29], since DSM preserves TKE better than SSM during the initial times.

An interesting alternative to LES, discussed extensively in Chapter 4, is the implicit large-eddy simulation (ILES) technique. This approach seems well suited for transitional flows containing adjacent regions of very high and very low Reynolds numbers [100]. Currently, ILES approaches also include a broad family of schemes based on Godunov's Riemann solver [34].

It is well known [30] that Godunov-based schemes are highly dissipative for turbulent flows. To address this problem, Thornber et al. [9] suggested an approach that involved reducing the artificially large velocity jumps Δu set up by these schemes, since the dissipation rate is $\propto O(\Delta u^2)$. An alternative approach to improve the accuracy of Godunov-based schemes was recently proposed by Bidadi and Rani [64] (see Chapter 3). In that study, a Mach-number-dependent scaling factor was used to mitigate excessive dissipation by reducing numerical viscosity instead of velocity jumps.

In this chapter, the stability and diffusive characteristics of the modified [9,64] second-order Roe-MUSCL scheme together with three temporal schemes are investigated for implicit large-eddy simulation (ILES) of the Taylor-Green vortex problem. The three temporal schemes considered are those of Jameson et al. [15], Shu and Osher [104], and Spiteri and Ruuth [17]. Simulations are conducted on 64^3 and 128^3 grids. Our objective is to examine whether the spatial-temporal scheme combinations meet the criteria outlined by Drikakis et al. [26], with the focus being on capturing transition. Specifically, we investigate whether these schemes accurately capture the laminar, transition and turbulent stages of the TGV flow. To this end, a number of statistical quantities are computed, and compared with DNS and theoretical scaling wherever appropriate. The spectral profiles of quantified numerical viscosity and dissipation rate are also computed, which shed significant light on the accuracy and stability of the schemes. Estimates for the effective Reynolds number Re_{eff} for various cases are obtained by using the correlation between mean dissipation rate and enstrophy.

5.2 Initial Conditions for Inviscid TGV

The 3-D compressible Euler equations in conservative form are solved [64]. The ideal-gas equation of state closes the system of equations. Simulations are conducted in a triply periodic cube with edge length $L \approx 2\pi$, and the domain is initialized with

the following solenoidal velocity field,

$$u_0 = U \sin(kx)\cos(ky)\cos(kz) \tag{5.1}$$

$$v_0 = -U \cos(kx)\sin(ky)\cos(kz) \tag{5.2}$$

$$w_0 = 0 \tag{5.3}$$

where k is the wavenumber, and velocity U is a free parameter. The initial pressure field p_0 is a solution to the Poisson equation, and is given by

$$p_0 = p_\infty + \frac{\rho U^2}{16}\left[2 + \cos(2kz)\right]\left[\cos(2kx) + \cos(2ky)\right] \tag{5.4}$$

The initial values chosen for the above variables were obtained from the references [31, 100]. They are $k = 1$, $U = 100$ m/s, $p_\infty = 100000$ Pa, $\rho = 1.178$ kg/m^3 and $\gamma = 1.4$. The resulting initial Mach number is $M_0 = 0.29$.

5.3 Numerical method

This section presents an overview of the numerical method that has been presented in much greater detail in Chapter 4. Applying the finite volume method (FVM) to the Euler equations yields the following semi-discretized form of equations:

$$\frac{d\mathbf{Q}(t)}{dt} V + \sum_{f \in \text{cell faces}} (\mathbf{F}_Q \cdot \mathbf{n})_f \; A_f = 0 \tag{5.5}$$

where $\mathbf{Q} = [\rho\ \rho u\ \rho v\ \rho w\ \rho e_t]^T$ is the vector of conserved variables, V is the cell volume, A_f is the interface surface area, and the face-normal flux $(\mathbf{F}_Q \cdot \mathbf{n})_f$ is given by

$$
\begin{aligned}
(\mathbf{F}_Q \cdot \mathbf{n})_f &= (\mathbf{F}\hat{\mathbf{e}}_x + \mathbf{G}\hat{\mathbf{e}}_y + \mathbf{H}\hat{\mathbf{e}}_z)_f \cdot (n_x\hat{\mathbf{e}}_x + n_y\hat{\mathbf{e}}_y + n_z\hat{\mathbf{e}}_z)_f && (5.6)\\
&= (\mathbf{F}n_x + \mathbf{G}n_y + \mathbf{H}n_z)_f && (5.7)
\end{aligned}
$$

The x, y and z components of flux, $\mathbf{F}$, $\mathbf{G}$ and $\mathbf{H}$ respectively, are discretized using Roe's flux-difference splitting technique [40]. Substituting Roe's expression into (5.7) for the three fluxes yields

$$
(\mathbf{F}_Q \cdot \mathbf{n})_f = \mathbf{F}_{\text{CDS}} - \frac{1}{2}|\tilde{\mathbf{A}}_n|(\mathbf{Q}_R - \mathbf{Q}_L) \tag{5.8}
$$

where $\mathbf{Q}_L$ and $\mathbf{Q}_R$ are the reconstructed states of $\mathbf{Q}$ to the left and right of a cell interface, and the dispersive second-order central differenced flux, $\mathbf{F}_{\text{CDS}}$, is given by:

$$
\begin{aligned}
\mathbf{F}_{\text{CDS}} = &\frac{1}{2}\left[\mathbf{F}(\mathbf{Q}_L) + \mathbf{F}(\mathbf{Q}_R)\right] n_x + \frac{1}{2}\left[(\mathbf{G}(\mathbf{Q}_L) + \mathbf{G}(\mathbf{Q}_R)\right] n_y + \\
&\frac{1}{2}\left[\mathbf{H}(\mathbf{Q}_L) + \mathbf{H}(\mathbf{Q}_R)\right] n_z
\end{aligned} \tag{5.9}
$$

The approach to compute the Roe-averaged Jacobian $|\tilde{\mathbf{A}}_n|$ was elaborated in the previous chapter, and is not reproduced here. The time derivative term in (5.5) is discretized using the third-order Runge-Kutta schemes of Jameson et al. [15], Shu-Osher [104], and Spiteri-Ruuth [17], as shown in Table 5.1. Both Shu-Osher and Spiteri-Ruuth schemes are referred to as TVD Runge-Kutta [105]. The latter has the

advantage of being theoretically stable up to CFL = 2. It may be seen from Table 5.1 that the Jameson et al. scheme is perhaps the most explicit among the three methods in the sense that the intermediate solutions are given the lowest weightage in this scheme.

Table 5.1: Three steps for third-order Runge-Kutta methods of Jameson et al. [15], Shu-Osher [16] and Spiteri-Ruuth [17].

	Jameson et al.	Shu-Osher	Spiteri-Ruuth
$\mathbf{Q}^{(1)}$	$\mathbf{Q}^n - \frac{1}{3}\frac{\Delta t}{V}\mathbf{R}^n$	$\mathbf{Q}^n - \frac{\Delta t}{V}\mathbf{R}^{(0)}$	$\mathbf{Q}^n - \frac{1}{2}\frac{\Delta t}{V}\mathbf{R}^n$
$\mathbf{Q}^{(2)}$	$\mathbf{Q}^n - \frac{1}{2}\frac{\Delta t}{V}\mathbf{R}^{(1)}$	$\frac{3}{4}\mathbf{Q}^n + \frac{1}{4}\mathbf{Q}^{(1)} - \frac{1}{4}\frac{\Delta t}{V}\mathbf{R}^{(1)}$	$\mathbf{Q}^n - \frac{1}{2}\frac{\Delta t}{V}\mathbf{R}^{(1)}$
$\mathbf{Q}^{n+1}$	$\mathbf{Q}^n - \frac{\Delta t}{V}\mathbf{R}^{(2)}$	$\frac{1}{3}\mathbf{Q}^n + \frac{2}{3}\mathbf{Q}^{(2)} - \frac{2}{3}\frac{\Delta t}{V}\mathbf{R}^{(2)}$	$\frac{2}{3}\mathbf{Q}^{(2)} + \frac{1}{3}\mathbf{Q}^n - \frac{1}{3}\frac{\Delta t}{V}\left[\mathbf{R}^{(2)} + \mathbf{R}^{(1)}\right]$

While ILES has been applied to a wide variety of flows of both practical and academic interest, the magnitudes of the effective numerical viscosity (ν_{eff}) and Reynolds number (Re_{eff}) due to the numerical schemes are yet to be rigorously quantified [106]. Over the past decade, a number of studies have attempted to estimate ν_{eff} using [106]

$$\nu_{\text{eff}} = \epsilon/\Omega \tag{5.10}$$

where ϵ is the dissipation rate and Ω is the enstrophy (square of the vorticity magnitude). For forced isotropic turbulence, Fureby and Grinstein [107] computed ν_{eff}

as

$$\nu_{\text{eff}} = \epsilon_F / \left[2 \left\langle S_{ij} S_{ij} \right\rangle \right] \tag{5.11}$$

Here ϵ_F is the dissipation due to forcing, S_{ij} is the strain rate tensor, and $\langle \cdots \rangle$ indicates spatial averaging over the entire domain. For the same case, Aspden et al. [108] proposed the following formulation

$$\nu_{\text{eff}} = \epsilon^{1/3} \xi^{4/3} (\Delta x)^{4/3} \tag{5.12}$$

where the dimensionless parameter, $\xi = 0.203 N^{0.102}$, N is the number of grid cells, and Δx is the grid size. In case of incompressible decaying isotropic turbulence, since most of the energy is contained in the resolved scales, it was found to be more appropriate to utilize the relation representing the strong correlation between the resolved rate of change of kinetic energy and enstrophy [100, 106, 108]:

$$\frac{dK^*(t)}{dt^*} = -\frac{\Omega^*}{Re} \tag{5.13}$$

where $K^* = 1/2 \left\langle u_i u_i \right\rangle / U_0^2$ and $\Omega^* = \left\langle \omega^2 \right\rangle / (kU_0)^2$ are dimensionless kinetic energy and enstrophy, respectively. Using the above relation, resonable estimates of Re_{eff} were obtained by Zhou et al. [106] for the TGV case after the flow had fully transitioned to turbulence. Latini et al. [109] provided alternative means to estimate the effective numerical viscosity and Reynolds number for WENO-based ILES simulations of the 2-D single-mode Richtmyer-Meshkov instability. In that study, the numerical viscosity was estimated using both the dissipation rate of turbulent ki-

netic energy and of enstrophy. The effective Reynolds number was also computed using two expressions, one used in blast wave simulations and the other in two-mode Richtmyer-Meshkov instability simulations.

In the study by Bidadi and Rani [64] (see Chapter 3), a new formulation was derived for numerical viscosity ν_{num} inherent to the Roe-MUSCL scheme. It is to be noted that ν_{num} represents the actual numerical viscosity, whereas ν_{eff} is only an *a posteriori* indirect estimate. The numerical viscosity matrix for the Euler system of equations was derived as [64]

$$\boldsymbol{\nu}_{\text{num}} = \frac{z}{2}\left(\mathbf{I} - \frac{\boldsymbol{\Psi}}{\Lambda}\right)|H(\tilde{\mathbf{A}}_n)|\ (\mathbf{d}\cdot\mathbf{n})_f \tag{5.14}$$

where $z = \min[1, \max(M_L, M_R)]$ is a Mach-number-dependent modification used to mitigate dissipation, H represents Harten's correction, $\mathbf{d}$ is the vector from the left centroid to the right centroid at an interface, $\mathbf{n}$ is the face-normal vector, Λ is a scaling parameter [64], and $\boldsymbol{\Psi}$ is the diagonal matrix of flux limiters for the conserved quantities. The limiters are functions of dimensionless quantity r which is computed using Darwish and Moukalled's formulation [4]. To represent the overall viscosity supplied by the modified Roe-MUSCL, the first tensorial invariant $\text{Tr}\,(\boldsymbol{\nu}_{\text{num}})$ is considered.

The numerical viscosity spectrum $\widehat{\nu}_{\text{num}}(k,t)$ and the dissipation rate spectrum $\widehat{\epsilon}_{\text{num}}(k,t)$ provide quantitative information on the numerical dissipation inherent to a scheme, as well as on its accuracy. In Bidadi and Rani [64], these were computed as follows:

$$\widehat{\nu}_{\text{num}}(k,t) = \sqrt{\sum_{|\mathbf{k}'|=k} \widehat{\nu}_{\text{num}}(\mathbf{k}',t)\ \widehat{\nu}^{*}_{\text{num}}(\mathbf{k}',t)} \tag{5.15}$$

$$\widehat{\epsilon}_{\text{num}}(k,t) = 2\ \widehat{\nu}_{\text{num}}(k,t)\ k^2 E(k,t) \tag{5.16}$$

where $E(k,t)$ is the turbulent kinetic energy spectrum, and ν_{num} is the first tensorial invariant $\text{Tr}(\boldsymbol{\nu}_{\text{num}})$. The two spectra are normalized as

$$\widehat{\nu}^{+}_{\text{num}} = \frac{\widehat{\nu}_{\text{num}}(k,t)}{\widehat{\nu}_{\text{num,ref}}(k_c,t)} \tag{5.17}$$

$$\widehat{\epsilon}^{+}_{\text{num}} = \frac{\widehat{\epsilon}_{\text{num}}(k,t)}{\widehat{\epsilon}_{\text{num,ref}}(k_c,t)} \tag{5.18}$$

where $\widehat{\nu}_{\text{num,ref}}(k_c,t)$ and $\widehat{\epsilon}_{\text{num,ref}}(k_c,t)$ are the viscosity and dissipation rate at the cut-off wavenumber k_c. In the context of LES, Schilling and Zhou [110] employed the eddy-damped quasinormal Markovian (EDQNM) model together with a sharp Fourier cut-off filter to derive expressions for the spectra of eddy viscosity and backscatter viscosity in high-Reynolds-number decaying isotropic turbulence.

5.4 Results

Results obtained from ILES simulations of nominally inviscid TGV problem are discussed in this section. Computations were performed using three forms of Roe-MUSCL flux formulation: the original second-order Roe-MUSCL with *no* z-factor modification (NM), and Roe-MUSCL with the *current* z-factor modification (CM) shown in (5.14), and with the Thornber et al. *low Mach-number* z-factor modification

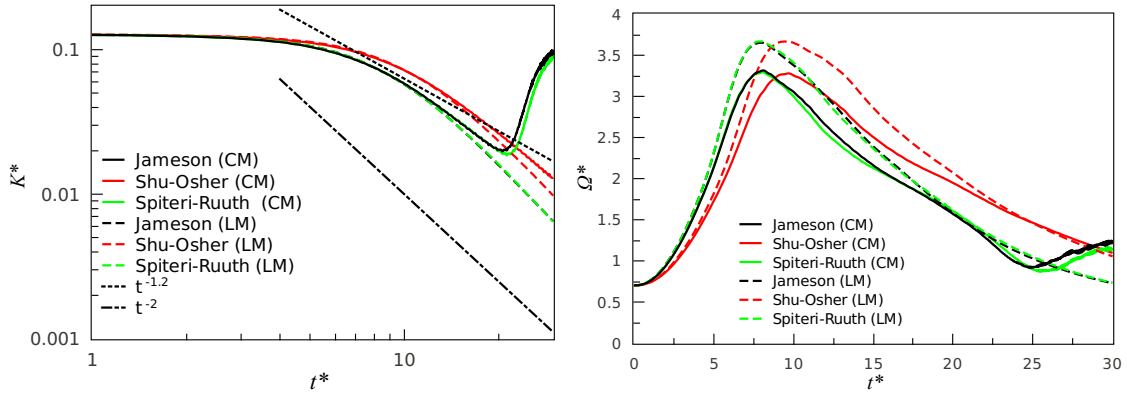

Figure 5.1: Temporal evolution of dimensionless (a) turbulent kinetic energy, and (b) enstrophy for Jameson, Shu-Osher and Spiteri-Ruuth Runge-Kutta schemes along with current modification (CM) and Thornber et al. modification (LM) schemes. Results for no modification (NM) scheme are not shown here.

(LM) [9]. These spatial schemes are in turn combined with the Runge-Kutta-based temporal schemes of Jameson et al. [15], Shu-Osher [104] and Spiteri-Ruuth [17]. All simulations were performed using minmod limiter with scaling parameter $\Lambda = 1$, and CFL number of 0.4.

According to Shu et al. [16], it is essential to consider the behavior of more than one statistical quantity before drawing conclusions on the performance of a numerical scheme. Therefore, a number of statistics were computed both in temporal and spectral spaces so as to assess the schemes' ability to capture physics during various stages of TGV evolution. Spectral statistics included the energy spectra, as well as the numerical viscosity and dissipation rate spectra. They provide insights into the schemes' dissipative characteristics as the TGV system evolves in time. Finally, effective Reynolds number Re_{eff} was estimated using (5.13), and compared with Reynolds numbers from prior DNS and ILES/LES studies.

Figure 5.1 shows the time evolution of dimensionless turbulent kinetic energy (TKE) $K^* = 1/2 \langle u_i u_i \rangle / U_0^2$ and enstrophy $\Omega^* = \langle \omega^2 \rangle / (kU_0)^2$. TKE and enstrophy profiles corresponding to the no-modification (NM) case are not shown due to the excessive dissipation inherent to the original Roe-MUSCL. It can be seen in Figure 5.1(a) that all three temporal schemes in conjunction with CM and LM essentially preserve the initial TKE for $t^* \lesssim 5$, where $t^* = kU_0 t$. In transitional flow simulations, the longer a numerical scheme preserves the initial TKE, the better the scheme is able to capture the growth of flow perturbations and the consequent transition to turbulence. For $t^* \gtrsim 5$, K^* decays monotonically with time, except for cases involving the combination of current z-factor modification (CM) with either the Jameson et al. or the Spiteri and Ruuth time scheme. These two CM cases in fact become numerically unstable for $t^* \gtrsim 20$. The numerical instability is a direct result of the dispersive symmetric fluxes dominating the dissipative fluxes in these schemes. The Shu-Osher scheme with both CM and LM preserves the initial kinetic energy longer than the other cases, which suggests that Shu-Osher is better suited for simulating transitional flows. At longer times with $t^* \gtrsim 20$, Shu-Osher-CM preserves more kinetic energy than even Shu-Osher-LM, which is also manifested as marginally higher enstrophy during these times in Figure 5.1(b).

Also shown in Figure 5.1(a) are temporally decaying profiles corresponding to $t^{*^{-1.2}}$ and $t^{*^{-2}}$. The $t^{*^{-1.2}}$ functionality of TKE is considered to be characteristic of decaying isotropic turbulence [111], whereas $t^{*^{-2}}$ decay suggests that energy containing eddies with sizes larger than the domain cannot exist. This long-time decay is referred to in literature [100] as the "later-time" quadratic law. In the current study, during

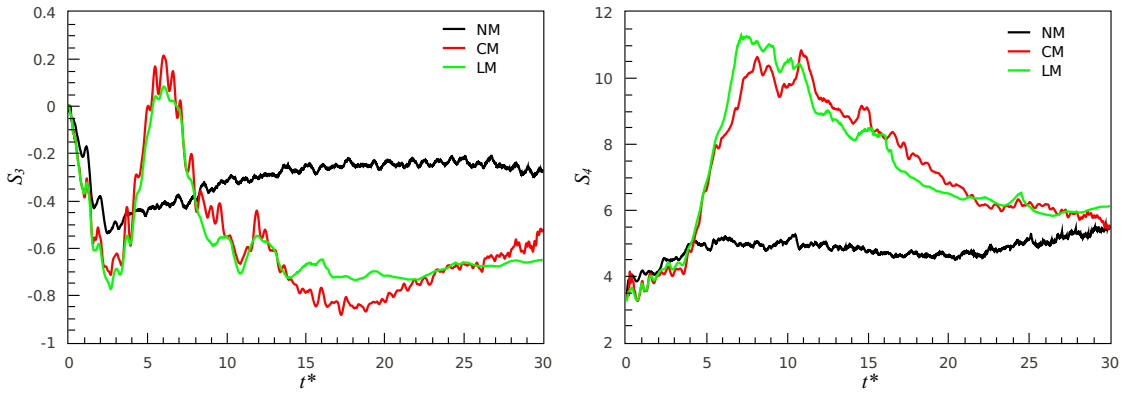

Figure 5.2: Temporal evolution of (a) skewness S_3, and (b) flatness S_4 for NM, CM and LM schemes. All profiles are obtained using Shu-Osher scheme.

the initial decay period, all K^* profiles exhibit a slope of -1.2, whereas towards the end of the simulation, the decay exponent is closer to -2. These trends in the decay of TKE are in good agreement with LES and ILES simulations of Drikakis et al. [100] and ILES simulations of Aspden et al. [108]. Figure 5.1(b) shows that enstrophy profiles corresponding to Jameson and Spiteri-Ruuth schemes with CM and LM peak at $t^* \sim 8$, while those for Shu-Osher with CM and LM peak at $t^* \sim 9.5$. The Shu-Osher predicted value of $t^* \sim 9.5$ is closer to that reported in [100]. Furthermore, it can be seen that temporal schemes with LM generate more enstrophy than with CM.

The temporal evolution of skewness $S_3 = -\langle\left(\frac{\partial u}{\partial x}\right)^3\rangle / \langle\left(\frac{\partial u}{\partial x}\right)^2\rangle^{\frac{3}{2}}$ for NM, CM and LM with Shu-Osher is presented in Figure 5.2(a). Profiles for Jameson et al. and Spiteri-Ruuth schemes are not shown since these schemes develop numerical instabilities. During the laminar flow phase corresponding to times $t^* \lesssim 4$, skewness profiles for both CM and LM are negative and evolve close to each other. The correspond-

ing skewness profile for NM is in general of smaller magnitude compared to CM and LM. During the time $4 \lesssim t^* \lesssim 8$, corresponding to the transition phase, skewness for NM remains negative, while that for both CM and LM attains a positive peak and decreases subsequently. The rather abrupt changes in the sign of skewness for CM and LM may be attributed to the fact that higher order structure functions are extremely sensitive to local perturbations in velocity gradients that may be further amplified by the dispersive nature of these two schemes [31]. The sudden changes are also indicative of flow transitioning from laminar to turbulent regime. The lack of a peak in the NM skewness profile is due to the excessive dissipation inherent to Roe-MUSCL. For longer times, skewness is negative for all three modifications, with NM having the smallest magnitude indicating that NM does not result in fully developed turbulence.

The time evolution of flatness $S_4 = -\langle \left(\frac{\partial u}{\partial x}\right)^4 \rangle / \langle \left(\frac{\partial u}{\partial x}\right)^2 \rangle^2$ is shown in Figure 5.2(b). During early times, NM flatness is marginally higher than that of CM and LM. Subsequently, CM and LM show a sharp increase in flatness, while that for NM essentially plateaus. The steep rise in flatness for CM and LM is due to: (i) amplification of small-amplitude perturbations by the dispersion inherent to these schemes, and (ii) susceptibility of flow to instabilities that develop during the transition phase, thereby making the flow highly intermittent during this time. A closer observation of the profiles shows LM exhibiting greater flatness in the transition phase compared to CM. Since flatness is a measure of intermittency in the flow-field, LM generates larger perturbations which results in greater enstrophy than CM, as seen in Figure 5.1(b).

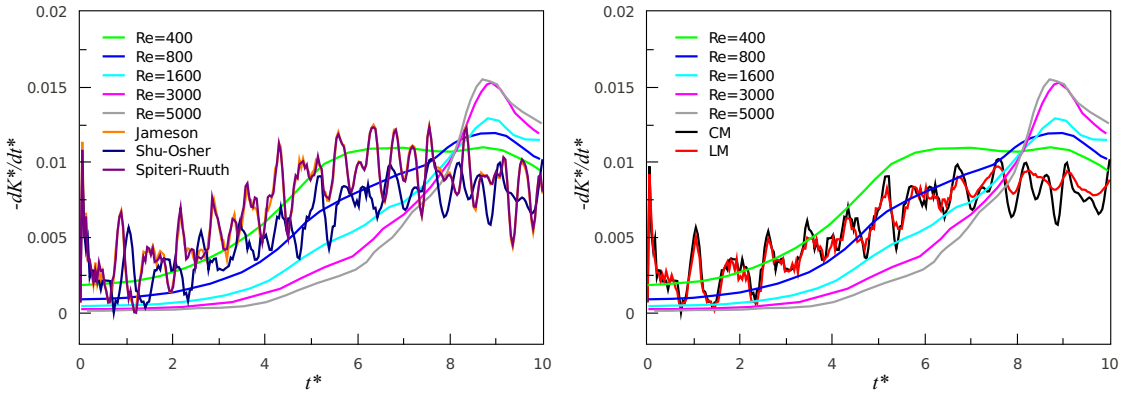

Figure 5.3: Evolution of $-dK^*/dt^*$ for (a) Jameson, Shu-Osher and Spiteri-Ruuth schemes with CM, and (b) CM and LM with Shu-Osher scheme. Profiles from pseudo-spectral DNS studies of Brachet et al. [13] and Brachet [14] at $Re = 400,\ 800,\ 1600,\ 3000$, and 5000 are presented for comparison.

Eventually, toward the end of simulations, all three flatness profiles move close to each other due to decay in turbulence.

Figure 5.3 presents TKE dissipation rate $-dK^*/dt^*$ as a function of time. The effects of temporal schemes (when combined with CM) on time evolution of dissipation rate are shown in Figure 5.3(a), while the effects of CM and LM (when combined with Shu-Osher) are shown in Figure 5.3(b). The DNS profiles at $Re = 400,\ 800,\ 1600,\ 3000$, and 5000 obtained from the references [13, 14] are also shown in Figure 5.3(a) and Figure 5.3(b). In both figures, profiles from current simulations are significantly more oscillatory compared to the DNS [13, 14]. The fluctuations reflect the effects of central-differenced dispersive terms in the Roe-MUSCL fluxes. In Figure 5.3(a), it may be noted that oscillations for Shu-Osher are smaller compared to those for the other two temporal schemes. This is because Shu-Osher is the

most stable among the temporal schemes considered. In Figure 5.3(a), the Jameson and Spiteri-Ruuth profiles peak earlier than Shu-Osher profile, as was the case for enstrophy in Figure 5.1(b). In Figure 5.3(b), the CM and LM profiles show similar oscillatory behavior, although the former has marginally larger amplitudes. This is because CM is more dispersive than LM. In both figures, dissipation rate profiles are closest to the $Re = 400$ DNS curve.

Table 5.2: Effective Reynolds number Re_{eff} for Jameson, Shu-Osher and Spiteri-Ruuth temporal schemes with CM and LM at $t^* = 10, 15$ and 20.

	CM			LM		
t^*	Jameson	Shu-Osher	Spiteri-Ruuth	Jameson	Shu-Osher	Spiteri-Ruuth
10	377	412	375	399	445	381
15	745	582	734	629	615	630
20	784	974	728	879	828	806

Table 5.2 provides the effective Reynolds number Re_{eff} estimated using (5.13) at $t^* = 10, 15$ and 20. The Re_{eff} values presented are for the three temporal schemes in combination with CM and LM, respectively. As discussed previously, the slope of TKE profiles during this time period is ≈ 1.2 (see Figure 1), which corresponds to decaying isotropic turbulence-like simulation. However, at later stages ($t^* > 20$), $K^* \sim t^{*-2}$.

To examine the effectiveness of schemes in transitioning the TGV system away from the initial symmetries, isocontour plots of vorticity at $t^* = 26$ obtained using Shu-Osher with NM, CM and LM are presented in Figure 5.4. It can be seen in Figure 5.4(a) that the symmetries imposed by the initial conditions at the π-planes

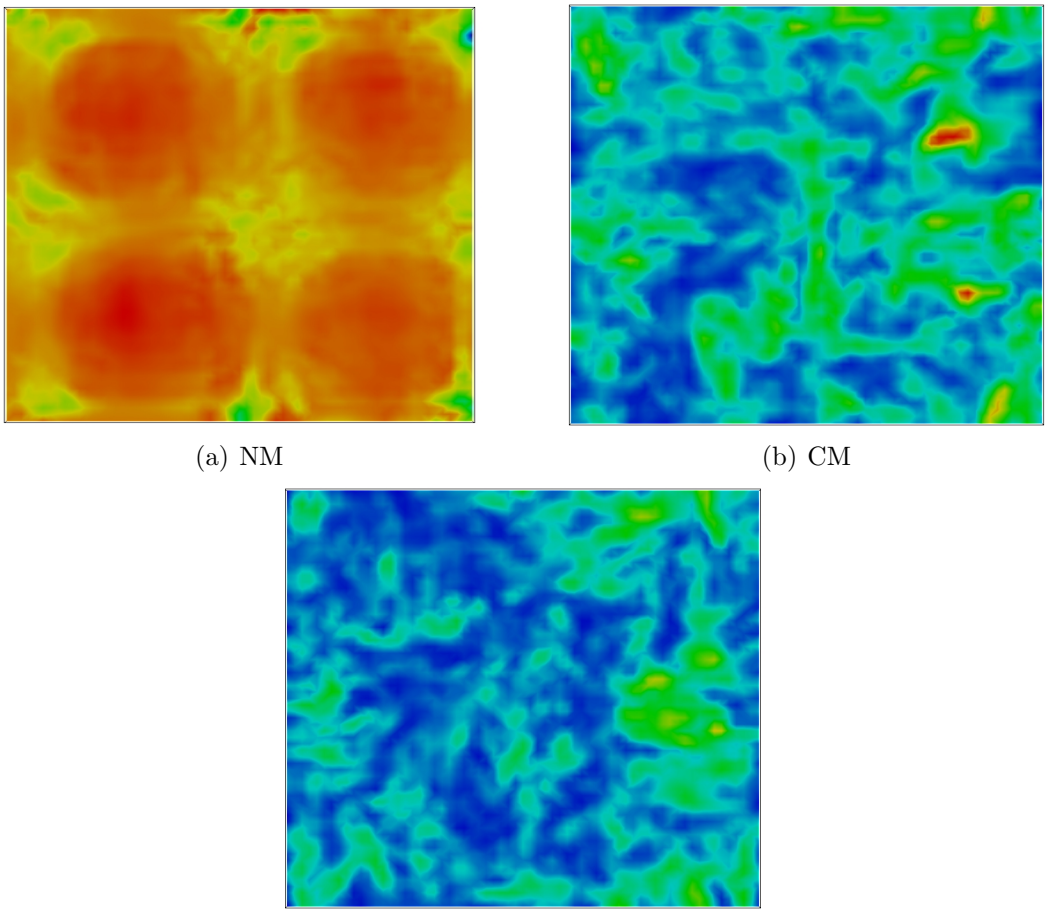

(a) NM

(b) CM

(c) LM

Figure 5.4: Vorticity contours of NM, CM and LM with Shu-Osher scheme at $t^* = 26$.

are essentially preserved for NM, whereas transition to turbulence is successfully captured by both CM and LM (Figure 5.4(b) and Figure 5.4(c)). NM failed in capturing the physics of transition due to its excessive numerical diffusion. CM and LM are successful because, during the early stages of flow development, the hyperbolic component of Roe-MUSCL fluxes are dominant. The hyperbolic fluxes strengthen the centrifugal forces that drive the transition of initial counter-rotating vortices to the impermeable stress-free faces, as well as the subsequent formation of vortex sheets.

However, as the flow evolves, diffusive component of Roe-MUSCL fluxes play an increasingly important role. Nevertheless, dispersive fluxes continue to dominate in CM and LM. This leads to the tearing of closed vortex sheets that reconnect almost immediately to form vortex tubes [31]. These tubes then undergo constant tearing and reconnection, eventually leading to breakdown of initial symmetry. LM seems to capture this physics better than CM due to the greater intermittency seen in LM (Figure 5.2(b)). Hence, to trigger the vortex-stretching mechanism, numerical dissipation must be kept to a minimum.

The spectra of turbulent kinetic energy (TKE) are shown in Figure 5.5. Figure 5.5(a) and Figure 5.5(c) compare the TKE spectra of Jameson, Shu-Osher and Spiteri-Ruuth schemes in combination with CM at $t^* = 10$ and 26. At $t^* = 10$, the energy spectra are similar to those observed in decaying isotropic turbulence. This is to be anticipated since by this time (i.e., $t^* \sim 10$), the flow is close to the end of transition process. In Figure 5.5(a), the Shu-Osher spectrum contains greater energy than the Jameson and Spiteri-Ruuth spectra at all wavenumbers. This is because Shu-Osher preserves the initial TKE for longer times than the other two schemes, as already seen in Figure 5.1(a). At $t^* = 26$, Jameson and Spiteri-Ruuth schemes with CM perform poorly due to the energy build-up observed in the inertial subrange (Figure 5.5(c)). It will be seen that the instability of these two temporal schemes can be explained using dissipation rate spectra.

Figure 5.5(b) and Figure 5.5(d) compare the energy spectra for the NM, CM and LM schemes combined with Shu-Osher. It is evident that at both time instances, NM is the most dissipative. At $t^* = 10$, energy spectra for CM and LM are quite

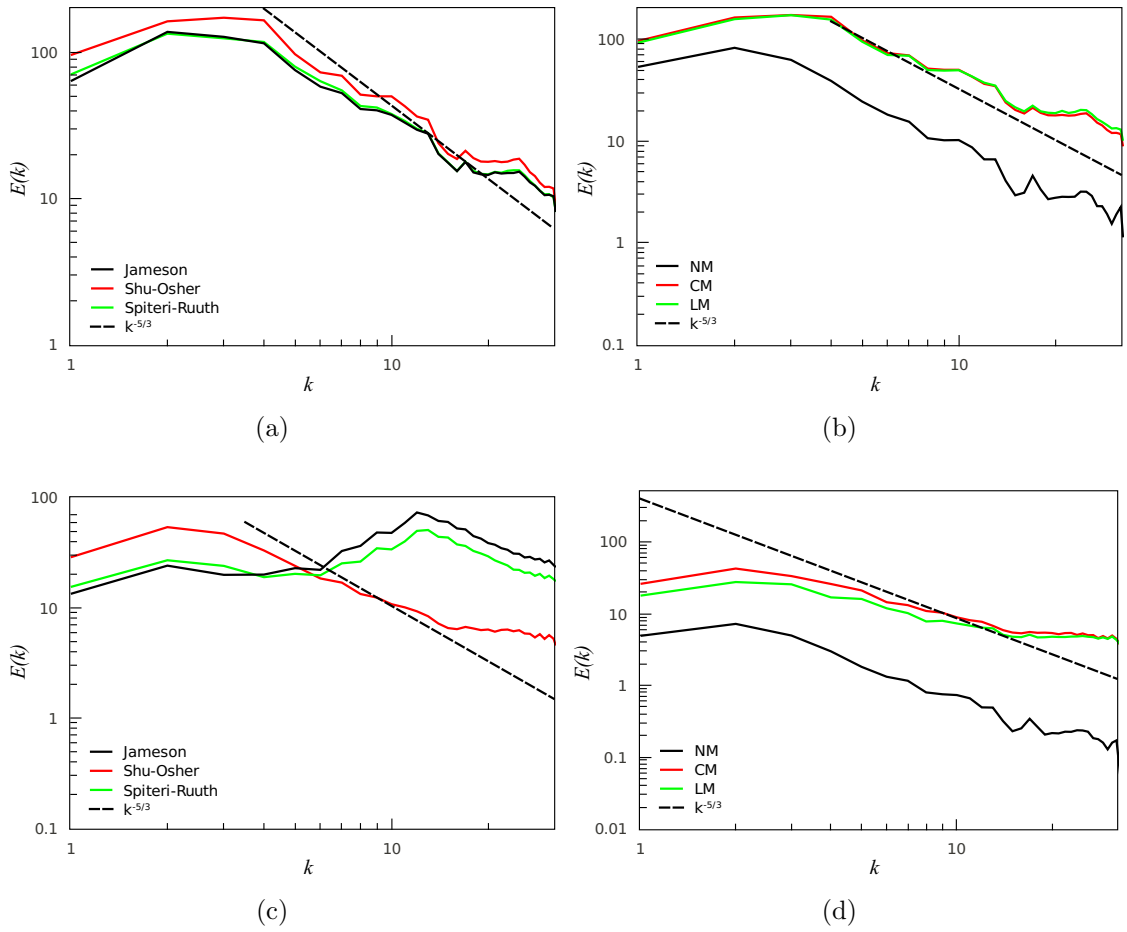

Figure 5.5: Comparison of energy spectra for (a) Jameson, Shu-Osher and Spiteri-Ruuth Runge-Kutta schemes with CM, and (b) NM, CM and LM with Shu-Osher scheme at $t^* = 10$. Profiles in (c) and (d) are for the same combinations at $t^* = 26$. Kolmogorov's $-5/3$ scaling law profile is also shown.

close to each other, while at $t^* = 26$, CM contains marginally higher energy than LM. At $t^* = 26$, both CM and LM spectra exhibit a less than $-5/3$ slope. A similar behavior was also noted by Aspden et al. [108] in their inviscid TGV simulations.

The normalized spectra of numerical viscosity $\widehat{\nu}^+$ and dissipation rate $\widehat{\epsilon}^+$ at $t^* = 10$ are shown in Figure 5.6, while the corresponding spectra at $t^* = 26$ are shown in Figure 5.7. In Figure 5.6(a), numerical viscosity spectra of the three temporal

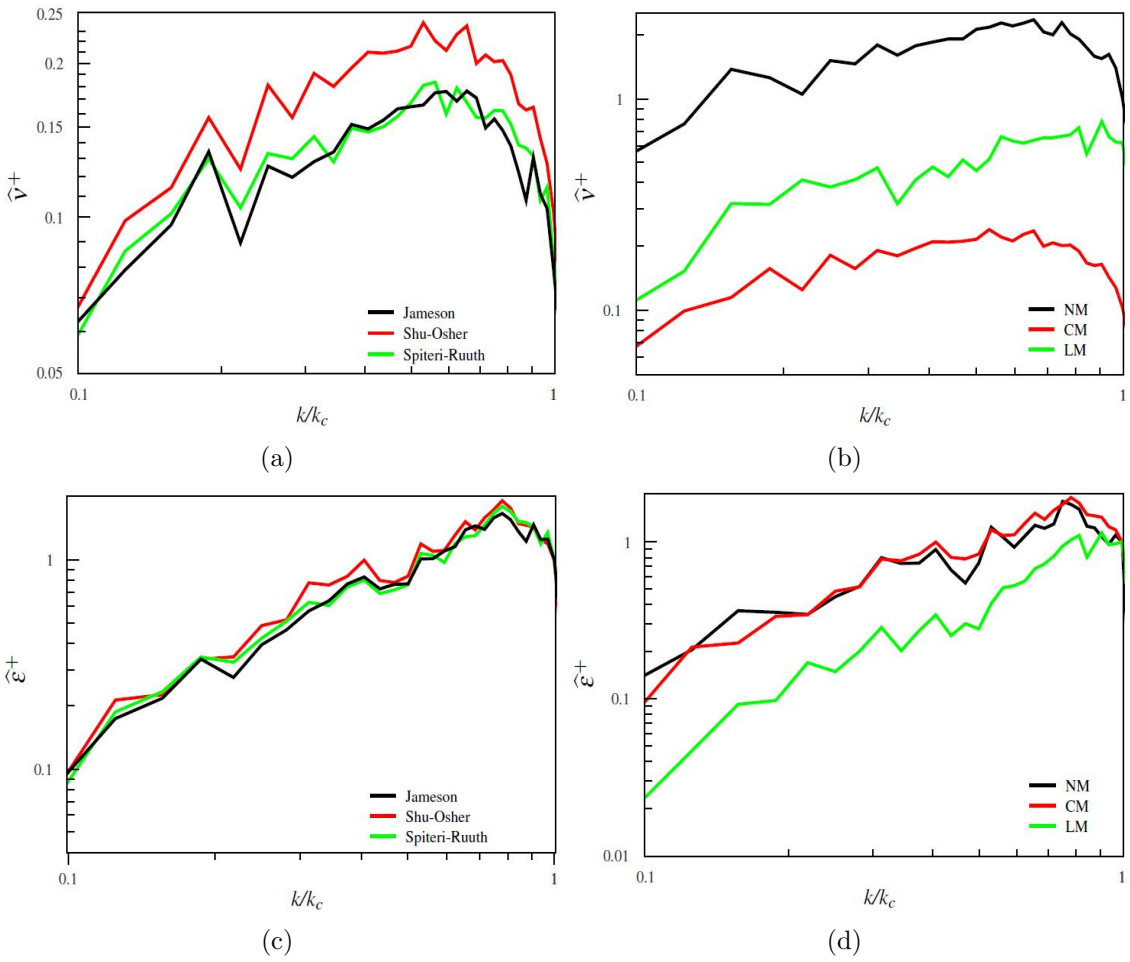

Figure 5.6: Spectra of normalized numerical viscosity and dissipation rate: (a) and (c) Jameson, Shu-Osher and Spiteri-Ruuth schemes with CM, and (b) and (d) NM, CM and LM with Shu-Osher scheme at $t^* = 10$.

schemes with CM are compared, while in Figure 5.6(c) the corresponding dissipation rate spectra are compared. It is observed in Figure 5.6(a) that Shu-Osher supplies more viscosity compared to Jameson and Spiteri-Ruuth at all wavenumbers. The dissipation spectra in Figure 5.6(c), however, show all three temporal schemes with similar dissipation magnitudes. The profiles increase sharply with a slope of ~ 1.1 before peaking ahead of the cutoff wavenumber k_c. This slope in the dissipation rate

spectra seemingly ensures correct rate of energy transfer, and consequently results in successful scale separation, i.e. the close to $-5/3$ slope, observed in Figure 5.5(a).

To compare NM, CM and LM when combined with Shu-Osher, $\widehat{\nu}^+$ and $\widehat{\epsilon}^+$ spectra are shown in Figure 5.6(b) and Figure 5.6(d), respectively. As expected, NM provides maximum viscosity and CM the least at all wavenumbers. The lowest viscosity of CM is a direct manifestation of applying the z-factor to directly mitigate numerical viscosity, as opposed to applying it to reduce velocity jumps at an interface in LM. But, the dissipation rate of LM is smaller than that of CM at all wavenumbers, which may be attributed to the marginally higher preservation of initial TKE for CM than LM (Figure 5.1(a)).

The $\widehat{\nu}^+$ and $\widehat{\epsilon}^+$ spectra at $t^* = 26$ are shown in Figure 5.7. Figure 5.7(a) shows Shu-Osher scheme with CM supplying less viscosity than Jameson and Spiteri-Ruuth schemes. The higher magnitudes for the latter time schemes are a consequence of the energy build-up observed in Figure 5.5(c). The $\widehat{\epsilon}^+$ spectra in Figure 5.7(c) explain the numerical instability of Jameson and Spiteri-Ruuth. As the figure shows, magnitude of dissipation rate of the two schemes at low wavenumbers is smaller compared to that of Shu-Osher. In fact, at these wavenumbers, the dissipation rate slope is ~ 3 which is in sharp contrast to a relatively moderate slope of ~ 1.1 for Shu-Osher. Since the rate at which kinetic energy is dissipated is approximately equal to the energy transfer rate [25], profiles in Figure 5.7(c) suggest that Jameson and Spiteri-Ruuth with CM are incapable of transferring kinetic energy to smaller scales at the correct rate. Consequently, there is significant energy build-up in the inertial subrange. Thus, the slope of $\widehat{\epsilon}^+$ spectrum can provide insights into the stability of a numerical scheme.

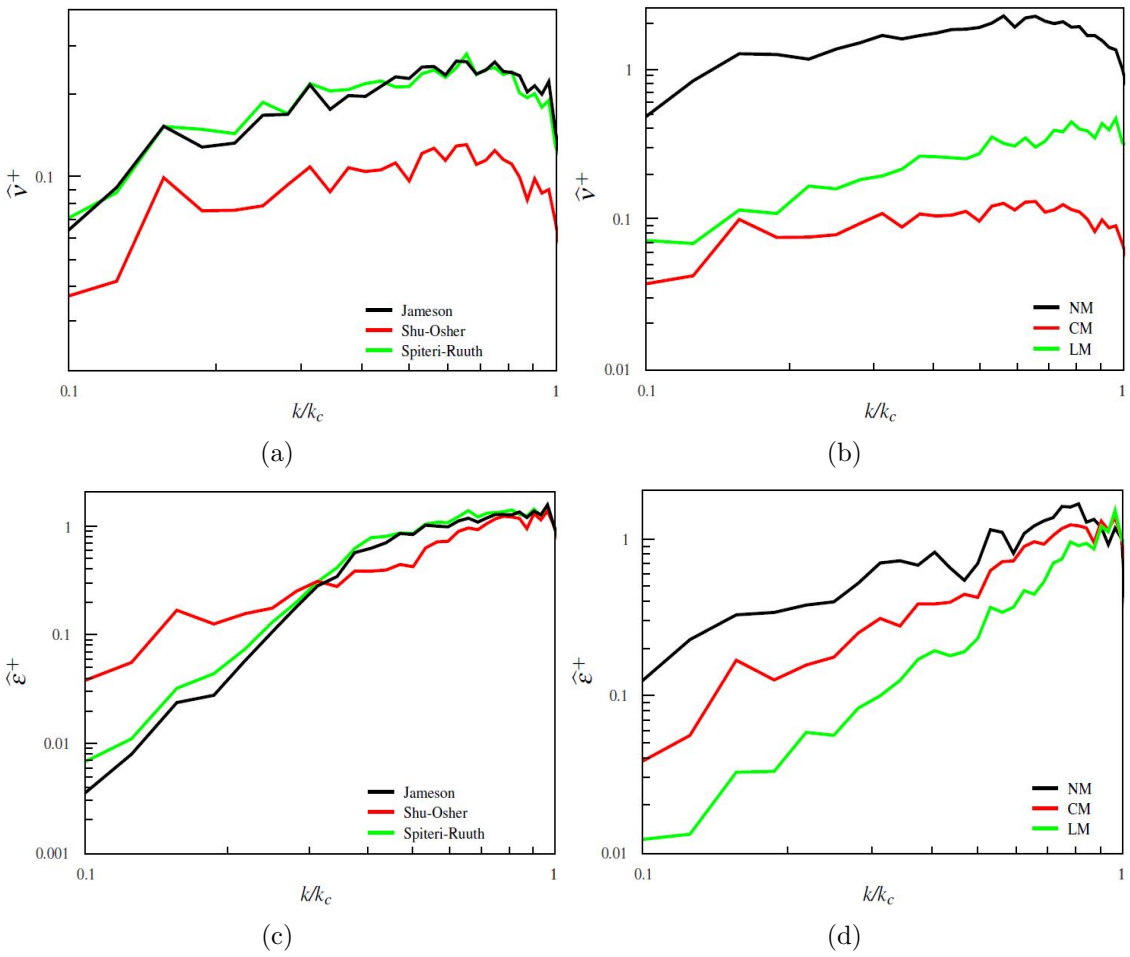

Figure 5.7: Spectra of normalized numerical viscosity and dissipation rate: (a) and (c) Jameson, Shu-Osher and Spiteri-Ruuth schemes with CM, and (b) and (d) NM, CM and LM with Shu-Osher scheme at $t^* = 10$.

Figure 5.7(b) and Figure 5.7(d) show the viscosity and dissipation rate spectra for NM, CM and LM schemes with Shu-Osher at $t^* = 26$. The trends in these spectra are similar to those at $t^* = 10$. The dissipation rate spectra provide important information on the performance of the schemes. The slopes of the spectra are nearly the same and close to what is ideally needed to avoid energy from accumulating. However, near the cutoff wavenumber k_c, both CM and LM dissipate energy at rates similar to NM which has very little kinetic energy left at this stage. This lower than

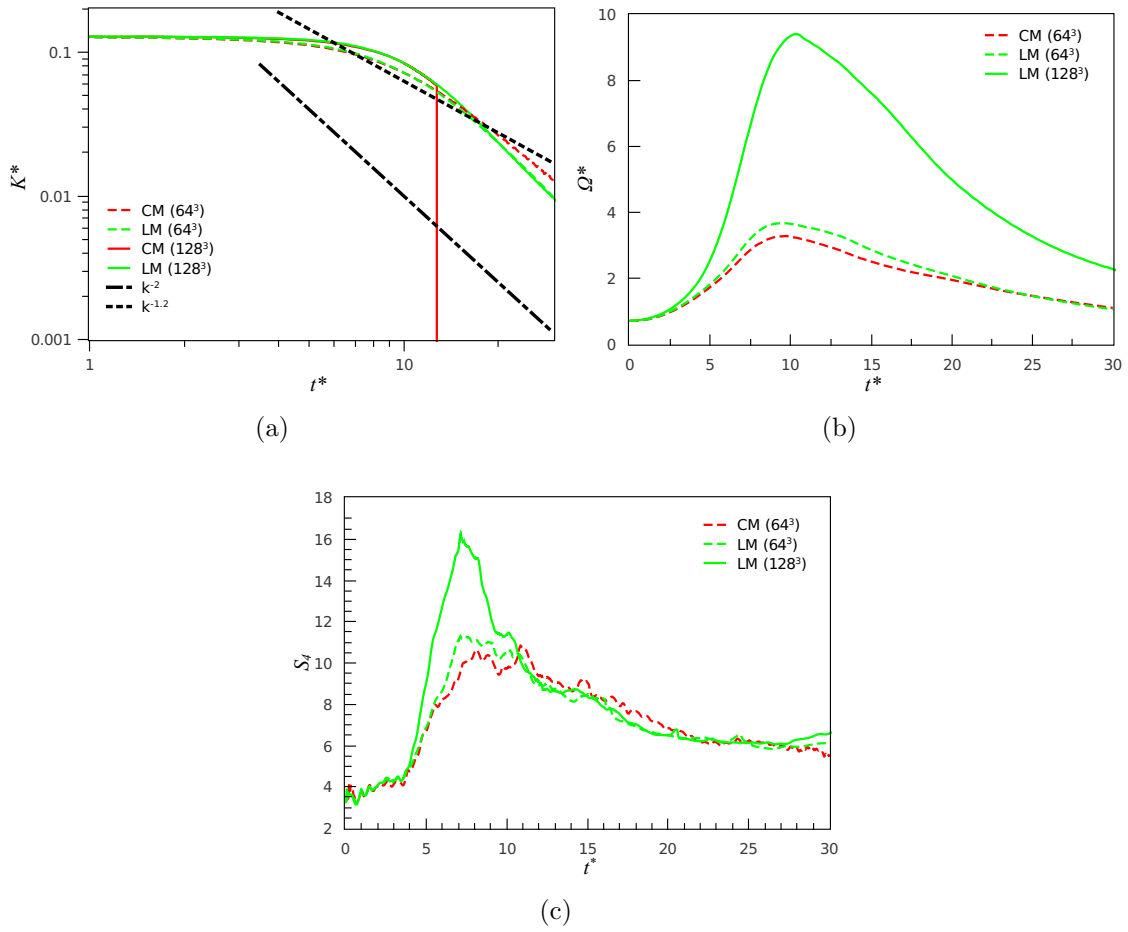

Figure 5.8: Temporal evolution of (a) normalized turbulent kinetic energy, (b) normalized enstrophy, and (c) flatness for CM and LM with Shu-Osher scheme on 64^3 and 128^3 mesh resolutions. CM profile on 128^3 grid is shown only for (a).

expected magnitude in $\widehat{\epsilon}^{+}$ for CM and LM is a possible explanation for the slope of $E(k)$ to be less than $-5/3$ at high wavenumbers in Figure 5.5(d).

The time evolution of dimensionless kinetic energy and enstrophy, K^* and Ω^* respectively, as well as flatness S_4 at 128^3 grid resolution are shown in Figure 5.8. Also included are the corresponding profiles for the 64^3 grid case. Profiles are shown for CM and LM with Shu-Osher. It can be seen in Figure 5.8(a) that CM on 128^3 grid becomes unstable at $t^* \approx 12$ due to insufficient numerical viscosity. This is

in contrast with LM that maintains stability on the finer grid as well. The TKE decay rate for CM and LM on the 64^3 grid, and for LM on 128^3 grid scales as $t^{*^{-1.2}}$ toward the end of transition, and as $t^{*^{-2}}$ toward the end of simulation. A closer look at the kinetic energy plot also reveals that higher grid resolution delays the time when the simulation becomes under-resolved. Figure 5.8(b) demonstrates that LM generates substantially higher enstrophy on the 128^3 grid than on the 64^3 grid, which is indicative of LM's ability to prevent the flow from becoming under-resolved for longer times. The large increase in Ω^* for LM during the transition period may be correlated with lower dissipation, as well as with greater intermittency as reflected by the significantly higher peak in S_4 in Figure 5.8(c).

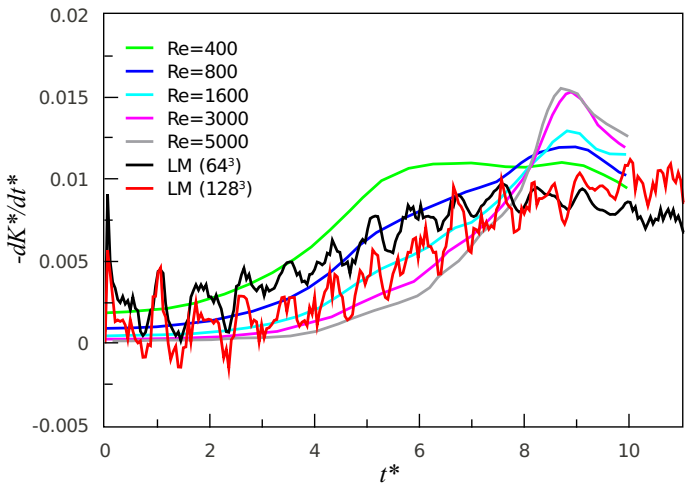

Figure 5.9: Comparison of temporal evolution of $-dK^*/dt^*$ for Thornber et al. low Mach-number modification [9] and Shu-Osher combination with pseudospectral DNS data of Brachet et al. [13] and Brachet [14] at $Re = 400,\ 800,\ 1600,\ 3000$, and 5000.

The temporal evolution of dimensionless dissipation rate $-dK^*/dt^*$ for LM with Shu-Osher on 64^3 and 128^3 grids is shown in Figure 5.9. The profiles are com-

pared with DNS data of Brachet et al. [13] and Brachet [14] at $Re = 400,\ 800,\ 1600,\ 3000,$ and 5000. The dissipation rate on the 128^3 grid during laminar and transition stages is smaller than that on the 64^3 grid. At $t^* = 10$, the former exceeds the latter with an effective Reynolds number $Re_{\text{eff}} = 829$. Although the profile on the finer grid is close to the $Re = 800$ DNS curve, there is a slight delay in the occurrence of the peak in the simulation data.

CHAPTER 6

CONCLUSIONS AND FUTURE WORK

6.1 Conclusions

The goal of this study is to provide further justification for the implicit large-eddy simulation (ILES) approach based on shock-capturing schemes for accurately representing the motion of both incompressible and compressible turbulent flows, as well as laminar to turbulent flow transition. The study was primarily motivated by the limitations of popular LES-SGS models to accurately simulate high Mach number turbulent flows and the vortex stretching mechanism that is crucial to transition an initial laminar flow-field to fully developed turbulence.

The high-resolution Roe-MUSCL scheme together with the low-Mach number modifications successfully captured the physics of compressible isotropic turbulence and Taylor-Green vortex transitional flow problem. As a consequence, the current ILES approach satisfied the two criteria of Drikakis et al. [26]. In addition to a number of temporal statistics, spectra of numerical viscosity and dissipation rates demonstrated why the approach is successful. In the remainder of this section, the contributions made in each of the chapters are highlighted.

For the non-linear advection equation (Chapter 2), a numerical viscosity formulation was derived for the combined Roe-MUSCL scheme when solving the 3-D advection equation. The explicit expression for the numerical viscosity recovers the UDS scheme when $\psi = 0$ and the second-order CDS at $\psi = 1$ or 2 depending the choice of the scaling parameter Λ. This new formulation was then applied to quantify the numerical viscosity of the minmod, superbee, van Leer and Barth-Jesperson TVD limiters for four problems. It is shown that the superbee scheme consistently provides the lowest numerical viscosity that is also most active around the discontinuity. The minmod scheme is most diffusive, as well as active in regions away from the discontinuity. The impact of the scaling parameter Λ on the profiles was also examined in detail. It is shown that the combination of $\Lambda = 1$ and $\psi = 2$ results in anti-diffusion being added to the advection equation. While the effects of this anti-diffusion were not apparent in the 1-D case, the 2-D cases studied clearly demonstrate that it leads to non-monotonicity. Choosing $\Lambda = 2$ always ensures monotonic behavior for all the TVD schemes, but at the cost of increased viscosity. The effects of non-orthogonal meshes on numerical viscosity was also investigated. For the cases considered, it was found that the numerical viscosity was lower for the non-orthogonal mesh than for an orthogonal mesh of similar resolution. This study also serves the important purpose of clarifying the consequences of extending the Roe-MUSCL scheme and the limiters, which were originally developed for 1-D orthogonal meshes, to multi-dimensional and non-orthogonal meshes.

In the case of Euler equations (Chapter 3), a formulation to estimate the numerical viscosity inherent to second-order TVD-MUSCL schemes through a 3-D

extension of Roe's original flux is presented. The flux and numerical viscosity expressions derived are applicable to both structured and unstructured grids. A z-factor modification approach, inspired by Thornber et al. study [9], is developed, whose effects on the viscosity profiles were investigated as well. Numerical experiments for the 1-D shock-tube and 2-D inviscid supersonic wedge flow were conducted to quantify the spatial distribution of viscosity supplied by minmod, van Leer and superbee limiters. For these flow cases, it was found that minmod with $\Lambda = 1$ is the least diffusive of the ψ-Λ combinations investigated. The viscosity profiles of all limiters peaked upstream of the jumps to suppress the high level of solution oscillations in these regions. It was also observed that the current and Thornber et al. z-factor modifications (CM and LM [9]) perform better than the no z-factor modification (NM).

In Chapter 4, ILES of decaying HIT cases were performed for initial turbulent Mach numbers, $M_{t_0} = 0.1$, 0.3 and 0.5, with initial compressibility ratio $\chi_0 = 0$ and zero fluctuations in the thermodynamic quantities, and for mesh resolutions of 32^3, 64^3 and 128^3. In the $M_{t_0} = 0.1$ case, the energy spectra for NM fail to capture the inertial subrange due to NM's highly dissipative nature. CM and LM schemes showed excellent agreement with experimental results for all three grid resolutions. The skewness parameter S_3 on 32^3 and 128^3 grids for CM were found to be very close to the experimental results of Kang et al. [11] for $Re_\lambda = 720$. However, its magnitude was found to be surprisingly lower on the 64^3 grid when compared to that on the 32^3 grid. Normalized viscosity and dissipation-rate spectra were presented for the two coarse grid resolutions, which clearly demonstrate the positive impact of the z-factor

modifications. The numerical dissipation rates are significantly reduced for the CM and LM cases in the low wavenumber region. In addition, the wavenumber range over which numerical dissipation occurs was also observed to decrease with these two schemes.

For the quasi-isentropic regime ($M_{t_0} = 0.3$) case, the energy spectra for current and Thornber et al. schemes showed good agreement with Kolmogorov's $-5/3$ law. The deviation from this slope at high wavenumbers may be attributed to the dissipation rates peaking at wavenumbers lower than those reported for the CBC experiments. Magnitude of skewness S_3 was again found to be lower for the 64^3 grid, while the decay exponent p for CM and LM schemes was closer to Saffman's result [101]. Enstrophy profiles for the 64^3 grid exhibited peaks that were absent in the lowest grid resolution case. The temporal evolution of kinetic energy and thermodynamic properties show the CM scheme on the 64^3 grid providing the largest amount of compression and preserving more kinetic energy than the simulations of Honein and Moin [10] for the same grid resolution.

The velocity derivative PDFs for all schemes were successful in capturing turbulent intermittency. However, only the PDFs of modified schemes on 64^3 grid showed good agreement with the experimental and DNS results of Kang et al. [11] and Vincent and Meneguzzi [12], respectively. The PDF of pressure fluctuations for CM on 64^3 grid showed maximum negative skewness compared to the other two schemes. This indicates strong correlation between pressure and vorticity which is to be expected in simulations of HIT. We conclude that the simulations conducted on this finer mesh using the current z-factor is capable of satisfactorily capturing the physics

of decaying isotropic turbulence. The simulation results for the non-linear subsonic regime ($M_t = 0.5$) case on 32^3 and 64^3 grids are similar to those for $M_t = 0.3$, except that the former has higher flow compressibility due to the stronger non-linear interactions between the velocity components. However, shocklets were observed only for the 128^3 grid simulation.

The stability and accuracy of Roe-MUSCL scheme with no z-factor modification (NM), current z-factor modification (CM) and Thornber et al. z-factor modification (LM) together with Jameson, Shu-Osher and Spiteri-Ruuth temporal schemes was also investigated for the Taylor-Green vortex (TGV) problem (Chapter 5). NM was found to be excessively diffusive as it fails to develop the conditions necessary to transition the initially laminar field to a fully developed turbulent flow. On the other hand, the modifications demonstrated successful transition to decaying isotropic turbulent flow. LM does a slightly better job than CM in breaking the initial symmetries due to lower dissipation and greater intermittency in the transition phase.

The temporal evolution of a number of statistical quantities for simulations conducted on 64^3 grid was discussed. The TKE profiles for Shu-Osher scheme with CM and LM preserved the initial kinetic energy for the longest time compared to other spatial-temporal scheme combinations. The profiles exhibited a slope of -1.2 during the initial decay period and a slope of -2 toward the end of the simulations. The enstrophy production for LM was more than CM due to greater intermittency in the domain, as shown by the corresponding skewness S_3 and flatness S_4 profiles. The dissipation rate profiles were found to be oscillatory, primarily due to the dispersive fluxes inherent to Roe-MUSCL. However, the underlying trends were similar to the

DNS data at $Re = 400$. Furthermore, Ω^* profiles of Jameson and Spiteri-Ruuth schemes with CM and LM peaked earlier compared to the Shu-Osher scheme.

In addition to energy spectra, spectra of numerical viscosity and dissipation rate provide significant insights into the dissipative nature of the schemes. The dissipation rate spectra demonstrated that the energy build-up observed in the case of Jameson and Spiteri-Ruuth schemes with CM at $t^* = 26$ was due to the insufficient rate of energy down to the smaller eddies. Consequently, dissipation spectra for these two schemes were steeper as well. In case of NM, CM and TM combined with Shu-Osher, it was observed that the the latter two schemes were stable and less dissipative. Additionally, the reason for the less than $-5/3$ slope in energy spectra for CM and LM was due to insufficient rate of energy transfer at high wavenumbers.

Simulations for CM and LM with Shu-Osher were conducted on the 128^3 grid. CM became unstable at $t^* \approx 12$ due to insufficient viscosity. However, LM was successful in capturing the vortex stretching mechanism. This was confirmed by the relatively large enstrophy production and high intermittency during the transition phase.

Lessons Learned: The dissertation demonstrates the feasability of ILES approach based on Godunov-type schemes. The results from decaying isotropic turbulence and Taylor-Green vortex cases suggest that numerical viscosity inherent to shock-capturing schemes holds the potential to facilitate accurate and reliable large-eddy simulations of compressible turbulent and transitional flows. Moreover, truncation error terms when controlled by mechanisms based on the flow physics can be of significant advantage instead of treating them as an inconvenience that is to

be avoided at all costs. The study also showed that second-order schemes such as Roe-MUSCL with modifications can achieve accuracy that is comparable to computationaly expensive higher-order schemes. This will be of interest to the industry where there is widespread usage of second-order schemes such as TVD-MUSCL. Furthermore, the Roe-MUSCL formulation developed can be easily applied to flows in and around complicated geometries where unstructured meshes are the norm.

6.2 Future Work

The simulations of compressible turbulent flows are extremely challenging for current numerical algorithms due to large number of mathematical as well as physical symmetries. Therefore, the issue of stability for compressible flow solvers is a topic of great interest. Currently, the two main approaches to improve the stability of compressible schemes are: (i) writing the convective fluxes in skew-symmetric form, and (ii) satisfying in a discrete sense an additional equation for quantities such as the entropy.

The presence of shocks waves in the flow adds to the complexity. In fact, the interaction between a shock wave and turbulent flow is regarded as a fundamental problem in fluid mechanics [112,113]. Such interactions are common both in nature as well as in engineering flows. Examples include supernova explosions, supersonic flight and propulsion, and internal confinement fusions, among others. These involve additional complexities such as real gas effects, nonuniform mean flow or streamline curvature that can significantly affect the interaction process. In order to obtain a fundamental understanding of the phenomenon, canonical studies involving isotropic turbulence

passing through a normal shock is considered first. Hence, future work could entail performing rigorous DNS and ILES simulations of the shock-isotropic-turbulence interaction problem at high M_t and Re_λ. To achieve this, entropy-consistent scheme of Ismail and Roe [114] can be utilized. The scheme provides stability in 1-D for strong shocks. However, it is unclear whether a straightforward extension can guarantee similar stability in multidimensional scenarios. Therefore, it is important to test a multidimensional formulation of this flux for two important cases: (1) hypersonic flow around blunt body, and (2) hypersonic double-cone flow problem. The former is an ideal test case for investigating the appearance of the carbuncle phenomenon, whereas the latter is a relatively complex problem consisting of shock interactions, triple points and recirculation zones that are found in flow past hypersonic vehicles.

If the scheme performs poorly in combating multidimensional shock instability, it would be interesting to see whether coupling of the 1-D entropy-consistency mechanism with the multidimensional dissipation algorithm of either Nishikawa and Kitamura [115], and Roe and Kitamura [116] can satisfy entropy-consistency and therefore generate stable solutions in higher-dimensions. The next logical step is to extend the scheme to higher-order using MUSCL extrapolation technique. A stability study could be conducted again with the higher-order scheme for the above canonical problems.

The following step could involve performing DNS and ILES of decaying isotropic turbulent flow simulations to investigate the scheme's stability and diffusive characteristics. If needed, the excess dissipation can be mitigated using the z-factor modifications proposed by Thornber et al. [9], and Bidadi and Rani [64]. The numerical

viscosity and dissipation rate of the scheme can be quantified following the approach presented in this dissertation. The final phase of the study then involves performing numerical experiments for a shock wave interacting with isotropic turbulence at high M_t and Re_λ.

APPENDICES

APPENDIX A

NEGLECTING DIFFERENCE IN STATE QUANTITIES AT AN INTERFACE

In equation (2.21), the difference in state quantities at the interface $(q_R - q_L)$ was neglected in comparison to $(q_{R,c} - q_{L,c})$. To verify this assertion, three types of reconstruction are considered on a 1-D uniform grid, namely CDS, linear reconstruction with limiter ψ, and UDS, which are represented as shown in Figure A.1. From Figure A.1, it is qualitatively evident that for the case of linear reconstruction with limiter ψ, $(q_R - q_L)$ at the interface is smaller than $(q_{R,c} - q_{L,c})$. Using scaling analysis, we will show that $(q_R - q_L)$ is at least an order of magnitude smaller than $(q_{R,c} - q_{L,c})$.

For the second-order CDS on a uniform mesh, the interface state is simply an average of the left and right cell-centered states, $q_{L,c}$ and $q_{R,c}$ respectively. The reconstruction of the interface state for CDS can therefore be illustrated as shown in Figure A.1(a). It can be seen that both the left and right reconstructed states at the interface are the same, i.e., $q_R = q_L$ so that $q_R - q_L$ is exactly zero. Therefore, for CDS $(q_R - q_L) \ll (q_{R,c} - q_{L,c})$ is satisfied.

For UDS, data is treated as piecewise constant in each cell, as shown in Figure A.1(c). Consequently, for UDS: $(q_R - q_L) = (q_{R,c} - q_{L,c})$. Hence, $(q_R - q_L) \ll$

$(q_{R,c} - q_{L,c})$ is *not* satisfied for UDS. We will now demonstrate that for the case of linear reconstruction with limiter ψ, shown in Figure A.1(b), one may indeed neglect $(q_R - q_L)$ in comparison to $(q_{R,c} - q_{L,c})$. It is to be noted that the following analysis is an order of magnitude analysis and hence equalities are used interchangeably with $\sim$ or $\approx$.

Linear reconstruction of interface states, q_L and q_R, using ψ and Λ on a uniform 1-D mesh can be expressed as follows:

$$q_L = q_{L,c} + \frac{\psi}{\Lambda}\left.\frac{\partial q}{\partial x}\right|_{L,c}\frac{\Delta x}{2} + O(\Delta x^2) \tag{A.1}$$

$$q_R = q_{R,c} - \frac{\psi}{\Lambda}\left.\frac{\partial q}{\partial x}\right|_{R,c}\frac{\Delta x}{2} + O(\Delta x^2) \tag{A.2}$$

Subtracting (A.1) from (A.2) yields

$$(q_R - q_L)_\psi = (q_{R,c} - q_{L,c}) - \frac{\psi}{\Lambda}\left(\left.\frac{\partial q}{\partial x}\right|_{R,c} + \left.\frac{\partial q}{\partial x}\right|_{L,c}\right)\frac{\Delta x}{2} \tag{A.3}$$

where $(q_R - q_L)_\psi$ refers to the difference in the right and left interface states for the case of linear reconstruction with limiter ψ.

Performing Taylor series expansion about the interface of the derivatives on the RHS of (A.3) gives

$$\left.\frac{\partial q}{\partial x}\right|_{R,c} = \left.\frac{\partial q}{\partial x}\right|_{f} + \left.\frac{\partial^2 q}{\partial x^2}\right|_{f}\frac{\Delta x}{2} + O(\Delta x^2) \tag{A.4}$$

$$\left.\frac{\partial q}{\partial x}\right|_{L,c} = \left.\frac{\partial q}{\partial x}\right|_{f} - \left.\frac{\partial^2 q}{\partial x^2}\right|_{f}\frac{\Delta x}{2} + O(\Delta x^2) \tag{A.5}$$

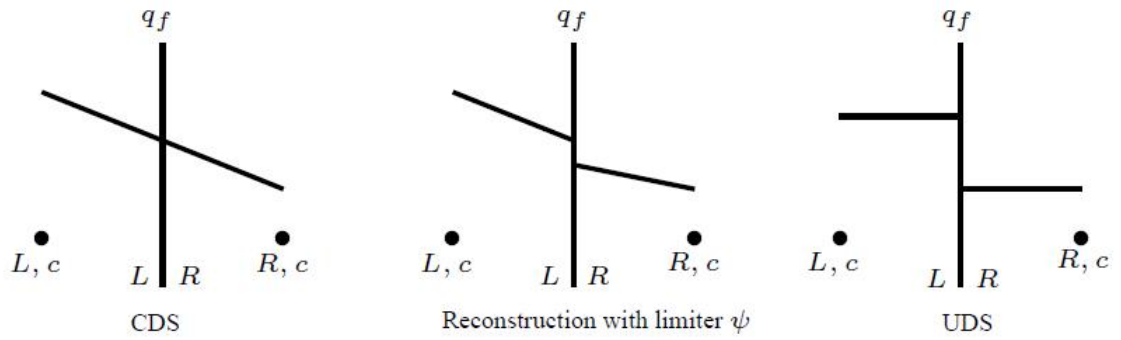

Figure A.1: Reconstruction of cell data using (a) second-order CDS, (b) linear reconstruction with limiter ψ and (c) UDS.

Substituting (A.4) and (A.5) into (A.3)

$$(q_R - q_L)_\psi = (q_{R,c} - q_{L,c}) - \frac{\psi}{\Lambda} \left.\frac{\partial q}{\partial x}\right|_f \Delta x + O(\Delta x^3) \tag{A.6}$$

Upon substituting $\psi = \Lambda$ into (A.6), $(q_R - q_L)_\psi$ becomes $(q_R - q_L)_{CDS}$, where $(q_R - q_L)_{CDS}$ is the difference in the interface states when using CDS. Therefore one can write

$$(q_R - q_L)_{CDS} = (q_{R,c} - q_{L,c}) - \left.\frac{\partial q}{\partial x}\right|_f \Delta x + O(\Delta x^3) \tag{A.7}$$

Subtracting (A.7) from (A.6) yields

$$(q_R - q_L)_\psi - (q_R - q_L)_{CDS} = \left(1 - \frac{\psi}{\Lambda}\right) \left.\frac{\partial q}{\partial x}\right|_f \Delta x + O(\Delta x^3) \tag{A.8}$$

Since $(q_R - q_L)_{CDS}$ is $O(0)$, it is clear from (A.8) that $(q_R - q_L)_\psi$ is $O\left[\left(1 - \frac{\psi}{\Lambda}\right)\Delta x\right]$. This means that when $\frac{\psi}{\Lambda} \to 1$, $(q_R - q_L)_\psi \to O(\Delta x^3)$. That is, the constraint $(q_R - q_L) \ll (q_{R,c} - q_{L,c})$ is best satisfied when $\frac{\psi}{\Lambda}$ is close to 1. Also, for $\Lambda = 2$

and $\psi > 1$, and for $\Lambda = 1$ and $\psi < 1$, $(q_R - q_L)_\psi$ is $O\left[10^{-1}\Delta x\right]$. One can therefore conclude that $(q_R - q_L)_\psi$ is at least an order of magnitude smaller than $(q_{R,c} - q_{L,c})$, justifying the neglect of the former in comparison to the latter. The same argument is applied to neglect $[(\mathbf{Q}_i)_R - (\mathbf{Q}_i)_L]$ in equation (3.65) when deriving the expression for numerical viscosity in the case of Euler equations.

APPENDIX B

A RELATION BETWEEN CFL NUMBER AND Λ PARAMETER

A scaling parameter Λ was introduced in Chapter 2 to preserve monotonicity of TVD schemes for multi-dimensional problems. This was possible by setting $\Lambda = 2$. In such a scenario, $\psi = 2$ corresponds to second-order central differencing scheme (CDS), which is the upper bound of the TVD-Monotonicity region (indicated by the shaded region in Figure 2.2). Although the parameter is successful in satisfying the TVD criterion for all three 2-D test cases, the resulting profiles displayed noticable smearing on structured grids. To improve this situation, the scaling parameter like the flux limiter ψ must therefore depend on local flow conditions so that it supplies just enough viscosity for preserving both the monotonicity as well as accuracy of high-resolution schemes. This can be achieved by relating the Roe-MUSCL flux to the modified Lax-Wendroff flux. The second-order Roe-MUSCL flux with limiter ψ and Λ is as follows

$$F_{RM} = \frac{1}{2}\,(\mathbf{u}\cdot\mathbf{n})_f\,(q_{L,c}+q_{R,c}) - \frac{1}{2}\,|(\mathbf{u}\cdot\mathbf{n})_f|\,(q_{R,c}-q_{L,c}) + \frac{\psi}{2\Lambda}\,|(\mathbf{u}\cdot\mathbf{n})_f|\,(q_{R,c}-q_{L,c}) \quad \text{(B.1)}$$

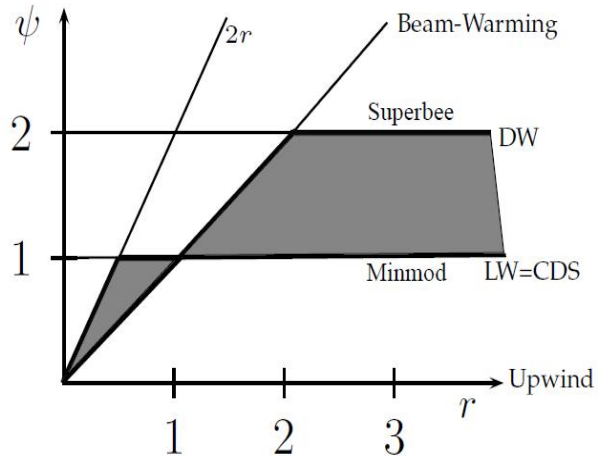

(a) CFL=0

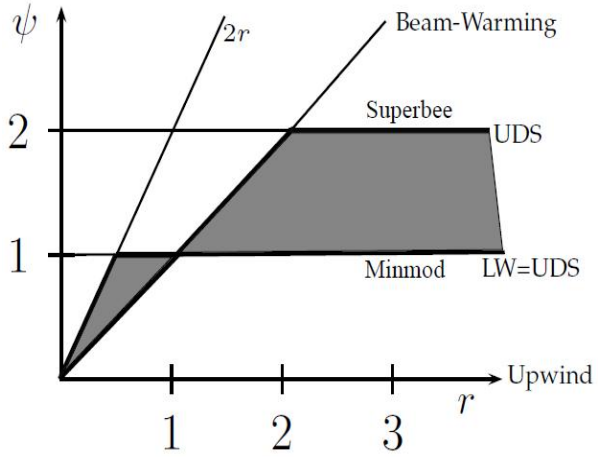

(b) CFL=1

Figure B.1: Sweby diagram for (a) CFL=0, and (b) CFL=1

Assuming $(\mathbf{u}\cdot\mathbf{n})_f > 0$, the above TVD-MUSCL flux is then

$$F_{RM} = \frac{1}{2}\,(\mathbf{u}\cdot\mathbf{n})_f\,(q_{L,c}+q_{R,c}) - \frac{1}{2}(\mathbf{u}\cdot\mathbf{n})_f\,(q_{R,c}-q_{L,c}) + \frac{\psi}{2\Lambda}\,(\mathbf{u}\cdot\mathbf{n})_f\,(q_{R,c}-q_{L,c}) \quad \text{(B.2)}$$

The Lax-Wendroff flux **modified** with limiter ψ can be written as [60]

$$F_{LW\psi} = \frac{1}{2}\,(\mathbf{u}\cdot\mathbf{n})_f\,(q_{L,c}+q_{R,c}) - \frac{1}{2}(\mathbf{u}\cdot\mathbf{n})_f\,(q_{R,c}-q_{L,c}) + \frac{\psi}{2}\,(\mathbf{u}\cdot\mathbf{n})_f(1-|\mathrm{CFL}|)\,(\mathrm{q_{R,c}}-\mathrm{q_{L,c}}) \tag{B.3}$$

Setting $F_{RM} = F_{LW\psi}$, we obtain a simple relation between Λ and Courant number CFL

$$\Lambda = \frac{1}{1-|\mathrm{CFL}|} \tag{B.4}$$

Substituting the above expression into (B.2) and setting the CFL number to 0 recovers CDS at $\psi = 1$ and downwind scheme at $\psi = 2$. As discussed previously (see Chapter 2), the net anti-diffusion supplied by the superbee scheme for this case violates the TVD-monotonicity criterion near high-gradient regions. The corresponding Sweby diagram is shown in Figure B.1(a). Setting CFL=1 recovers the highly diffusive upwind scheme for all ψ as illusrated in Figure B.1(b). Clearly, the two scenarios are not desirable. The choice of CFL=0.5 ($\Lambda = 2$) reduces Roe-MUSCL to the original Lax-Wendroff scheme when $\psi = 1$. However, since the 2-D profiles for TVD limiters with $\Lambda = 2$ exhibited noticable smearing, the Courant number must less than but lie in the vicinity of 0.5 to achieve greater accuracy.

REFERENCES

[1] W.J.A. Dahm and P.E. Dimotakis. Mixing at large scale Schmidt number in the self similar far field of turbulent jets. *Journal of Fluid Mechanics*, 217:299–330, 1990.

[2] E. Garnier. *Large eddy simulation for compressible flows*. New York, 2009.

[3] M.A. Alves, P. Cruz, A. Mendes, F.D. Magalhaes, and P.J. Oliveria. Adaptive multiresolution approach for solution of hyperbolic PDEs. *Computer Methods in Applied Mechanics and Engineering*, 191:3909 – 3928, 2002.

[4] M.S. Darwish and F. Moukalled. TVD schemes for unstructured grids. *International Journal of Heat and Mass Transfer*, 46:599–611, 2003.

[5] L. Li, H. Liao, and L. Qi. An improved r-factor algorithm for TVD schemes. *International Journal of Heat and Mass Transfer*, 51:610–617, 2008.

[6] C.B. Laney. *Computational Gas Dynamics*. Cambridge University Press, Cambridge, 1998.

[7] E.F. Toro. *Riemann Solvers and Numerical Methods for Fluid Dynamics*. Springer, New York, 2009.

[8] C.P. Dullemond. *Lecture on Numerical Fluid Dynamics*. 2009.

[9] B. Thornber, A. Mosedale, D. Drikakis, D. Younds, and R.J.R. Williams. An improved reconstruction method for compressible flows with low Mach number features. *Journal of Computational Physics*, 227:4873 – 4894, 2008.

[10] A.E. Honein and P. Moin. Higher entropy conservation and numerical stability of compressible turbulence simulations. *Journal of Computational Physics*, 201:531 – 545, 2004.

[11] H. Kang, S. Chester, and C. Meneveau. Decaying turbulence in an active-grid-generated flow and comparisons with large-eddy simulation. *Journal of Fluid Mechanics*, 480:129 – 160, 2003.

[12] A. Vincent and M. Meneguzzi. The spatial structure and statistical properties of homogeneous turbulence.

[13] M.E. Brachet, D.I. Meiron, S.A. Orszag, B.G. Nickel, and R.H. Morg. Small-scale structure of the Taylor-Green vortex. *Journal of Fluid Mechanics*, 130:411 – 452, 1983.

[14] M.E. Brachet. Direct numerical simulation of three-dimensional turbulence in the Taylor-Green vortex. *Fluid Dynamic Research*, 8:1 – 8, 1991.

[15] A. Jameson, W. Schmidt, and E. Turkel. Numerical solution of the Euler equations by finite volume methods using Runge-Kutta time stepping schemes. *AIAA*, 81-1259:1 – 17, 1981.

[16] C.-W. Shu, W-S. Don, D. Gottlieb, O. Schilling, and L. Jameson. Numerical convergence of nearly incompressible, inviscid Taylor-Green vortex flow.

[17] R. Spiteri and S. Ruuth. A class of optimal high-order strong-stability preserving time discretization methods. *Journal of Scientific Computing*, 40 (2):469 – 491, 2002.

[18] L.F. Richardson. *Weather Prediction by Numerical Process*. Cambridge University Press, 1922.

[19] G.T. Chapman and M. Tobak. *Theoretical Approaches to Turbulence*. Springer-Verlag, New York, 1985.

[20] P. Orlandi. *Fluid flow phenomena*. Kluwer Academic Publishers, 2000.

[21] W.J. Feiereisen. *Numerical simulation of a compressible, homogeneous, turbulent shear flow*. PhD Thesis, Stanford University, Palo Alto, CA, 1981.

[22] A. Kolmogorov. The local structure of turbulence in an incompressible fluid at very high Reynolds numbers. *Dokl. Akad. Nauk. SSSR*, 30, 1941.

[23] G. Comte-Bellot and S. Corrsin. Simple Eulerian time correlation of full and narrow-band velocity signals in grid-generated 'isotropic' turbulence. *Journal of Fluid Mechanics*, 48:237 – 337, 1971.

[24] T.L. Clark. A small-scale dynamic model using a terrain following coordinate system. *Journal of Computational Physics*, 24:186 – 215, 1997.

[25] S.B. Pope. *Turbulent Flows*. Cambridge University Press, 2000.

[26] D. Drikakis, M. Hahn, A. Mosedale, and B. Thornber. Large eddy simulation using high-resolution and high-order methods. *Philosophical Transactions of the Royal Society*, 367:2895 – 2997, 2009.

[27] C.W. Hirt. Computer studies of time-dependent turbulent flows. *Physics of Fluids*, 2:219 – 227, 1969.

[28] J. Smagorinsky. General circulation experiments with the primitive equations. *Monthly Weather Review*, 91:99 – 164, 1963.

[29] M. Germano. A dynamic subgrid-scale eddy viscosity model. *Physics of Fluids A*, 3:1760 – 1765, 1991.

[30] E. Garnier, M. Mossi, P. Sagaut, P. Comte, and M. Deville. On the use of shock-capturing schemes for large-eddy simulation. *Journal of Computational Physics*, 153:273 – 311, 1999.

[31] M. Hahn El-Asrag. *Implicit large-eddy simulation of low-speed separated flows using high-resolution methods*. Ph.D. Thesis, Cranfield University, 2008.

[32] C. Fureby and F.F. Grinstein. Large-eddy simulation of High-Reynolds-Number free and wall-bounded flows. *Journal of Computational Physics*, 181:68 – 97, 2002.

[33] F.F. Grinstein, L.G. Margolin, and W.J. Rider. Cambridge University Press.

[34] S.K. Godunov. A finite-difference method for the numerical computation and discontinious solutions of the equations of fluid dynamics. *Math. Sbornik*, 47:271–306, 1959.

[35] J.P. Boris, F.F. Grinstein, E.S. Oran, and R.L. Kolbe. New insights into large eddy simulation. *Fluid Dynam. Res.*, 10, 1992.

[36] H. Bethe. On the theory of shock waves for an arbitrary equation of state. Technical report, Office of Scientific Research and Development, 1942.

[37] J.P. Boris. *On large eddy simulation using subgrid turbulence models, in Whither Turbulence? Turbulence at Crossroads*. Springer-Verlag, New York, 1990.

[38] W.J. Rider and L.G. Margolin. From numerical analysis to implicit subgrid turbulence modeling. 16^{th} *AIAA CFD Conference*, AIAA 2003-4101, 2003.

[39] B. Thornber, D. Drikakis, R.J.R. Williams, and D. Youngs. On entropy generation and dissipation of kinetic energy in high-resolution shock-capturing schemes. *Journal of Computational Physics*, 227:4853 – 4872, 2008.

[40] P.L. Roe. Approximate Riemann Solvers, Parameter Vectors, and Difference Schemes. *Journal of Computational Physics*, 43:357–372, 1981.

[41] E.A. Luke and T. George. A rule-based framework for parallel multidisciplinary simulation synthesis. *Journal of Functional Programming*, 3:477 – 502, 2005.

[42] E.A. Luke and P. Cinnella. Numerical simulation of mixtures of fluids using upwind algorithms. *Computers and Fluids*, 36:1547 – 1566, 2007.

[43] S. Thakur, J. Wright, and W. Shyy. An algorithm for chemically reactive flows on generalized grids using a rule-based framework. *43rd AIAA Conference, Paper No. 2005-0875*, 2005.

[44] J.P. Boris and D.L. Book. Flux-Corrected Transport I: SHASTA, a fluid-transport algorithm that works. *Journal of Computational Physics*, 11:38 – 69, 1973.

[45] B. van Leer. Towards the ultimate conservative difference scheme, V. A second-order sequel to Godunov's Method. *Journal of Computational Physics*, 32:357–393, 1979.

[46] P. Collella P and P.R. Woodward. The Piecewise Parabolic Method (PPM) for gas-dynamical simulations. *Journal of Computational Physics*, 54:174 – 201, 1984.

[47] V.P. Kolgan. Application of the principle of minimizing the derivative to the construction of finite-difference schemes for computing discontinious solutions of gas dynamics. Technical report.

[48] V.P. Kolgan. Application of the principle of minimizing the derivative to the construction of finite-difference schemes for computing discontinious solutions of gas dynamics. *Journal of Computational Physics*, 230:2384 – 2390, 2011.

[49] B. van Leer. A historical oversight: Vladimir P. Kolgan and his high-resolution scheme. *Journal of Computational Physics*, 230:2378 – 2383, 2011.

[50] C. Bruner. *Parallelization of the Euler equations on unstructured grids.* PhD Thesis, Virginia Polytechnic Institute and State University, Blacksburg, VA, 1996.

[51] C. Bruner. Parallelization of the euler equations on unstructured grids. *AIAA*, 97, 1995.

[52] B.P. Leonard. A stable and accurate convective modeling procedure based on quadratic upstream interpolation. *Computer Methods in Applied Mechanics and Engineering*, 19:59–98, 1979.

[53] A.M. Mohammadian and D.Y. Le Roux. Fourier analysis of a class of upwind schemes in shallow water systems for gravity and Rossby waves. *International Journal for Numerical Methods in Fluid*, 57:389–416, 2008.

[54] P. Tamamidis. A new upwind scheme on triangular meshes using the finite volume method. *Computer Methods in Applied Mechanics and Engineering*, 124:15–31, 1995.

[55] P. Juntasaro and A.J. Marquis. Comparative Study of Flux-limiters Based on MUST Differencing Scheme. *International Journal of Computational Fluid Dynamics*, 18:569–576, 2004.

[56] W.K. Anderson and D.L. Bonhaus. An Implicit Upwind Algorithm for Computing Turbulent Flows on Unstructured Grids. *Computers and Fluids*, 1:1 – 21, 1994.

[57] P.K. Sweby. High resolution schemes using flux limiters for hyperbolic conservation laws. *SIAM Journal of Numerical Analysis*, 21:995 – 1011, 1984.

[58] M. Berger, M.J. Aftosmis, and S.M. Murman. Analysis of slope limiters on irregular grids. NAS Technical Report NAS-05-007, NASA, 2005.

[59] B. Thornber, A. Mosedale, and D. Drikakis. On the implicit large eddy simulations of homogeneous decaying turbulence. *Journal of Computational Physics*, 226:1902 – 1929, 2007.

[60] R.J. Leveque. *Finite volume Methods for Hyperbolic problems.* Cambridge University Press, New York, 2009.

[61] M. Torrilhon. Krylov-Riemann solver for large hyperbolic systems of conservation laws. *SIAM Journal of Scientific Computing*, 34:2072 – 2091, 2012.

[62] P. Lax and B. Wendroff. System of Conservation Laws. *Communications on Pure and Applied Mathematics*, 13:217 – 237, 1960.

[63] J. Johnson and R. Cheret. *Classic papers in Shock Compression Science.* Springer-Verlag, 1998.

[64] S. Bidadi and S.L. Rani. Investigation of numerical viscosities and dissipation rates of second-order TVD-MUSCL schemes for implicit large-eddy simulation. *Journal of Computational Physics*, 281:1003 – 1031, 2015.

[65] W.K. Anderson, J.L. Thomas, and B. van Leer. Comparison of finite volume flux vector splittings for the Euler equatins. *AIAA Journal*, 24:1453 – 1460, 1985.

[66] B. van Leer. Upwind-difference methods for aerodynamic problems governed by the Euler equations. *Large-Scale Computations in FLuid Mechanics*, 22:327 – 336, 1985.

[67] M.-S. Liou and C. Steffen. A new flux splitting scheme. *Journal of Computational Physics*, 107:23 – 39, 1993.

[68] J.L. Steger and R.F. Warming. Flux vector splitting of the inviscid gasdynamic equations with applications to finite-difference methods. *Journal of Computational Physics*, 40:263 – 293, 1981.

[69] B. van Leer. *Flux-vector splitting for the Euler equations.* Springer-Verlag, Berlin, 1982.

[70] M. Brio and C.C. Wu. An upwind differencing scheme for the Euler equations of ideal magnetohydrodynamics. *Journal of Computational Physics*, 75:400 – 422, 1988.

[71] E.F. Toro. Riemann-problem based techniques for computing reactive two phase flows. 351:472 – 481, Proceedings of the Third International Conference on Numerical Combustion.

[72] J.F. Clarke, S. Karni, J.J. Quirk, L.G. Simmons, P.L. Roe, and E.F. Toro. Numerical computation of two-dimensional, unsteady detonation waves in high energy solids. *Journal of Computational Physics*, 106:215 – 233, 1993.

[73] F. Rieper. On the dissipation mechanism of upwind-schemes in the low Mach number regime: A comparison between Roe and HLL. *Journal of Computational Physics*, 229:221 – 232, 2010.

[74] G. Strang. Construction and comparison of difference schemes. *Journal of Numerical Analysis*, 5(3):506 – 517, 1968.

[75] N.N. Yaneko. *The method of fractional steps*. Springer-Verlag, New York, 1971.

[76] B. van Leer. Upwind and high-resolution methods for compressible flow: from donor cell to residual-distribution schemes. *Communications in Computational Physics*, 1(2):192 – 206, 2006.

[77] S.F. Davis. A rotationally-biased upwind difference scheme for the Euler equations. *Journal of Computational Physics*, 106, 1984.

[78] N.T. Frink. Upwind scheme for solving the Euler equations on unstructured tetrahedral meshes. *AIAA Journal*, 30 (1):70 – 77, 1992.

[79] N.T. Frink. *Three-dimensional upwind scheme for solving the Euler equations on unstructured tetrahedral grids*. Ph.D. Thesis, Virginia Polytechnic Institute and State University, Blacksburg, VA, September 1991.

[80] S. Bidadi and S.L. Rani. Quantification of numerical diffusivity due to TVD schemes in the advection equation. *Journal of Computational Physics*, 261:65 – 82, 2014.

[81] A. Harten, P.D. Lax, and B. van Leer. On upstream differencing and Godunov type schemes for hyperbolic conservation laws. *SIAM Review*, 25:35 – 61, 1983.

[82] P.K. Subbareddy and G.V. Candler. A fully discrete, kinetic energy consistent finite-volume scheme for compressible flows. *Journal of Computational Physics*, 228:1347 – 1364, 2009.

[83] G.A. Sod. A survey of several finite difference methods for systems of nonlinear hyperbolic conservation laws. *Journal of Computational Physics*, 27:1 – 31, 1978.

[84] G. Fernandez N. Balakrishnan. Wall boundary conditions for inviscid compressible flows on unstructured meshes. *International Journal for Numerical Methods in Fluids*, 28:1481 – 1501, 1998.

[85] L.S.G. Kovasznay. Turbulence in supersonic flow. *Journal of Aerospace Sciences*, 20:657 – 682, 1953.

[86] B.T. Chu and L.S.G. Kovasznay. Non-linear interactions in a viscous heat-conducting compressible gas. *Journal of Fluid Mechanics*, 3:494 – 514, 1957.

[87] J. Wang, Y. Shu, L. Wang, Z Xiao, and X. He. Effects of shocklets on the velocity gradients in highly compressible isotropic turbulence. *Physics of Fluids*, 23, 2011.

[88] J.E. Moyal. The spectra of turbulence in a compressible fluid; eddy turbulence and random noise. *Proc. Camb. Phil. Soc.*, 48:329 – 344, 1951.

[89] G.A. Blaidell, N.N Mansour, and W.C. Reynolds. Compressibility effects on the growth and structure of homogeneous turbulent shear flow. *Journal of Fluid Mechanics*, 256:443 – 485, 1993.

[90] W.J. Feiereisen, W.C. Reynolds, and J.H. Ferziger. Numerical simulation of a compressible homogeneous turbulent shear flow. Report no. tf-13, Stanford University, 1981.

[91] R. Samtaney, D.I. Pullin, and K. Branko. Direct numerical simulation of decaying compressible turbulence and shocklet statistics. *Physics of Fluids*, 13:1415 – 1430, 2001.

[92] S. Lee, Lele, S.K., and P. Moin. Eddy shocklets in decaying compressible turbulence. *Physics of Fluids A*, 3:657 – 664, 1991.

[93] D.H. Porter, A. Pouquet, and P.R. Woodward. Kolmogorov-like spectra in decaying three-dimensional supersonic flows. *Physics of Fluids*, 6:2133 – 2142, 1994.

[94] B. Kosovic, D.I. Pullin, and R. Samtaney. Subgrid-scale modeling for large-eddy simulations of compressible turbulence. *Physics of Fluids*, 14:1511 – 1522, 2002.

[95] A. Kolmogorov. A refinement of previous hypothesis concerning the local structure of turbulence in a viscous incompressible fluid at high Reynolds number. *Journal of Fluid Mechanics*, 13:82 – 85, 1962.

[96] R. Rogallo. Numerical experiments in homogeneous turbulence. Technical report tm-81315, NASA, 1990.

[97] J. Domaradzski, Z. Xiao, and P. Smolarkiewicz. Effective eddy viscosities in implicit large eddy simulation of turbulent flows. *Physics of Fluids*, 15:3890 – 3893, 2003.

[98] M. Ciardi, P. Sagaut, M. Klien, and W. Dawes. A dynamic finite volume scheme for large-eddy simulation on unstructured grids. *Journal of Computational Physics*, 210:632 – 655, 2005.

[99] G. Erlebacher, M.Y. Hussaini, C.G. Speziale, and T.A. Zang. Toward the large-eddy simulation of compressible turbulent flows. *Journal of Fluid Mechanics*, 238:155 – 185, 1992.

[100] D. Drikakis, C. Fureby, F.F. Grinstein, and D. Youngs. Simulation of transition and turbulence decay in the Taylor-Green vortex. *Journal of Turbulence*, 8:1 – 12, 2007.

[101] P.G. Saffman. Note on decay of homogeneous turbulence. *Physics of Fluids*, 10, 1967.

[102] S. Hickel, N.A. Adams, and J. Domaradzki. An adaptive local deconvolution method for implicit LES. *Journal of Computational Physics*, 213:413 – 436, 2006.

[103] O. Metais and M. Lesieur. Spectral large-eddy simulations of isotropic and stably-stratified turbulence. *Journal of Fluid Mechanics*, 239:157 – 194, 1992.

[104] C.W. Shu and S. Osher. Efficient implementation of essentially non-oscillatory shock-capturing schemes. *Journal of Computational Physics*, 77:439 – 471, 1988.

[105] S. Osher and R.P. Fedkiw. *Level set methods and dynamic implicit surfaces*. Springer-Verlag, New York, 2002.

[106] Y. Zhou, F.F. Grinstein, A.J. Wachtor, and B.M. Haines. Estimating the effective Reynolds number in implicit large-eddy simulation. *Physical Review E*, 89:1 – 13, 2014.

[107] C. Fureby and F.F. Grinstein. Monotonically integrated large eddy simulation of free shear flows. *AIAA Journal*, 37 (5):544 – 556, 1999.

[108] Y. Zhou, F.F. Grinstein, A.J. Wachtor, and B.M. Haines. Analysis of Implicit LES methods. *Communications in Applied Mathematics and Computational Science*, 3 (1):103 – 126, 2008.

[109] M. Latini, O. Schilling, and W.S. Don. Effects of WENO flux reconstruction order and spatial resolution on reshocked two-dimensional Richtmyer-Meshkov instability. *Journal of Computational Physics*, 221:805–836, 2007.

[110] O. Schilling and Y. Zhou. Analysis of spectral eddy viscosity and backscatter in incompressible, isotropic turbulence using statistical closure theory. *Physics of Fluids*, 14 (3):1244–1258, 2002.

[111] M. Lesieur and S. Ossia. 3-D isotropic at very high Reynolds numbers: EDQNM study. *Journal of Turbulence*, 1:1 – 25, 2000.

[112] J. Larsson and S.K. Lele. Direct numerical simulation of canonical shock/turbulence interaction. *Physics of Fluids*, 21:1 – 12, 2009.

[113] J. Larsson, I. Bermejo-Moreno, and S.K. Lele. Reynolds- and Mach-number effects in canonical shock-turbulence interaction. *Journal of Fluid Mechanics*, 717:293–321, 2013.

[114] F. Ismail and P.L. Roe. Affordable, entropy-consistent Euler flux functions 2: Entropy production at shocks. *Journal of Computational Physics*, 228:5410–5436, 2009.

[115] H. Nishikawa and K. Kitamura. Very simple, carbuncle-free, boundary-layer-resolving, rotated-hybrid Riemann solvers. *Journal of Computational Physics*, 227:2560–2581, 2008.

[116] P.L. Roe and K. Kitamura. Artificial surface tension to stabilize captured shockwaves. *AIAA conference no. 2008-3991*, 2008.